| | |
|---|---|
| Title | Development of Thermally Activated Delayed Fluorescent Donor-Acceptor-Donor-Acceptor π-Conjugated Macrocycles |
| Author(s) | 和泉, 彩香 |
| Citation | 大阪大学, 2021, 博士論文 |
| Version Type | VoR |
| URL | https://doi.org/10.18910/82209 |
| rights | |
| Note | |

Doctoral Dissertation

# Development of Thermally Activated Delayed Fluorescent Donor–Acceptor–Donor–Acceptor π-Conjugated Macrocycles

**Saika Izumi**

January 2021

*Department of Applied Chemistry*

*Graduate School of Engineering*

*Osaka University*

# Development of Thermally Activated Delayed Fluorescent Donor–Acceptor–Donor–Acceptor π-Conjugated Macrocycles

（熱活性化遅延蛍光を示すドナー・アクセプター・ドナー・アクセプター型
π共役マクロサイクルの創製）

**2021**

**Saika Izumi**

*Department of Applied Chemistry*
*Graduate School of Engineering*
*Osaka University*

# Preface

The studies presented in this Thesis were conducted under the supervision of Professor Dr. Satoshi Minakata, Department of Applied Chemistry, Graduate School of Engineering, Osaka University during the period of 2015–2021.

The objects of this Thesis cover the development of thermally activated delayed fluorescent donor–acceptor–donor–acceptor π-conjugated macrocycles. The author hopes sincerely that the fundamental work described in this thesis contributes to further development of donor–acceptor π-conjugated macrocycles, thermally activated delayed fluorescent molecules, and other related fields of chemistry.

S. Izumi

Saika Izumi

Department of Applied Chemistry
Graduate School of Engineering
Osaka University
Suita, Osaka
JAPAN

January, 2021

# Contents

# Abbreviations

| | |
|---|---|
| A | electron acceptor |
| Abs, abs | absorption |
| ADF | amsterdam density functional |
| anal | analytical |
| ATR | attenuated total reflection |
| BOC | *tert*-butoxycarbonyl |
| br | broad |
| brs | broad singlet |
| Bu | butyl |
| *c* | concentration |
| calc | calculation |
| calcd | calculated |
| CBP | 4,4'-bis(*N*-carbazolyl)-1,1'-biphenyl |
| conc | concentrated |
| COP | cycloolefin polymer |
| COSMO | conductor-like screening model |
| COSY | correlation spectroscopy |
| C-PCM | continuum solvation model |
| CPP | cycloparaphenylene |
| CT | charge-transfer |
| $^1$CT | singlet charge-transfer state |
| $^3$CT | triplet charge-transfer state |
| CV | cyclic voltammetry |
| D | electron donor |
| d | doublet |
| DBPHZ | dibenzo[*a*,*j*]phenazine |
| DCM | dichloromethane |
| dec. | decomposition |
| DF | delayed fluorescence |
| DFT | density functional theory |
| DIH | 1,3-diiodo-5,5-dimethylhydantoin |
| DMAP | 4-dimethylaminopyridine |
| DMF | *N*,*N*-dimethylformamide |
| DPEPhos | bis[2-(diphenylphosphino)phenyl]ether |
| EA | electron affinity |
| $\Delta E_{\mathrm{Ea}}$ | activation energy of delayed fluorescence |
| EI | electron ionization |
| em | emission |
| EPR | electron paramagnetic resonance |
| EQE | external quantum efficiency |
| equiv | equivalent |
| $E_{\mathrm{S1}}$ | singlet energy |
| $\Delta E_{\mathrm{ST}}$ | energy splitting between singlet state and triplet state |
| EtOAc | ethyl acetate |
| $E_{\mathrm{T1}}$ | triplet energy |
| ex | excitation |
| FAB | fast atom bombardment |
| Fc | ferrocene |
| FL | fluorescence |
| HAT-CN | 2,3,6,7,10,11-hexacyano-1,4,5,8,9,12-hexaazatriphenylene |
| HMBC | heteronuclear multiple bond coherence |
| HOMO | highest occupied molecular orbital |
| HRMS | high resolution mass spectrometry |
| HSQC | heteronuclear single quantum correlation |
| ICT | intramolecular charge-transfer |
| IP | ionization potential |
| IQE | internal quantum efficiency |
| IR | infrared resonance |
| ISC | intersystem crossing |

| | |
|---|---|
| ITO | indium-tin-oxide |
| IV-CT | intervalence charge-transfer |
| LE | locally excited |
| $^{3}\mathrm{LE}_{\mathrm{A}}$ | locally excited triplet state of acceptor |
| LUMO | lowest occupied molecular orbital |
| m | multiplet |
| *m* | meta |
| max | maximum |
| MC | macrocycle |
| mp | melting point |
| MS | mass spectrometry |
| NBA | *m*-nitrobenzyl alcohol |
| *n*-Bu$_4$NBF$_4$ | tetrabutylammonium tetrafluoroborate |
| NIR | near infrared |
| NLO | nonlinear optic |
| NMR | nuclear magnetic resonance |
| NOESY | nuclear overhauser enhancement spectroscopy |
| NPB | *N*,*N*'-di(1-naphthyl) -*N*,*N*'-diphenyl-(1,1'-biphenyl)-4,4'-diamine |
| NTO | natural transition orbital |
| OFET | organic field-effect transistor |
| OLED | organic light emitting diode |
| OTf | trifluoromethanesulfonyl |
| ox | oxidation |
| *p* | para |
| PCM | polarizable continuum model |
| Pd/C | palladium on carbon |
| PF | prompt fluorescence |
| PH | phosphorescence |
| Ph | phenyl |
| PL | photoluminescence |
| PLQY | photoluminescence quantum yield |
| PVC | photovoltaic cell |
| QPhos | 1,2,3,4,5-pentaphenyl-1'-(di-*tert*-butylphosphino)ferrocene |
| red | reduction |
| $R_{\mathrm{f}}$ | retention factor |
| rISC | reverse intersystem crossing |
| rt | room temperature |
| SOC | spin-orbit coupling |
| SPhos | 2-dicyclohexylphosphino-2',6'-dimethoxybiphenyl |
| $\mathrm{S}_1$ | lowest excited singlet state |
| t | triplet |
| *t*, *tert* | tertiary |
| TAPC | 1,1-bis[(di-4-tolylamino) phenyl]cyclohexane |
| TADF | thermally activated delayed fluorescence |
| *t*-BuXPhos | 2-di-*tert*-butylphosphino-2',4',6'-triisopropylbiphenyl |
| TD | time decay |
| $T_{\mathrm{d}}$ | decomposition temperature |
| TD-DFT | time-dependent density functional theory |
| TFA | trifluoroacetic acid |
| TGA | thermogravimetric analysis |
| THF | tetrahydrofuran |
| TLC | thin layer chromatography |
| TOCSY | total correlation spectroscopy |
| TPBi | 2,2',2"-(1,3,5-benzinetriyl)-tris(1-phenyl-1*H*-benzimidazole) |
| TPDA | *N*,*N*,*N*',*N*'-tetraphenylbenzene-1,4-diamine |
| $\mathrm{T}_1$ | lowest excited triplet state |
| UFF | universal force field |
| UV | ultraviolet |
| vis | visible |
| XantPhos | 4,5-bis(diphenylphosphino)-9,9-dimethylxanthene |

# General Introduction

## 1. Donor–Acceptor (D–A) π-Conjugated Molecules

Donor–acceptor (D–A) π-conjugated molecules, which comprise of an electron-rich donor (D) moiety and an electron-deficient acceptor (A) moiety connected through a π-conjugated bridge or a single bond, exhibit unique optical properties that stem from intramolecular charge-transfer (ICT) (Figure 1).[1] Therefore, a large number of photofunctional D–A π-conjugated molecules have been extensively developed and applied in the field of artificial photosynthesis,[2] bioimaging,[3] and optoelectronics such as photovoltaic cells (PVCs)[4] and nonlinear optics (NLOs).[5]

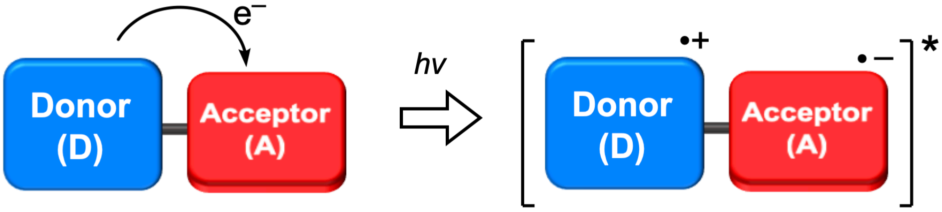

**Figure 1.** Intramolecular charge transfer of D–A π-conjugated molecules. Through this Thesis, the donor moiety and the acceptor moiety are shown in blue and red, respectively.

## 2. D–A π-Conjugated Macrocycles

Organic π-conjugated macrocycles,[6] which are regarded as terminal-less counterparts of linear π-conjugated oligomers and polymers, play crucial roles in materials science, and they have emerged as unique organic functional materials.[7,8] Among π-conjugated macrocycles, macrocycles composed of π-electronic donors and acceptors (i.e., D–A π-conjugated macrocycles) have attracted much attention, as they are expected to show not only opto- and electronic-properties resulting from ICT nature (Figure 2) but also unique properties arising from peculiar topology such as twisted, curved and/or bent terminal-less π-systems (Figure 3).[8] In addition, they can form highly ordered two-dimensional and three-dimensional molecular assemblies, which are difficult to realize with flat π-conjugated systems.[8] Although a significant number of hydrocarbon-based π-conjugated macrocycles have been developed,[7] D–A π-conjugated macrocycles have been much less explored,[9] probably because the processes of cyclization of π-conjugated linear framework are enthalpically and entropically unfavorable, and electron-donating and -accepting building blocks suitable for cyclization are limited.

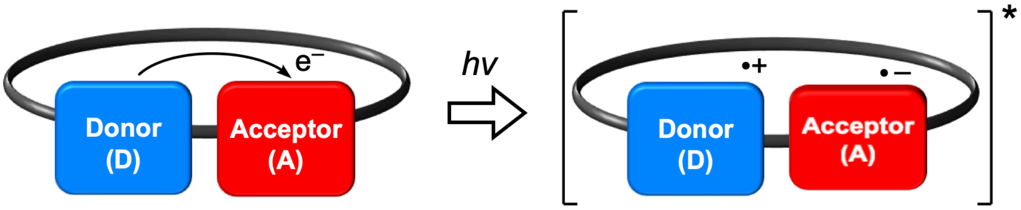

**Figure 2.** Intramolecular charge transfer of D–A π-conjugated macrocycles.

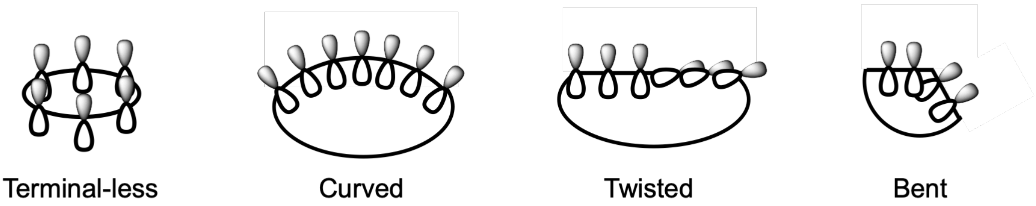

**Figure 3**. Peculiar topology of organic π-conjugated macrocycles.

As examples of D–A π-conjugated macrocycles, in 2012, Jäkle reported ambipolar B–π–N macrocycles, which show unique Lewis-base-responsive photoluminescent behaviors (Figure 4a).[10] In 2015, electron-deficient arene-incorportated cycloparaphenylenes (CPPs), which are featured with narrower HOMO/LUMO band gaps than those with the same ring-size all-carbon CPPs, were independently developed by Jasti[11a] and Itami[11b] (Figure 4b).

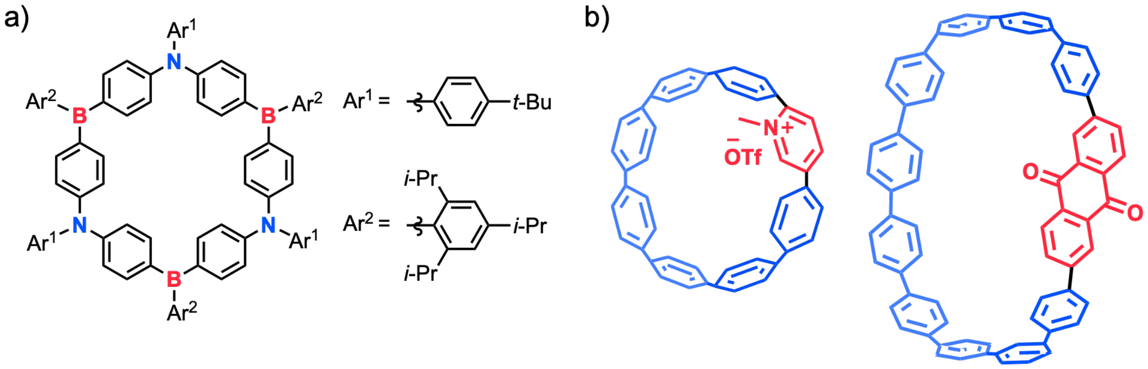

**Figure 4.** Examples of D–A π-conjugated macrocycles.

D–A-repeating carbon nanohoops comprised of multiple D−A units (D = bithiophene derivatives; A = perylene diimides derivatives) have been intensively developed by the Nuckolls group (Figure 5).[9b] They demonstrated that the D–A macrocycles can act as n-type materials in organic field-effect transistors (OFETs)[12] and bulk heterojunction OPVs,[12a] and as an active material of organic capsule transistors for sensing chemicals.[12c]

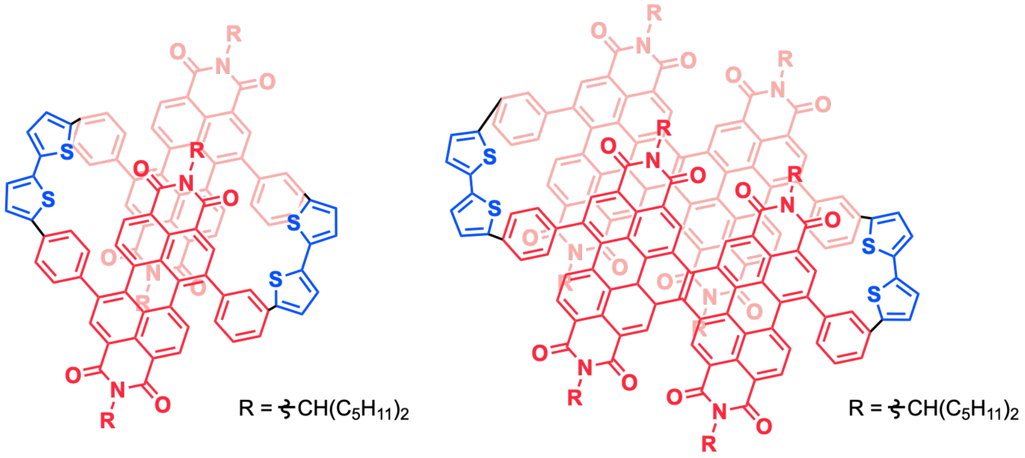

**Figure 5.** Examples of D–A π-conjugated macrocycle as functional materials.

Therefore, the development of novel D–A π-conjugated macrocycles and the investigation of their properties would allow for tailoring their optoelectronic properties by fluctuating three-dimensional shapes (e.g., bent, curved, and twisted conformations) and exterior/interior π–π interactions and/or host–guest interactions peculiar to D–A π-conjugated macrocycles.

## 3. Thermally Activated Delayed Fluorescent Molecules

Thermally activated delay fluorescence (TADF) is a fundamental phenomenon, which is a fluorescence irradiated from the lowest singlet excited state ($S_1$) through reverse intersystem crossing (rISC) from the triplet excited state ($T_1$) with the aid of thermal activation (Figure 6). Due to the involvement of the triple excited state, TADF compounds have significant potentials as functional materials in the fields of photocatalysis,[13] bioimaging,[14] and especially of optoelectronics. TADF materials are promising for enhancing external quantum efficiency (EQE) of organic light-emitting diodes (OLEDs), because TADF-active organic emitters can theoretically harvest 100% excitons that are electrically generated in the emitting layer.

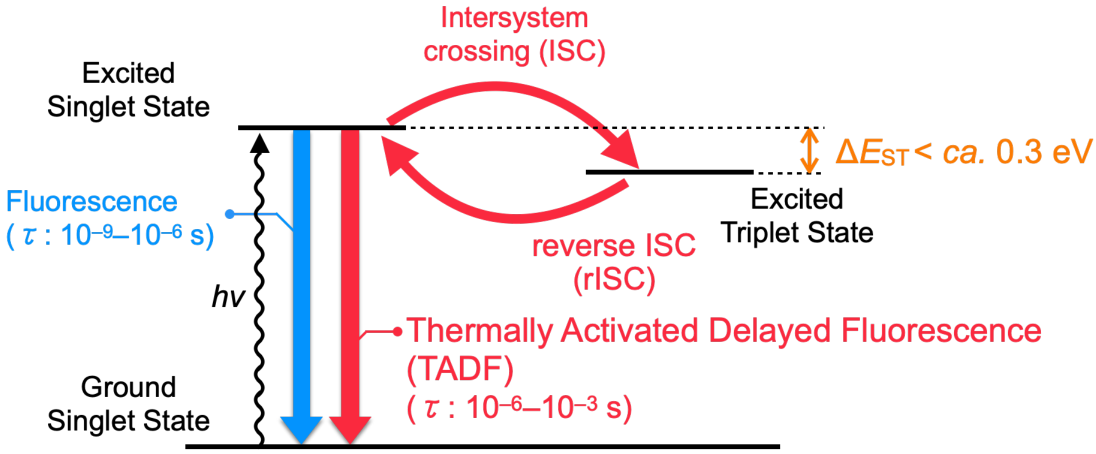

**Figure 6.** Photophysical processes in photoexcitation.

The phenomenon of TADF was reported as *E*-type delayed fluorescence in eosin by Parker and Hatchard in 1961, [15] and the first TADF-OLEDs was realized in 2009 by Adachi using $Sn^{4+}$–porphyrin complexes as the emitter.[16] However, the TADF emitters for OLEDs contain a toxic metal ion, and the TADF emission is very faint. To improve the efficiency of OLEDs, the acceleration of spin-forbidden and endothermic rISC process is crucial. To do so, it is important to enhance spin-orbit coupling (SOC), which facilitates spin inversion transition.[17] More importantly, the rISC rate ($k_{\mathrm{rISC}}$) is in inverse proportion to the energy splitting between the singlet ($S_1$) and triplet ($T_1$) states ($\Delta E_{\mathrm{ST}}$), and therefore a narrow $\Delta E_{\mathrm{ST}}$ (< *ca.* 0.37 eV)[18] is required for the efficient rISC. Since $\Delta E_{\mathrm{ST}}$ is a double electron exchange energy of the two unpaired electrons in the excited states, a narrow $\Delta E_{\mathrm{ST}}$ is achievable by minimizing the overlap between the HOMO and LUMO lobes.[17] In 2012, Adachi succeeded in developing efficient TADF-OLEDs with EQE of up to 19% employing highly twisted D–A molecules, where the HOMO and the LUMO are localized in the donors and acceptors, respectively (Figure 7).[19] Since this report, numerous TADF organic materials have been developed based on linear or branched D–A scaffolds with highly twisted dihedral angles.[20]

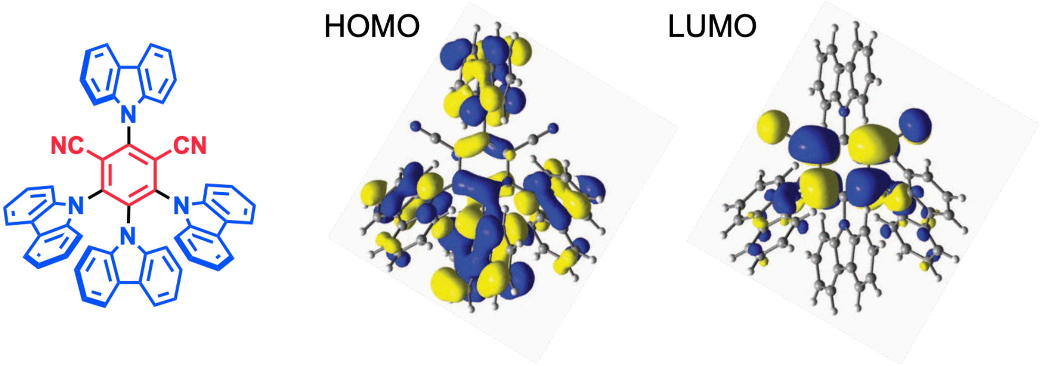

**Figure 7.** The first reported twisted D–A π-conjugated emitter for TADF-OLEDs. Adapted from ref. 19. Copyright 2012 Springer Nature.

By contrast, D−A-repeating macrocyclic TADF organic materials have been rarely explored.[21,22] In 2014, Kanbara revealed the delayed fluorescence behavior of azacalix[*n*](2,6)pyridines ($n = 3, 4$), which represent the first example of D−A-repeating organic TADF macrocycles (Figure 8a).[21] However, the large $\Delta E_{ST}$ (calc) values (> 600 meV) of the azacalixpyridines indicated that a severe thermal reverse internal conversion (rIC) from $T_1$ to $T_n$ is required for overcoming the rISC process.[21] In 2016, a purely organic deep-blue TADF emitting compound composed of triarylamines bridged with an electron-withdrawing $SO_2$ group was developed by Su and Huang (Figure 8b).[22] In these reports, only photo-excited and faint TADF phenomena in solutions and matrices were desired.[21,22] To the best of author's knowledge, any OLEDs fabricated with a macrocyclic TADF emitter have never been disclosed and evaluated. In addition, the influence of the macrocyclization of linear D−A-repeating π-conjugated systems on their physicochemical properties, especially TADF behavior, has remained unclear.

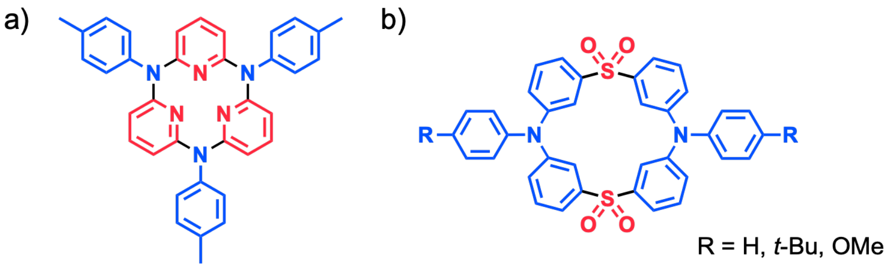

**Figure 8.** Macrocyclic TADF organic materials.

## 4. Synopsis of This Thesis

On the basis of these backgrounds, the author has designed and developed efficient TADF purely organic donor–acceptor–donor–acceptor (D–A–D–A) π-conjugated macrocycles, comprising phenylenediamine derivatives as the electron donors and dibenzo[*a*,*j*]phenazines as the electron acceptors. Furthermore, the effects of macrocyclization of a D–A–D–A scaffold and topological influence of phenylenediamine donor unit on physicochemical properties has been revealed. This Thesis consists of General Introduction, three Chapters (Figure 9), and Conclusion.

In Chapter 1, the design and synthesis of D–A–D–A π-conjugated macrocycles comprising phenylenediamine derivatives as donors and dibenzo[*a*,*j*]phenazines as acceptors are described.

In Chapter 2, the structures and fundamental physicochemical properties of D–A–D–A π-conjugated macrocycles are described.

In Chapter 3, the investigation of thermally activated delayed fluorescence properties of D–A–D–A π-conjugated macrocycles and their applications to OLEDs is described.

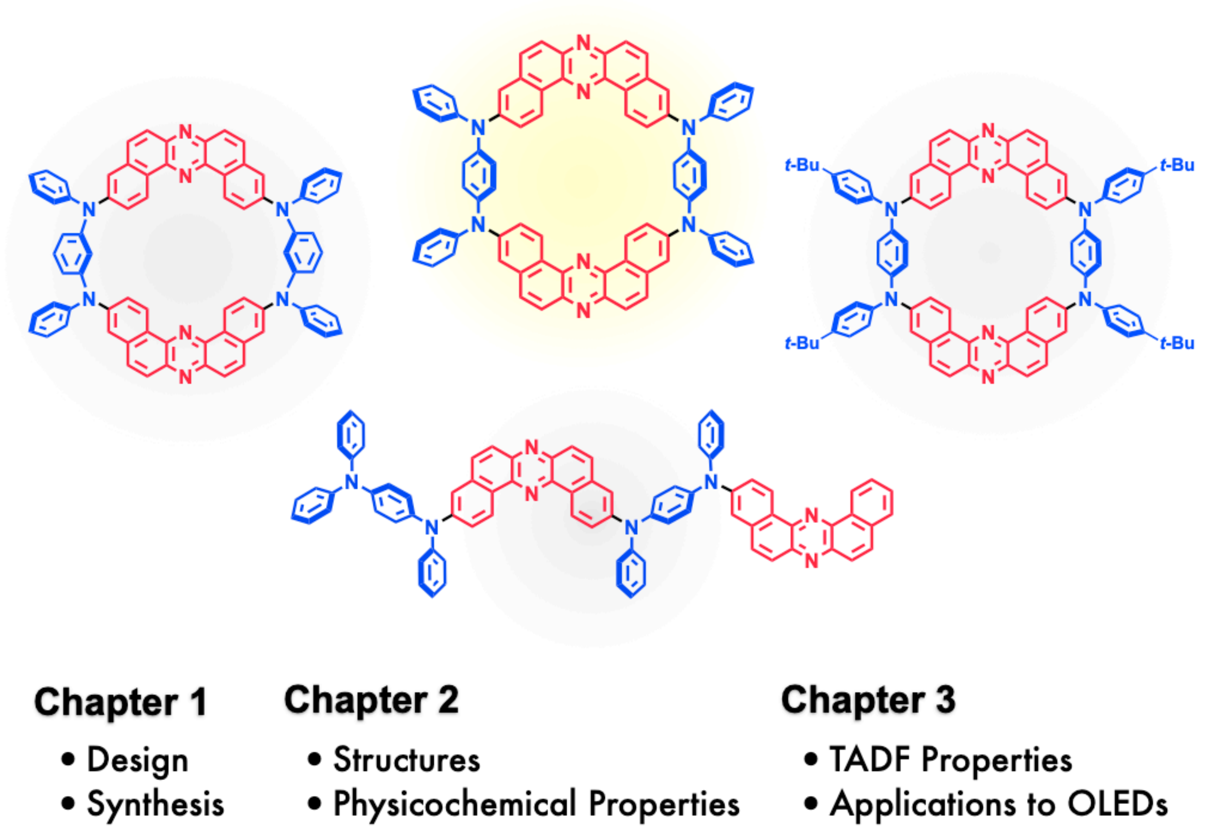

**Figure 9.** Summary of this Thesis.

## 5. References

1. (a) Sasaki, S.; Drummen, G. P. C.; Konishi, G. *J. Mater. Chem. C* **2016**, *4*, 2731–2743. (b) Misra, R.; Bhattacharyya, S. P. *Intramolecular Charge Transfer: Theory and Application;* Wiley-VCH: Weinheim, Germany, 2018.
2. Wasielewski, M. R. *Chem. Rev.* **1992**, *92*, 435–461.
3. (a) Klymchenko, A. S. *Acc. Chem. Res.* **2017**, *50*, 366–375.; (b) Chen, C.; Fang, C. *Chem. Asian J.* **2020**, *15*, 1514–1523.
4. (a) Lin, Y.; Li, Y.; Zhan, X. *Chem. Soc. Rev.* **2012**, *41*, 4245–4272. (b) Wu, Y.; Zhu, W. *Chem. Soc. Rev.* **2013**, *42*, 2039–2058.
5. Bryce, M. R. *J. Mater. Chem.* **2000**, *10*, 589–598.
6. Macrocycle is defined as “a cyclic macromolecule or a cyclic substructure of a macromolecule”, and its ring framework is usually composed of 12 or more atoms.: (a) Jenkins, A. D.; Kratochvíl, P.; Stepto, R. F. T.; Suter U. W. *Pure Appl. Chem.* **1996**, *68*, 2287–2311. (b) Parker, S. P. *McGraw-Hill Dictionary of Scientific and Technical Terms,* 6th ed.;

McGraw-Hill Education: New York, 2003; pp 1256.

7. (a) Höger, S. J. *J. Polym. Sci., Part A*: *Polym. Chem.* **1999**, *37*, 2685−2698. (b) Zhang, W.; Moore, J. S. *Angew. Chem., Int. Ed.* **2006**, *45*, 4416–4439. (c) Diederich, F.; Kivala, M. *Adv. Mater.* **2010**, *22*, 803–812. (d) Iyoda, M.; Yamakawa, J.; Rahman, M. J. *Angew. Chem., Int. Ed.* **2011**, *50*, 10522–10553. (e) Iyoda, M.; Shimizu, H. *Chem. Soc. Rev.* **2015**, *44*, 6411–6424. (f) Smith, M. K.; Miljanić, O. Š. *Org. Biomol. Chem.* **2015**, *13*, 7841–7845. (g) Lewis, S. E. *Chem. Soc. Rev.* **2015**, *44*, 2221–2304.
8. (a) Kawase, T.; Kurata, H. *Chem. Rev.* **2006**, *106*, 5250–5273. (b) Tahara, K.; Tobe, Y. *Chem. Rev.* **2006**, *106*, 5274–5290.
9. (a) Ball, M.; Nuckolls, C. *ACS Cent. Sci.* **2015**, *1*, 416–417. (b) Ball, M.; Zhang, B.; Zhong, Y.; Fowler, B.; Xiao, S.; Ng, F.; Steigerwald, M.; Nuckolls, C. *Acc. Chem. Res.* **2019**, *52*, 1068–1078.
10. (a) Chen, P.; Lalancette, R. A.; Jäkle, F. *Angew. Chem., Int. Ed.* **2012**, *51*, 7994–7998. (b) Chen, P.; Yin, X.; Baser-Kirazli, N.; Jäkle, F. *Angew. Chem., Int. Ed.* **2015**, *54*, 10768–10772.
11. (a) Darzi, E. R.; Hirst, E. S.; Weber, C. D.; Zakharov, L. N.; Lonergan, M. C.; Jasti, R. *ACS Cent. Sci.* **2015**, *1*, 335–342. (b) Kuwabara, T.; Orii, J.; Segawa, Y.; Itami, K. *Angew. Chem., Int. Ed.* **2015**, *54*, 9646–9649.
12. (a) Ball, M.; Zhong, Y.; Fowler, B.; Zhang, B.; Li, P.; Etkin, G.; Paley, D. W.; Decatur, J.; Dalsania, A. K.; Li, H.; Xiao, S.; Ng, F.; Steigerwald, M. L.; Nuckolls, C. *J. Am. Chem. Soc.* **2016**, *138*, 12861–12867. (b) Ball, M. L.; Zhang, B.; Xu, Q.; Paley, D. W.; Ritter, V. C.; Ng, F.; Steigerwald, M. L.; Nuckolls, C. *J. Am. Chem. Soc.* **2018**, *140*, 10135–10139. (c) Zhang, B.; HernándezSánchez, R.; Zhong, Y.; Ball, M.; Terban, M. W.; Paley, D.; Billinge, S. J. L.; Ng, F.; Steigerwald, M. L.; Nuckolls, C. *Nat. Commun.* **2018**, *9*, 1957.
13. For selected examples, see: (a) Luo, J.; Zhang, J. *ACS Catal.* **2016**, *6*, 873–877. (b) Mousawi, A. A.; Lara, D. M.; Noirbent, G.; Dummur, F.; Toufaily, J.; Hamieh, T.; Bui, T.-T.; Goubard, F.; Graff, B.; Gigmes, D.; Fouassier, J. P.; Lalevée, J. *Macromolecules* **2017**, *50*, 4913–4926. (c) Speckmeier, E.; Fischer, T. G.; Zeitler, K. *J. Am. Chem. Soc.* **2018**, *140*, 15353–15365.
14. For selected examples, see: (a) Xiong, X.; Song, F.; Wang, J.; Zhang, Y.; Xue, Y.; Sun, L.; Jiang, N.; Gao, P.; Tian, L.; Peng, X. *J. Am. Chem. Soc.* **2014**, *136*, 9590–9597. (b) Li, T.; Yang, D.; Zhai, L.; Wang, S.; Zhao, B.; Fu, N.; Wang, L.; Tao, Y.; Huang, W. *Adv. Sci.* **2017**, *4*, 1600166. (c) Zhu, Z.; Tian, D.; Gao, P.; Wang, K.; Li, Y.; Shu, X.; Zhu, J.; Zhao, Q. *J. Am. Chem. Soc.* **2018**, *140*, 17484–17491. (d) Ni, F.; Zhu, Z.; Tong, X.; Xie, M.; Zhao, Q.; Zhong, C.; Zou, Y.; Yang, C. *Chem. Sci.* **2018**, *9*, 6150–6155. (e) Sakar, S. K.; Pegu, M.; Behera, S.

K.; Narra, S. K.; Thilagar, P. *Chem. Asian J.* **2019**, *14*, 4588–4593. (f) Ni, F.; Zhu, Z.; Tong, X.; Zeng, W.; An, K.; Wei, D.; Gong, S.; Zhao, Q.; Zhou, X.; Yang, C. *Adv. Sci.* **2019**, *6*, 1801729. (g) Li, X.; Baryshnikov, G.; Deng, C.; Bao, X.; Wu, B.; Zhou, Y.; Ågren, H.; Zhu, L. *Nat. Commun.* **2019**, *10*, 731. (h) Zhang, Q.; Xu, S.; Li, M.; Wang, Y.; Zhang, N.; Guan, Y.; Chen, M.; Chen, C.-F.; Hu, H.-Y. *Chem. Commun.* **2019**, *55*, 5639–5642. (i) Christopherson, C. J.; Mayder, D. M.; Poisson, J.; Paisley, N. R.; Tonge, C. M.; Hudson, Z. M. *ACS Appl. Mater. Interfaces* **2020**, *12*, 20000–20011. (j) Luo, M.; Li, X.; Ding, L.; Baryshnikov, G.; Shen, S.; Zhu, M.; Zhou, L.; Zhang, M.; Lu, J.; Ågren, H.; Wang, X.-D.; Zhu, L. *Angew. Chem., Int. Ed.* **2020**, *59*, 17018–17025.

15. Parker, C. A.; Hatchard, C. G. *Trans. Faraday Soc.* **1961**, *57*, 1894–1904.
16. Endo, A.; Ogasawara, M.; Takahashi, A.; Yokoyama, D.; Kato, Y.; Adachi, C. *Adv. Mater.* **2009**, *21*, 4802–4806.
17. Dias, F. B.; Penfold, T. J.; Monkman, A. P. *Methods Appl. Fluoresc.* **2017**, *5*, 012001.
18. Leitl, M. J.; Krylova, V. A.; Djurovich, P. I.; Thompson, M. E.; Yersin, H. *J. Am. Chem. Soc.* **2014**, *136*, 16032–16038.
19. Uoyama, H.; Goushi, K.; Shizu, K.; Nomura, H.; Adachi, C. *Nature* **2012**, *492*, 234–238.
20. For selected reviews on TADF, see: (a) Tao, Y.; Yuan, K.; Chen, T.; Xu, P.; Li, H.; Chen, R.; Zheng, C.; Zhang, L.; Huang, W. *Adv. Mater.* **2014**, *26*, 7931−7958. (b) Czerwieniec, R.; Leitl, M. J.; Homeier, H. H. H.; Yersin, H. *Coord. Chem. Rev.* **2016**, *325*, 2−28. (c) Yang, Z.; Mao, Z.; Xie, Z.; Zhang, Y.; Liu, S.; Zhao, J.; Xu, J.; Chi, Z.; Aldred, M. P. *Chem. Soc. Rev.* **2017**, *46*, 915−1016. (d) Wong, M. Y.; Zysman-Colman, E. *Adv. Mater.* **2017**, *29*, 1605444. (e) Sarma, M.; Wong, K.-T. *ACS Appl. Mater. Interfaces* **2018**, *10*, 19279−19304. (f) Chen, X.-K.; Kim, D.; Brédas, J.-L. *Acc. Chem. Res.* **2018**, *51*, 2215−2224. (g) Liu, Y.; Li, C.; Ren, Z.; Yan, S.; Bryce, M. R. *Nat. Rev. Mater.* **2018**, *3*, 18020. (h) Data, P.; Takeda, Y. *Chem. Asian J.* **2019**, *14*, 1613−1636.
21. Uchida, N.; Sato, T.; Kuwabara, J.; Nishimura, Y.; Kanbara, T. *Chem. Lett.* **2014**, *43*, 459−461.
22. Hu, Y.; Wang, Z.; Jiang, X.; Cai, X.; Su, S.-J.; Huang, F.; Cao, Y. *Chem.Commun.* **2018**, *54*, 7850−7853.

# Chapter 1

# Design and Synthesis of Donor–Acceptor–Donor–Acceptor π-Conjugated Macrocycles Comprising Phenylenediamine Derivatives as Donors and Dibenzo[*a,j*]phenazines as Acceptors

## 1-1. Design of D–A–D–A Macrocycle

To design D–A–D–A π-conjugated macrocycles, the author focused on dibenzo[*a,j*]phenazine (DBPHZ) as the acceptor from the viewpoints of TADF functions and synthetic feasibility. DBPHZ is an electron-deficient aromatic compound, which is readily synthesized from 1,1’-binaphthalene-2,2’-diamines through an oxidative rearrangement.[1] Takeda, Minakata, and Data have reported that DBPHZ-cored twisted donor–acceptor–donor (D–A–D) molecules exhibit effective TADF.[2] The lowest triplet excited state ($T_1$) of the D–A–D family is exclusively localized on the DBPHZ acceptor unitss ($^3LE_A$), which allow for narrow

$\Delta E_{ST}$ by adjusting the $^1$CT energy levels through fluctuation of electronic bias and D–A dihedral angles. Given the utility of DBPHZ in TADF materials and the U-shaped structure of DBPHZ can be suitable for the formation of macrocyclic structure, the author decided to employ DBPHZ as the acceptor and designed a twisted D–A–D–A macrocycle composed of two DBPHZs (As) and two bridging electron donors (Ds). The selection of bridging donors should be crucial for synthetic feasibility, and TADF properties. The structural preorganization required for macrocyclization of a linear compound highly depends on the conformation and configuration of the precursor/intermediate. Otherwise, undesired intermolecular oligomerization/polymerization over desired intramolecular cyclization can occur.[3] Owing to the propeller-like geometries of triarylamines,[4] the incorporation of the *N*,*N*,*N*',*N*'-tetraphenylbenzene-1,4-diamine (TPDA) motif into macrocyclic structure would offer an opportunity to regulate the conformational flexibility of precursors for macrocyclization and thereby facilitate the cyclization. In addition, the bridging with a heteroatom (N) would allow for twisting of π-conjugated panels and alleviating ring strain in forming ***p*-MC**. From the above, D–A–D–A macrocycle ***p*-MC** comprising of two *p*-phenylenediamine derivatives as Ds and two DBPHZs as As was designed as TADF π-conjugated macrocycle (Figure 1).

To estimate the optimized structure and expansion of the molecular orbitals of ***p*-MC**, theoretical calculation by density functional theory (DFT) method at B3LYP/6-31+G** level using PCM (c-hex) model was conducted (Figure 2). The calculation revealed that ***p*-MC** took a saddle-shaped conformation as most stable structure (Figure 2a) with twisted donor-acceptor, as designed. HOMO and LUMO of ***p*-MC** were also localized on the donor and acceptor units (Figure 2b), as designed, and therefore, efficient TADF was expected.

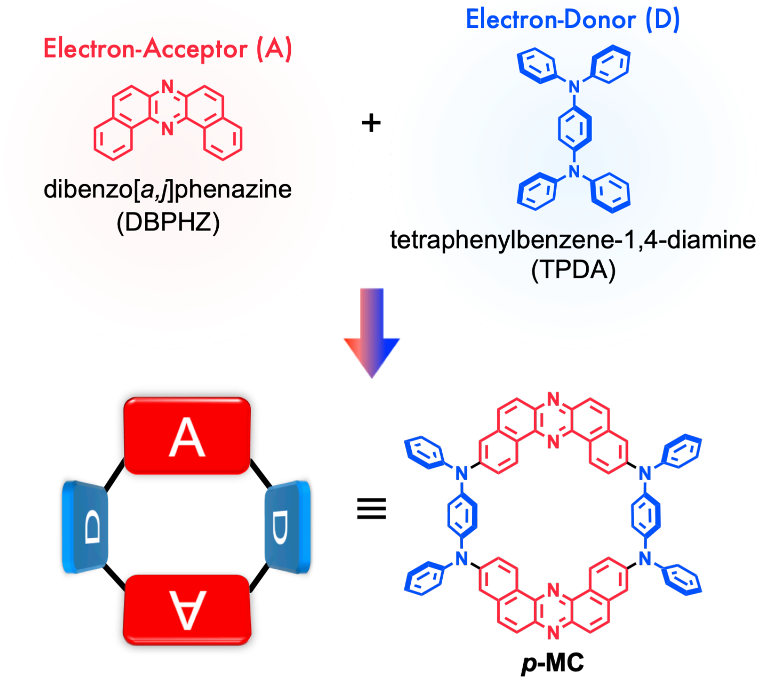

**Figure 1.** Design of D–A–D–A macrocycle ***p*-MC**.

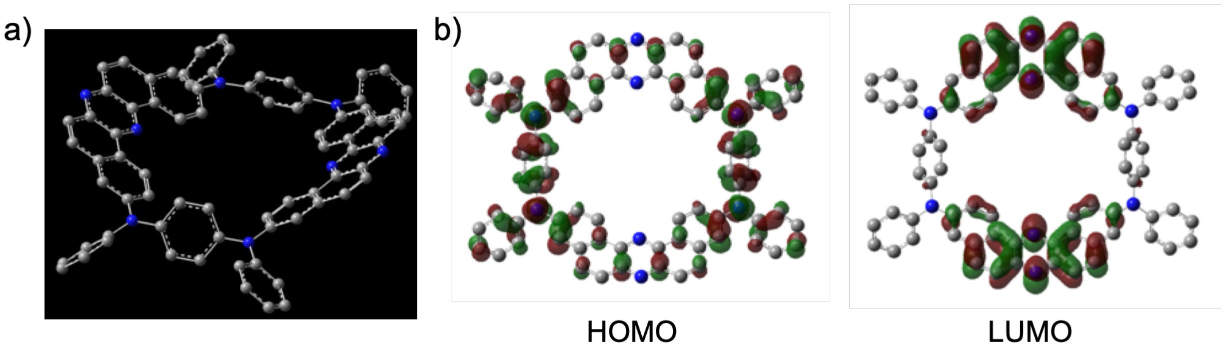

**Figure 2.** Optimized structure and frontier orbitals of ***p*-MC** by DFT calculation.

In addition to ***p*-MC,** to investigate the effect of macrocyclization of a D–A–D–A scaffold and the influence of topology in the phenylenediamine donor on its physicochemical properties, a linear analogue **Linear** (i.e., the open form of ***p*-MC**) and ***m*-MC**, which is regarded as the meta-variant of ***p*-MC**, were designed (Figure 3). Furthermore, the solubility of the macrocycle ***p*-MC** toward organic solvents, a macrocycle ***t*-Bu-MC** that have four *t*-Bu groups at the *para*-position of the exterior *N*-aromatic rings was designed (Figure 3).

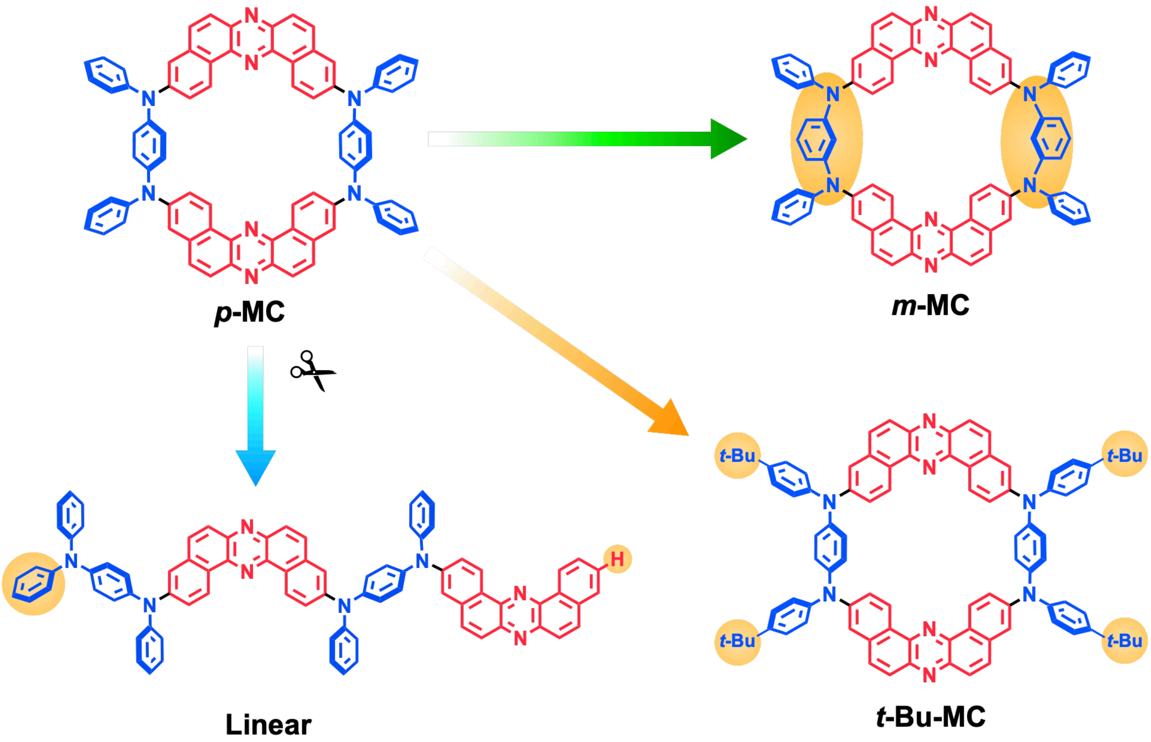

**Figure 3.** Design of D–A–D–A analogues.

### 1-2. Retrosynthesis of D–A–D–A macrocycle *p*-MC

Retrosynthetic analysis led to four synthetic routes to ***p*-MC** (Scheme 1). Route A is would be possible the most straightforward synthesis of ***p*-MC** through Buchwald-Hartwig amination of two 3,11-dibromo-dibenzo[*a*,*j*]phenazines (DBPHZ-Br$_2$) (**1**) and two $N^1$,$N^4$-diphenylbenzene-1,4-diamines (**2**). Route B involves three steps starting from diamination of DBPHZ-Br$_2$ with **5**. Route C was divided into two sub-routes (C-1 and C-2) from the common intermediate **6a**. Route C-1 includes double amination of DBPHZ-Br$_2$ **1** with two *N*-protected diamines **8a**, *N*-phenylation and macrocyclization. Route C-2 is three-step synthetic route similar to C-1. Starting from DBPHZ-Br$_2$ **1** and *N*-protected-*N*,*N*’-diphenyl-*p*-phenylenediamine **9a**, following Buchwald-Hartwig amination and de-protection, ***p*-MC** is synthesized by the cyclization using double Buchwald-Hartwig amination. These results of attempts are summarized below.

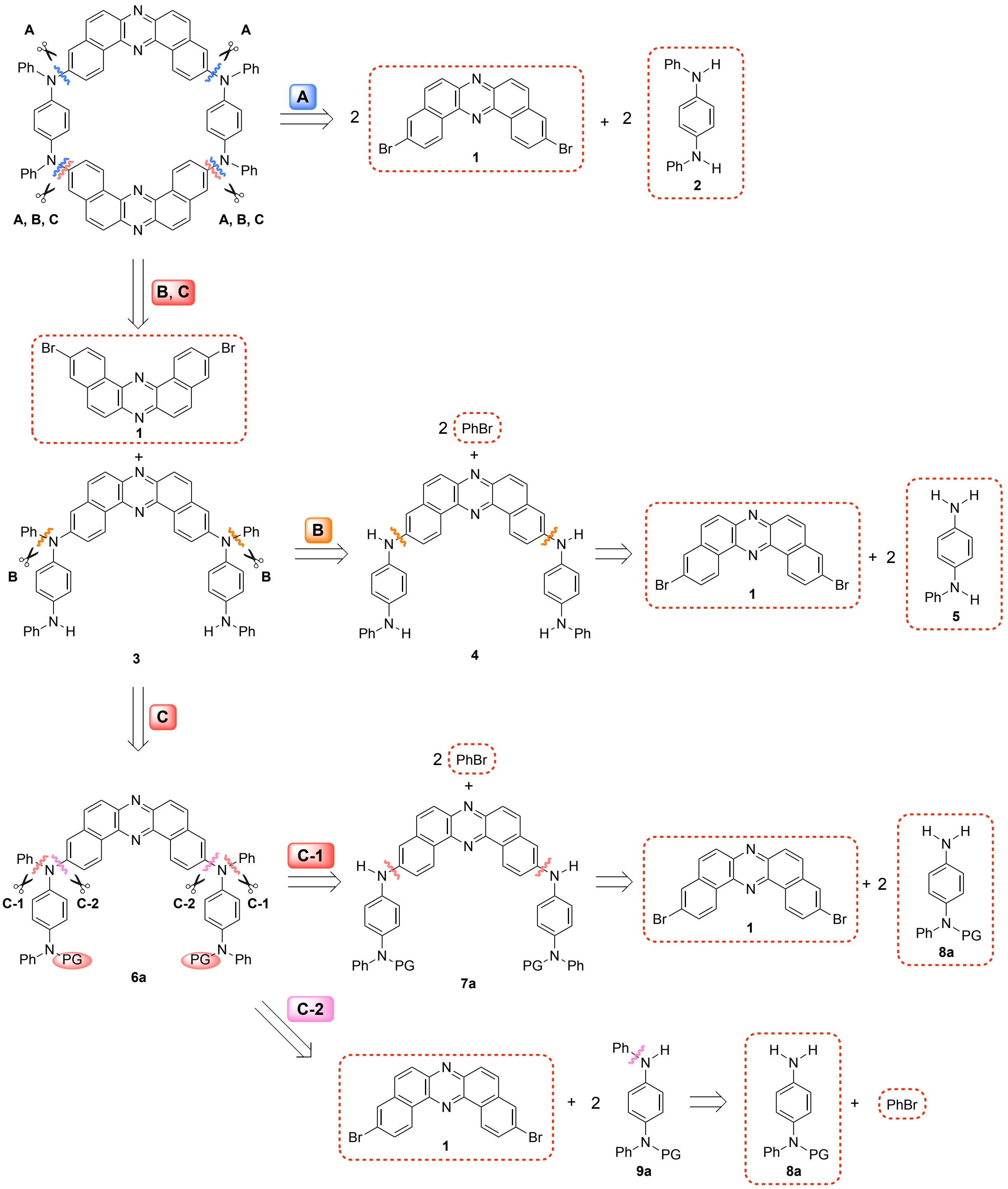

**Scheme 1.** Retrosynthetic analysis of designed ***p*-MC**.

## 1-3. Trial of Route A

One-step synthesis of ***p*-MC** was attempted from DBPHZ-Br$_2$ **1** and a commercially available diamine **2** through a Pd-catalyzed Buchwald-Hartwig amination, similar to the condition to synthesize 3,11-Bis(diphenylamino)dibenzo[*a*,*j*]phenazine from DBPHZ-$Br_2$ **1** and diphenylamine.[2b] Surprisingly, ***p*-MC** was successfully obtained in 1.7% yield (Eq. 1). However, from $^1H$ NMR analysis of the crude product, non-desired products such as oligomers/polymers, intermediates and others were major products. Since the competitive reactions to produce oligomers/polymers are difficult to suppress and the isolation of ***p*-MC** from these products was very tough, this route is considered as not suitable for synthesis of ***p*-MC**.

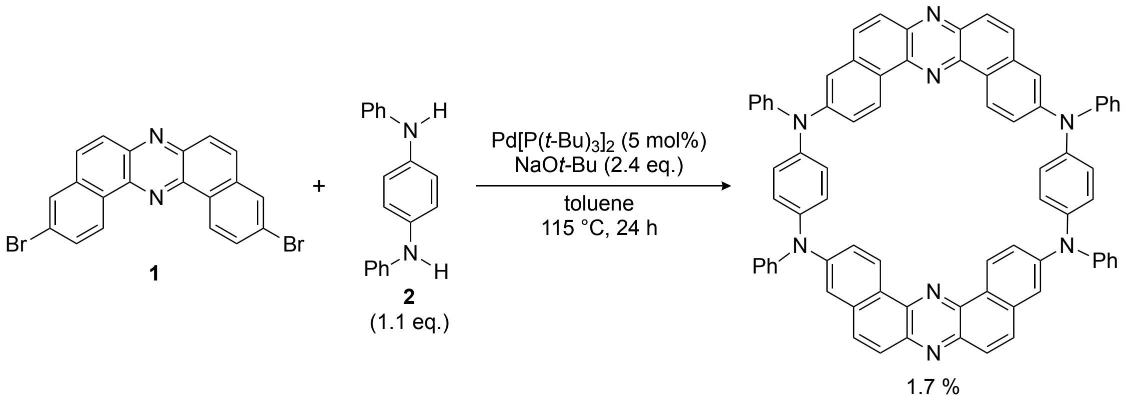

(1)

## 1-4. Trial of Route B

As the first step of this route, a Pd-catalized Buchwald-Hartwig amination of DBPHZ-$Br_2$ **1** with a commercially available *N*-phenyl-*p*-phenylenediamine (**5**) was examined (Eq. 2). $^1H$ NMR analysis of the crude product indicated that double aminated product **4** was formed, but it was not isolated due to the difficulty in separation from a number of side-reacted products such as oligomers/polymers. Accordingly, the author decided that this route was unsuitable.

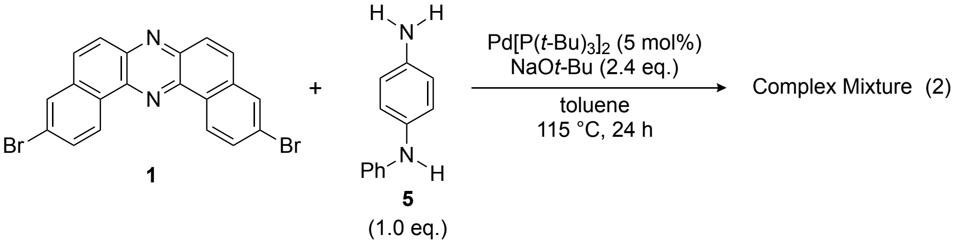

## 1-5. Trial of Route C-1

To explore the feasibility of route C-1, the author selected Boc group as a protecting group of the N-atom of the donor, because Boc group is stable towards nucleophiles and bases and can be easily deprotected under acid condition. Through a Pd-catalyzed Buchwald-Hartwig amination of DBPHZ-$Br_2$ **1** with a reported compound *tert*-butyl (4-aminophenyl)(phenyl) carbamate (**8b**), D–A–D intermediate **7b** was successfully obtained in 73% yield (Eq. 3).

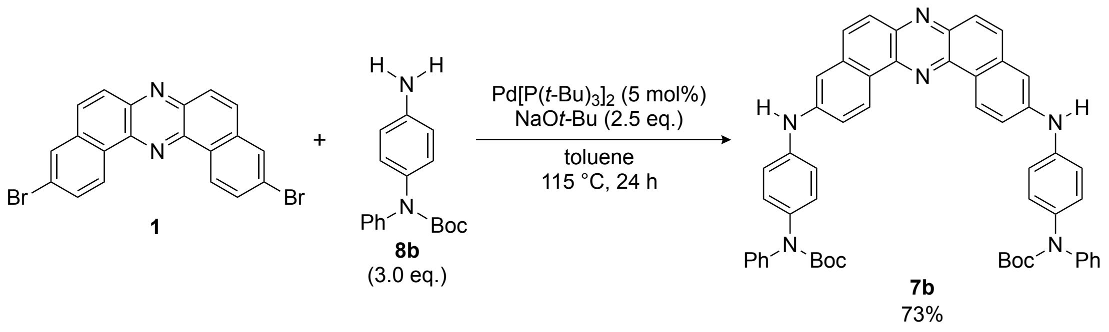

(3)

Under a similar condition with those in Eq. 3, as above reaction, *N*-phenylation of D–A–D intermediate **7b** by Pd-catalysis was conducted to give macrocycle precursor **6b** in 11% yield (not shown). The toluene was replaced with *o*-xylene as the solvent, and the reaction temperature was raised. Consequently, the yield of precursor **6b** was increased to 50% (Eq. 4). Since the two step reactions as investigated above remained in moderate yield, C-2 route was examined as an alternative route.

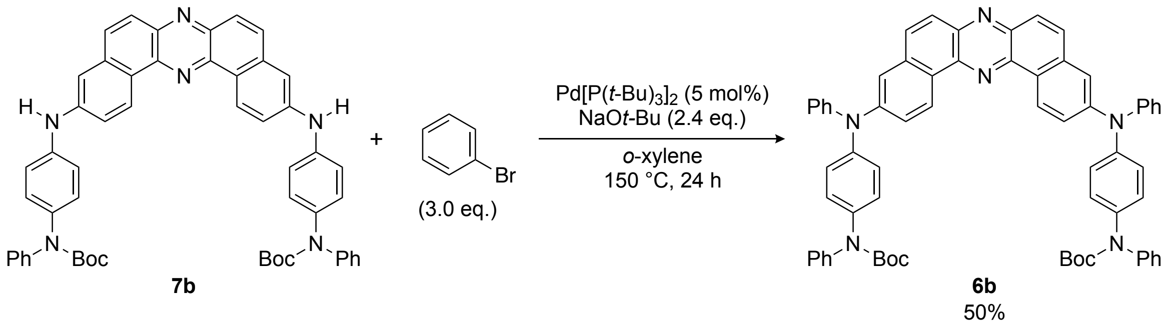

(4)

## 1-6. Trial of Route C-2

Starting from a commercially available *N*-phenyl-*p*-phenylenediamine (**5**), donor **9b** was prepared in 66% yield (in four steps), according to reported synthetic methods for oligo(*p*-aniline) compounds with a slightly modification (Scheme 2).[5,6]

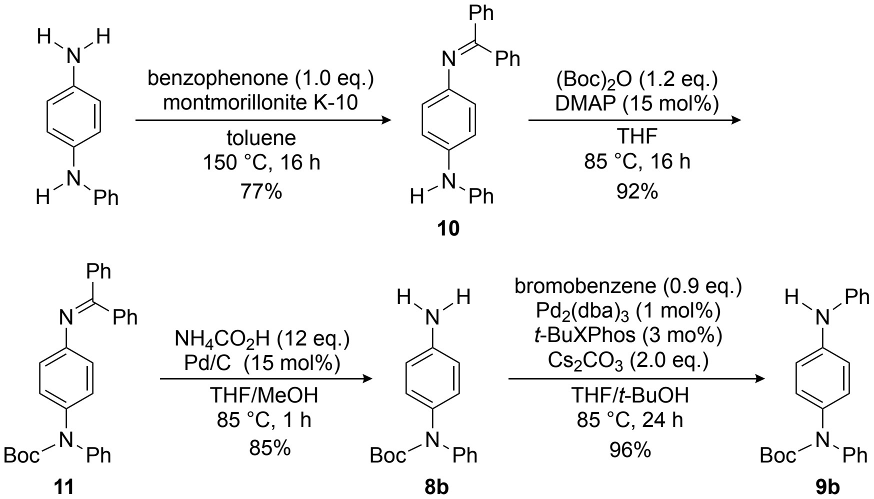

**Scheme 2.** Synthetic route to donor of ***p*-MC**.

Intermediate **6b** was obtained in a high yield by a double Pd-catalyzed Buchwald-Hartwig amination of DBPHZ-Br$_2$ **1** with the donor **9b** using a bulky phosphine ligand (QPhos) (Scheme 3).[7] The N-Boc groups of **6b** was quantitatively deprotected with an excess amount of trifluoroacetic acid (TFA) to give macrocycle precursor **3** (Scheme 3). Finally, macrocyclization was successfully achieved through a Pd-catalyzed Buchwald-Hartwig double amination of DBPHZ-Br$_2$ **1** with the D–A–D precursor **3** in 45% yield (Scheme 3), which is a relatively high yield in cyclization of aromatic components. ***p*-MC** was fully characterized by spectroscopic data (e.g., $^1$H and $^{13}$C NMR, IR, MS, and HRMS).

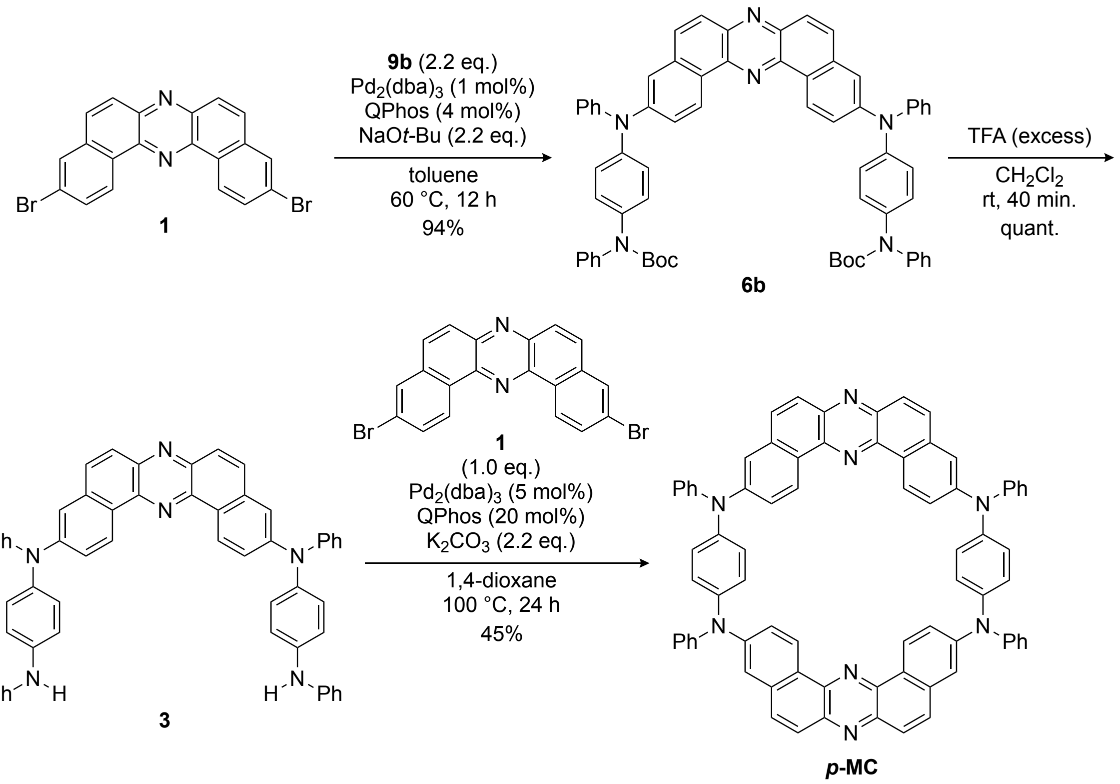

**Scheme 3.** Synthetic route to ***p*-MC**.

## 1-7. Synthesis of *t*-BuMC

Starting from 1,4-phenylenediamine, the donor having *t*-Bu groups prepared in 5 steps in a similar manner with the synthesis of ***p*-MC** donor (Scheme 4).

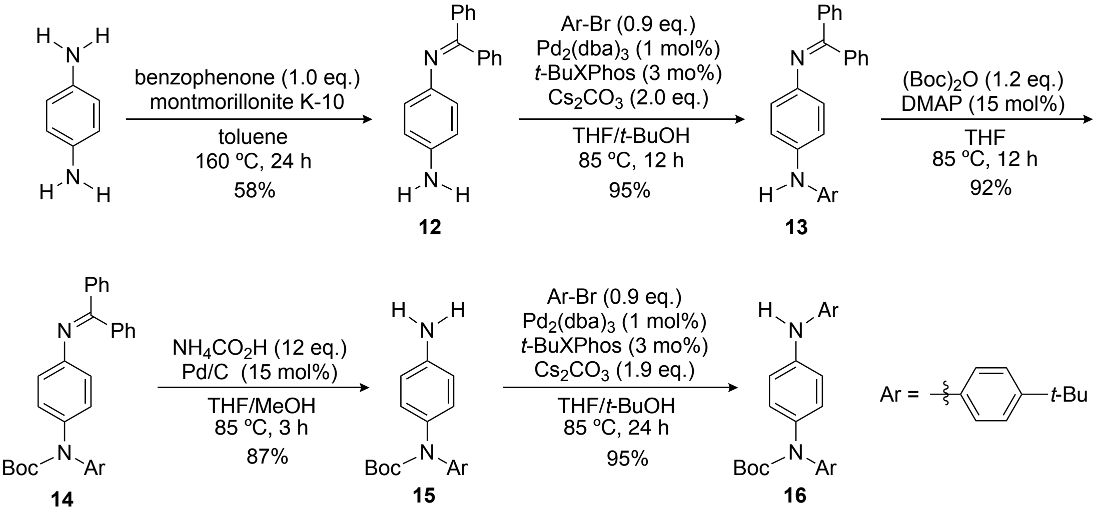

**Scheme 4.** Synthetic route to donor of ***t*-Bu-MC**.

In a similar manner with the synthesis of macrocycle ***p*-MC**, ***t*-Bu-MC** was synthesized (Scheme 5). The macrocyclization of **18** with DBPHZ-$Br_2$ **1** through a Pd-catalyzed double Buchwald-Hartwig amination gave ***t*-Bu-MC** in 30% yield, which is slightly lower than ***p*-MC**. Since *t*-Bu-substituted macrocycle precursor **18** is more soluble in organic solvents than ***p*-MC** precursor **3**, intermolecular aminative oligomerizations/polymerizations might be promoted by increasing effective concentration of precursor **18** than that of ***p*-MC** and, as the results, the yield of ***t*-Bu-MC** was lowed. ***t*-Bu-MC** was fully characterized by spectroscopic data (e.g., $^1$H and $^{13}$C NMR, IR, MS, and HRMS).

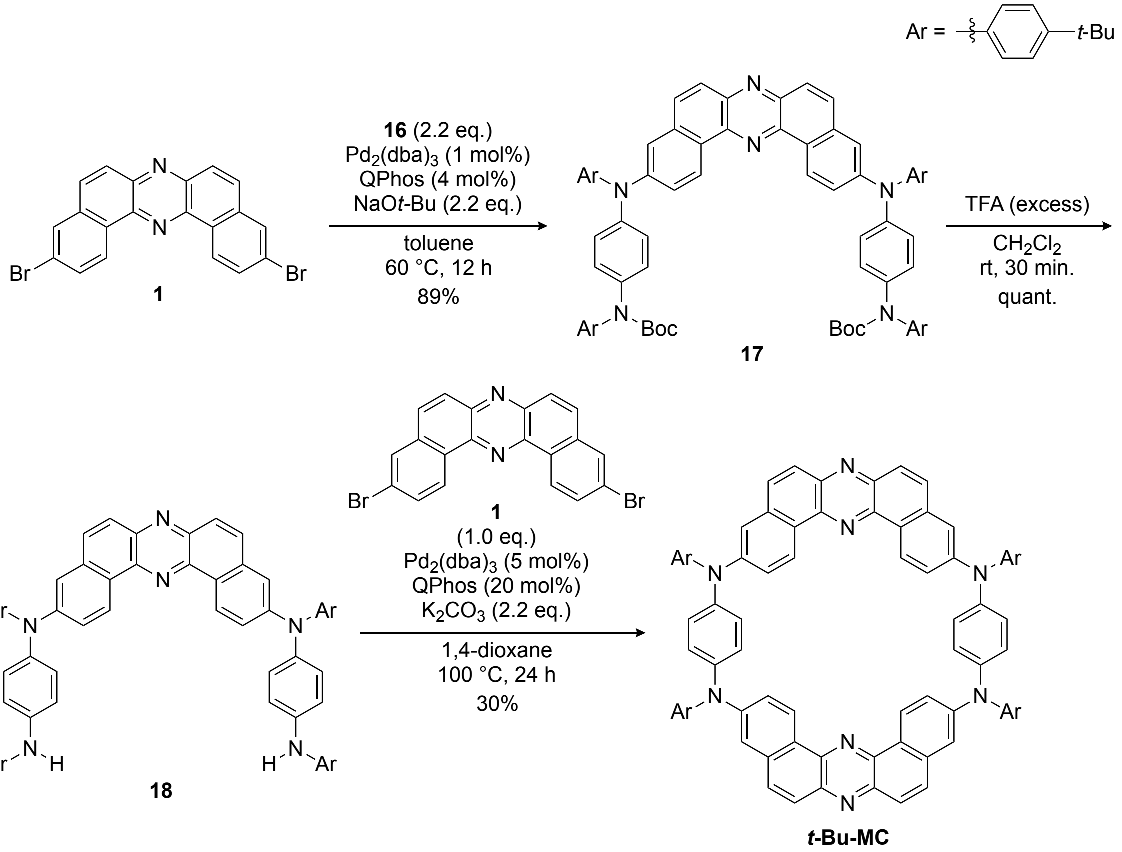

**Scheme 5.** Synthetic route to ***t*-Bu-MC**.

## 1-8. Synthesis of ***m***-MC

Unsymmetrical *m*-phenylene diamine donor **21** was efficiently prepared, starting from 3-bromo-iodobenzene in 3 steps (Scheme 6).

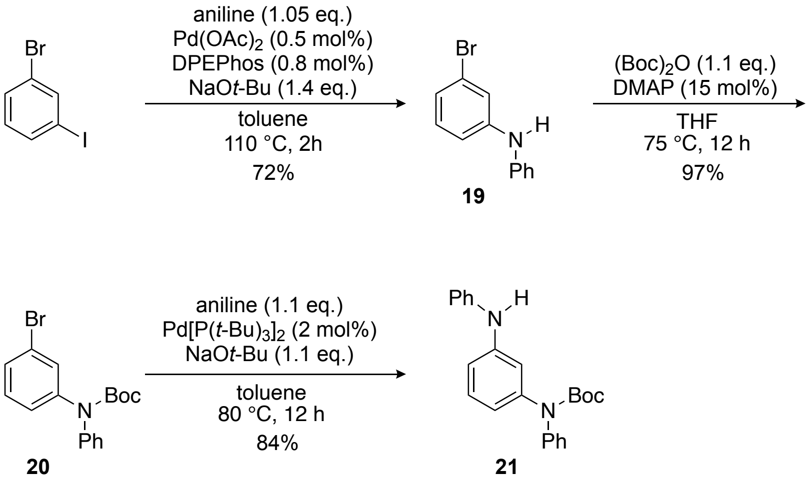

**Scheme 6.** Synthetic route to donor of ***m*-MC**.

In a similar way to the synthesis of macrocycle ***p*-MC**, ***m*-MC** was synthesized (Scheme 7). D–A–D intermediate **22** was provided in high yield through a double Pd-catalyzed Buchwald-Hartwig amination of DBPHZ-$Br_2$ **1** with the donor **21**. By the deprotection of the N-Boc groups of **22** with an excess amount of TFA, macrocycle precursor **23** was quantitatively afforded. The macrocyclization of **23** with DBPHZ-$Br_2$ **1** was completed through a Pd-catalyzed double Buchwald-Hartwig amination to give ***m*-MC** in 10% yield, which was much lower than that for ***p*-MC** (45%). Since a substantial amount of polymeric uncharacterized residue was observed in $^{1}H$ NMR chart of the crude product, this significant lowering in macrocyclization efficiency might be attributed to competition with intermolecular aminative oligomerizations/polymerizations over the desired intramolecular cyclization. ***m*-MC** was fully characterized by spectroscopic data (e.g., $^{1}H$ and $^{13}C$ NMR, IR, MS, and HRMS).

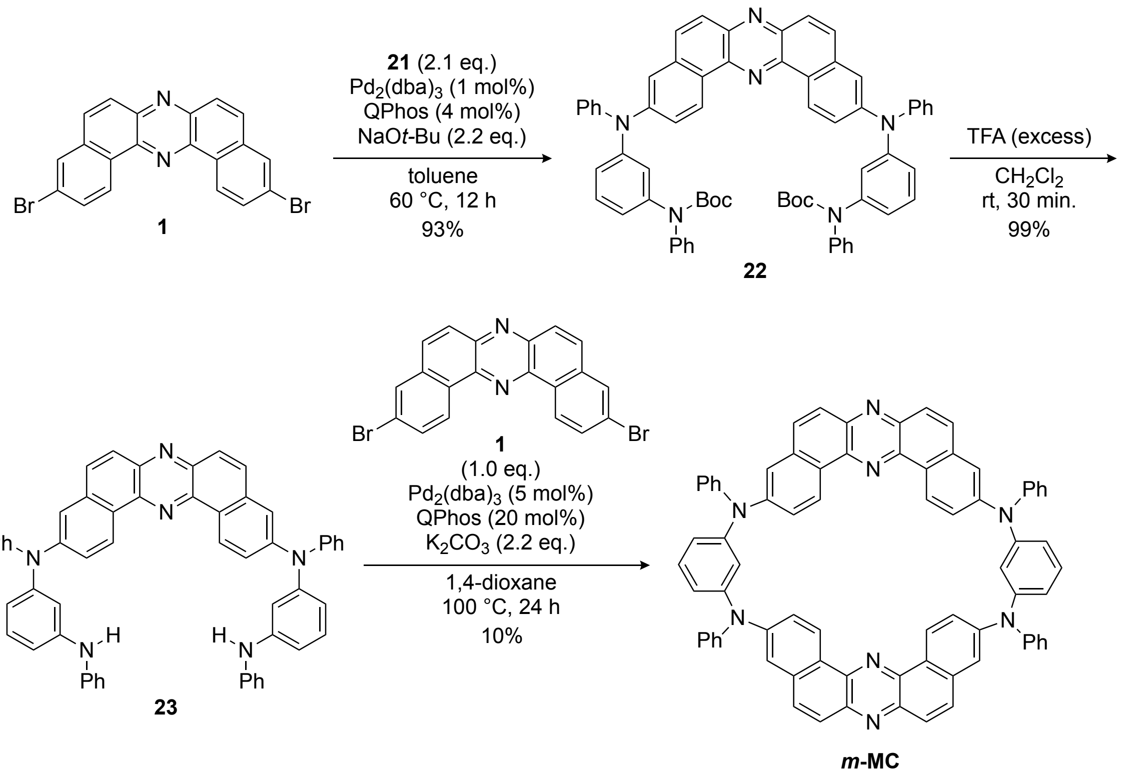

**Scheme 7.** Synthetic route to ***m*-MC**.

## 1-9. Synthesis of Linear

To synthesize the linear compound, a DBPHZ building block having a leaving group at the 3-position was required. For the purpose, dibenzo[*a*,*j*]phenazin-3-yl trifluoromethanesulfonate (DBPHZ-OTf) (**27**) was prepared (Scheme 8). Starting from a commercially available 2-bromonaphthalene, 2,2’-diamino-[1,1’-binaphthalen]-6-yltrifluoromethanesulfonate (**26**) was prepared by modifying synthetic methods for 2,2’-diamino-1,1’-biaryls.[8] DBPHZ-OTf **27** was synthesized by oxidative skeletal rearrangement of **26**.[1]

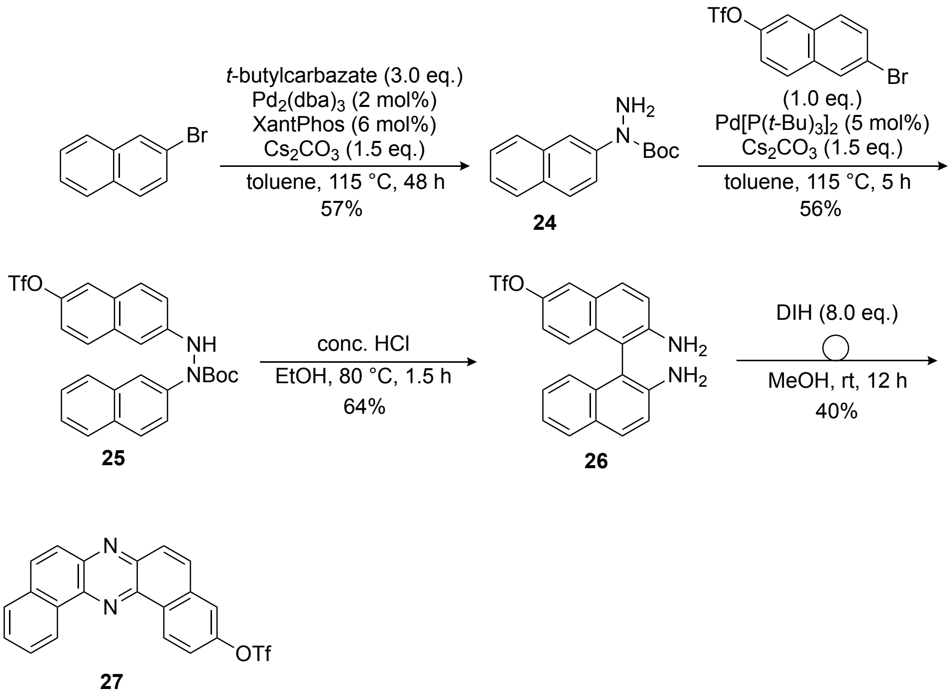

**Scheme 8.** Synthetic route to **DBPHZ-OTf**.

Monodeprotection of the N-Boc groups of ***p*-MC** intermediate **6b** with 8 equiv of TFA gave intermediate **28**. Then, *N*-phenylation of **28** with bromobenzene to provide **29** in a good yield. After the deprotection of the remaining N-Boc group of **29**, Buchwald-Hartwig amination of DBPHZ-OTf **27** with **30** gave **Linear**. **Linear** was fully characterized by spectroscopic data (e.g., $^{1}$H and $^{13}$C NMR, IR, MS, and HRMS).

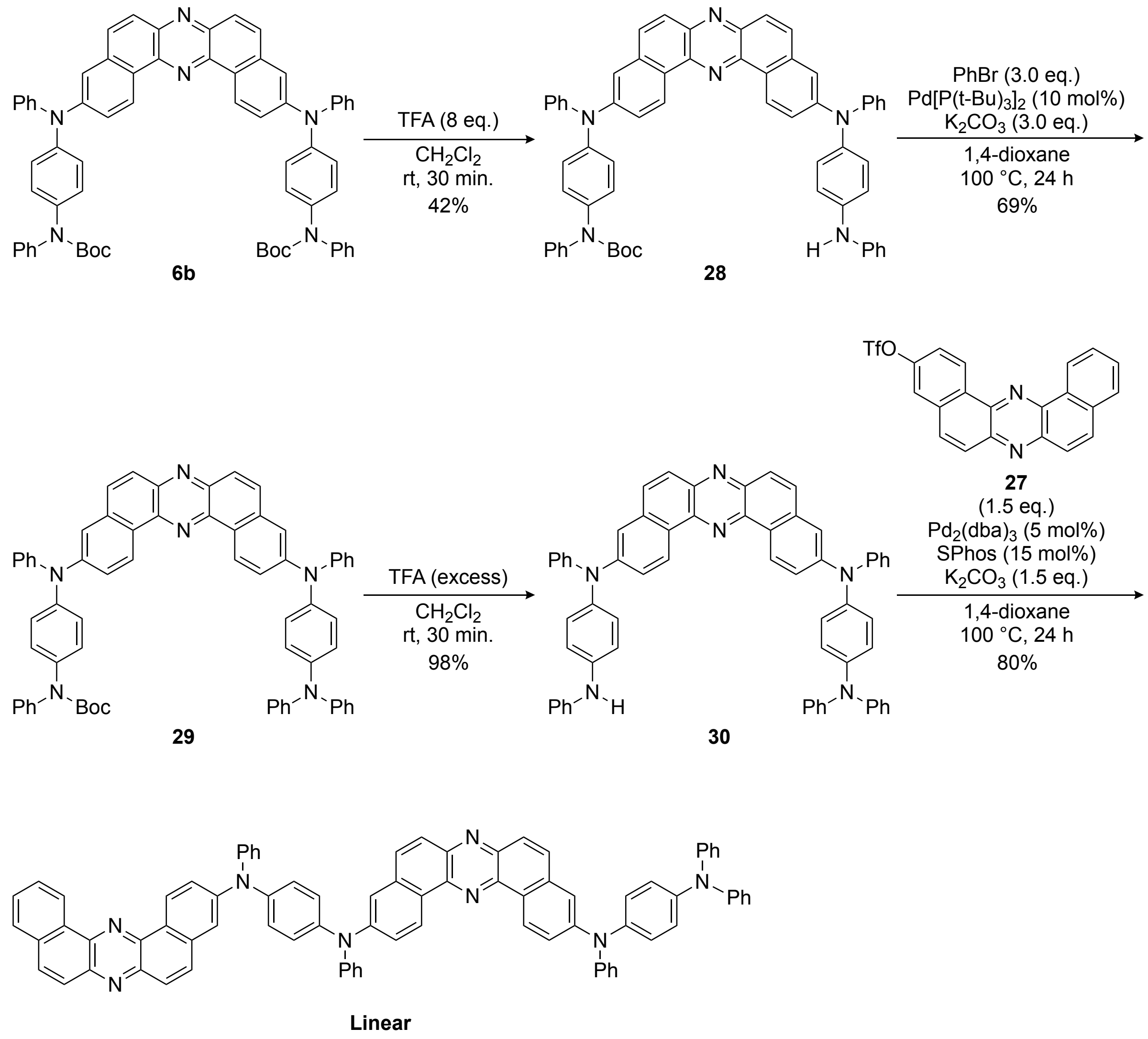

**Scheme 9.** Synthetic Route to **Linear**.

## 1-10. Summary

In Chapter 3, D–A–D–A π-conjugated macrocycle ***p*-MC** comprising *p*-phenylenediamine derivatives as electron-donors and dibenzo[*a*,*j*]phenazines as electron-acceptors was designed. In addition to ***p*-MC**, to investigate macrocyclization of a D–A–D–A scaffold and the influence of topology in the phenylenediamine donor on its physicochemical properties, a linear analogue **Linear** and ***m*-MC**, which is regarded as the *meta*-variant of ***p*-MC**, were designed. Moreover, to increase the solubility of a macrocycle, ***t*-Bu-MC** which have four *t*-Bu groups at the *para*-position of the exterior *N*-aromatic rings was designed. ***p*-MC** was succeeded in synthesizing from 3,11-dibromo-dibenzo[*a*,*j*]phenazine (**1**) and *tert*-butyl phenyl(4-(phenylamino)phenyl)carbamate (**9b**) in three steps. ***m*-MC** and ***t*-Bu-MC** was also synthesized, according to the same route as ***p*-MC**. **Linear** could be obtained from the intermediate of ***p*-MC** in four steps.

## 1-11. Experimental Section

### General Remarks.

All reactions were carried out under an atmosphere of nitrogen unless otherwise noted. Products were purified by chromatography on silica gel BW-300 and Chromatorex NH (Fuji Silysia Chemical Ltd.). Analytical thin-layer chromatography (TLC) was performed on pre-coated silica gel glass plates (Wako silicagel 70 FM TLC plate and Fuji Silysia Chromatorex NH, 0.25 mm thickness). Compounds were visualized with UV lamp. Melting points were determined on a Stanford Research Systems MPA100 OptiMelt Automated Melting Point System or a DSC 6220 (SII) system. All $^{1}$H, $^{13}$C and $^{19}$F NMR spectra except for ***p*-MC**, **Linear**, ***t*-Bu-MC** and ***m*-MC** were recorded on a JEOL JMTC-400/54/SS Spectrometer ($^{1}$H NMR, 400 MHz; $^{13}$C NMR, 100 MHz, $^{19}$F NMR, 377 MHz) using tetramethylsilane as an internal standard for $^{1}$H and $^{13}$C NMR and hexafluorobenzene as an external standard for $^{19}$F NMR. $^{1}$H and $^{13}$C NMR spectra of ***p*-MC** and ***m*-MC** and $^{13}$C NMR specta of **Linear** and ***t*-Bu-MC** were recorded on a Bruker AVANCE III 600 Spectrometer ($^{1}$H NMR, 600 MHz; $^{13}$C NMR, 151 MHz) using tetramethylsilane as an internal standard. Infrared spectra were acquired on a SHIMADZU IRAffinity-1 FT-IR Spectrometer. Mass spectra and high-resolution mass spectra were obtained on a JEOL JMS-700 Mass Spectrometer. The elemental analysis (CHN) was carried out with JM10 (J-SCIENCE LAB CO., Ltd).

## Materials.

Dehydrated THF, toluene, $CH_2Cl_2$ and 1,4-dioxane were used as received. Methanol and *tert*-butanol were dried with 3A molecular sieves before used. 3,11-dibromo-dibenzo[*a*,*j*]phenazine [CAS No. 1620543-64-7][1] and 6-bromo-2-naphthyltrifluoro-methansulfonnate [CAS No. 151600-02-1][9] were synthesized according to the reported procedure.

## Synthetic Procedures and Spectroscopic Data.

### 4-((diphenylmethylene)amino)-*N*-phenylaniline (10) [226713-32-2]

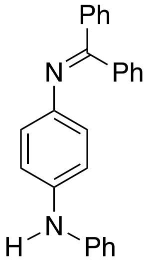

The title compound **10** was prepared according to a similar method reported in the literature[5] with a slight modification. Montmorillonite was dried at 130 °C under reduced pressure for half a day. Three-necked round bottom flask (200 mL) equipped with a magnetic stir bar, glass stoppers and a Dean-Stark apparatus, was evacuated and refilled with $N_2$ gas for three times. *p*-Aminodiphenylamine (9.21 g, 50 mmol), benzophenone (9.11g, 50 mmol, 1.0 equiv), montmorillonite K-10 (4.0 g) and toluene (100 mL) were added to the flask under a stream of $N_2$ gas at room temperature, and the resulting mixture was stirred at 150 °C for 16 h. The solvent was removed under reduced pressure, and the residue was purified by flash column chromatography on silica gel (eluent: *n*-hexane/EtOAc 95:5–8:2) to give product **10** as yellow solid in 77% yield (13.4 g, 38.5 mmol); mp 123.6–124.2 °C; $R_f$ 0.20 (*n*-hexane/EtOAc 8:2, NH silica); $^1$H NMR (400 MHz, $CDCl_3$) δ 7.73 (d, $J$ = 7.6 Hz, 2H), 7.48–7.38 (m, 3H), 7.31–7.15 (m, 7H), 6.95 (d, $J$ = 7.6 Hz, 2H), 6.90–6.84 (m, 3H), 6.68 (d, $J$ = 8.4 Hz, 2H), 5.55 (brs, 1H); $^{13}$C NMR (100 MHz, $CDCl_3$): δ 167.6, 145.1, 143.7, 140.0, 138.5, 136.6, 130.5, 129.6, 129.23, 129.17, 128.5, 128.1, 128.0, 122.6, 120.2, 118.8, 116.8; IR (ATR, cm$^{-1}$): 3383, 3040, 1609, 1591, 1566, 1506, 1491, 1441, 1310, 1287, 1242, 1223, 1171, 1155, 1072, 1026, 959, 914, 827, 800, 785, 766, 746, 729; MS (EI$^+$): m/z (relative intensity, %): 349 ([M+1]$^+$, 28), 348 (M$^+$, 100), 271 ([M–Ph]$^+$, 33), 167 ([$C_{12}H_9N$]$^+$, 26); HRMS (EI$^+$): m/z calcd for $C_{25}H_{20}N_2$ (M) 348.1626, found 348.1621.

***tert*-butyl (4-((diphenylmethylene)amino)phenyl)(phenyl)carbamate (11) [535960-10-2]**

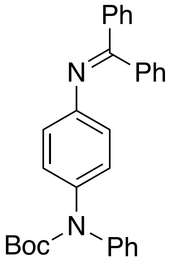

The title compound **11** was prepared according to a similar method reported in the literature[5] with a slight modification. Three-necked round bottom flask (200 mL) equipped with a magnetic stir bar, was added **10** (12.20 g, 35 mmol) under the air. The flask was capped with glass stoppers, and evacuated and refilled with $N_2$ gas for three times. THF (140 mL), di-*tert*-butyl dicarbonate (9.19 mg, 42 mmol, 1.2 equiv), and DMAP (640 mg, 5.2 mmol, 15 mol%) were added to the flask under a stream of $N_2$ gas at room temperature, and the resulting mixture was stirred at 85 °C for 16 h. The solvent was removed under reduced pressure, and the residue was purified by flash column chromatography on silica gel (eluent: *n*-hexane/EtOAc 10:0–9:1) to give product **11** as pale-yellow solid in 92% yield (14.4 g, 32 mmol). Spectroscopic data were in good agreement with those previously reported:[6] $^1$H NMR (400 MHz, $CDCl_3$) δ 7.74 (d, $J$ = 7.2 Hz, 2H), 7.47 (t, $J$ = 7.2 Hz, 1H), 7.40 (t, $J$ = 7.4 Hz, 2H), 7.30–7.24 (m, 5H), 7.16–7.10 (m, 5H), 6.97 (d, $J$ = 8.8 Hz, 2H), 6.67 (d, $J$ = 8.8 Hz, 2H), 1.40 (s, 9H); $^{13}$C NMR (100 MHz, $CDCl_3$): δ 168.7, 153.8, 149.1, 143.1, 139.5, 138.3, 136.1, 130.8, 129.5, 129.3, 128.6, 128.5, 128.2, 127.9, 127.5, 126.2, 125.1, 121.4, 80.9, 28.2.

***tert*-butyl (4-aminophenyl)(phenyl)carbamate (8b) [409357-04-6]**

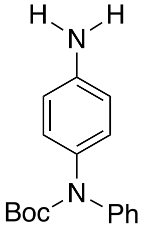

The title compound **8b** was prepared according to a similar method reported in the literature[5] with a slight modification. Three-necked round bottom flask (100 mL) equipped with a magnetic stir bar, was added **11** (3.14 g, 7.0 mmol) under the air. The flask was capped with glass stoppers, and evacuated and refilled with $N_2$ gas for three times. To the flask, ammonium formate (5.29 g, 84 mmol, 12 equiv), 10% Pd/C (1.12 g, 1.1 mmol based on Pd, 15 mol% based on Pd), THF (14 mL) and MeOH (21 mL) were added under a stream of $N_2$ gas at room temperature, and the resulting mixture was stirred at 85 °C for 1 h. The solution was filtered through a Celite pad, and the solvent was removed under reduced pressure to give solid residue. The solid was washed by *n*-hexane and filtered to give product **8b** as white solid in 97% yield (1.93 g, 6.79 mmol). mp 146.9–147.7 °C; $R_f$ 0.25 (*n*-hexane/EtOAc 6:4, NH silica); $^1$H NMR (400 MHz, $CDCl_3$) δ 7.29–7.20 (m, 4H), 7.11 (t, $J$ = 7.2 Hz, 1H), 6.99 (d, $J$ = 8.8 Hz, 2H), 6.63 (d, $J$ = 8.8 Hz, 2H), 3.65 (brs, 2H) 1.44 (s, 9H); $^{13}$C NMR (100 MHz, $CDCl_3$): δ 154.2, 144.4, 143.4, 134.1, 128.5, 128.4, 126.2, 125.0, 115.2, 80.7, 28.2; IR (ATR, $cm^{-1}$): 3443, 3352, 3003, 2984, 1678, 1628, 1595, 1518, 1491, 1356, 1308, 1275, 1225, 1161, 1057, 1026, 1015, 959, 845, 802, 756; MS (EI$^+$): m/z (relative intensity, %): 284 (M$^+$, 10), 228 ([M+1–*t*-Bu]$^+$, 55), 184 ([M+1–Boc]$^+$, 100), 183 ([M–Boc]$^+$, 32), 57 ([*t*-Bu]$^+$, 14); HRMS (EI$^+$): m/z calcd for $C_{17}H_{20}N_2O_2$ (M) 284.1525, found 284.1523.

***tert*-butyl phenyl(4-(phenylamino)phenyl)carbamate (9b)**

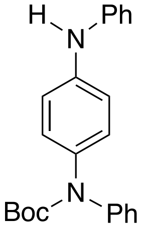

The title compound **9b** was prepared according to a similar method reported in the literature[6] with a slight modification. In a glovebox, to a three-necked round bottom flask (200 mL) equipped with a magnetic stir bar and a rubber septum, was added *t*-BuXPhos (127.1 mg, 0.30 mmol, 3.0 mol%), and the flask was sealed with a rubber septum. To the flask, **8b** (3.12 g, 11 mmol, 1.1 equiv), bromobenzene (1.54 g, 9.8 mmol), $Pd_2(dba)_3$ (91.0 mg, 0.10 mmol, 1.0 mol%), THF (20 mL) and *t*-BuOH (10 mL) were added. The solution was degassed through the freeze-pump-thaw cycling for three times and stirred at 85 °C for 24 h. De-ionized water (20 mL) was added to the reaction mixture, and the organic layer was extracted with $CH_2Cl_2$ (40 mL × 3). The combined organic extracts were dried over $Na_2SO_4$ which was purified by flash column chromatography on NH silica gel (eluent: *n*-hexane/EtOAc 10:0–8:2) to give **9b** as pale-yellow solid in 96% yield (3.39 g, 9.40 mmol). mp 94.6–95.2 °C; $R_f$ 0.23 (*n*-hexane/EtOAc 8:2, NH silica); $^1$H NMR (400 MHz, $CDCl_3$): δ 7.32–7.22 (m, 6H), 7.15 (t, *J* = 7.2 Hz, 1H), 7.10 (d, *J* = 8.8 Hz, 2H), 7.05 (d, *J* = 7.6 Hz, 2H), 7.00 (d, *J* = 8.8 Hz, 2H), 6.92 (t, *J* = 7.6 Hz, 1H), 5.70 (brs, 1H), 1.46 (s, 9H); $^{13}$C NMR (100 MHz, $CDCl_3$): δ 154.1, 143.2, 142.9, 140.9, 136.0, 129.3, 128.6, 128.1, 126.6, 125.3, 121.0, 117.8, 117.7, 80.9, 28.2; IR (ATR, cm$^{-1}$): 3333, 2978, 1684, 1595, 1518, 1491, 1472, 1456, 1354, 1308, 1288, 1279, 1248, 1229, 1161, 1057, 1028, 849, 802, 756, 737; MS (FAB$^+$, NBA): m/z (relative intensity, %): 361 ([M+H]$^+$, 40), 360 ([M]$^+$, 90), 305 ([M+H–*t*-Bu]$^+$, 81), 304 ([M–*t*-Bu]$^+$, 100), 260 ([M+H–Boc]$^+$, 32), 259 ([M–Boc]$^+$, 42), 57 ([*t*-Bu]$^+$, 38); HRMS (FAB$^+$, NBA): m/z calcd for $C_{23}H_{24}N_2O_2$ (M) 360.1838, found 360.1844.

**di-*tert*-butyl ((dibenzo[*a*,*j*]phenazine-3,11-diylbis(phenylazanediyl))bis(4,1-phenylene)) bis(phenylcarbamate) (6b)**

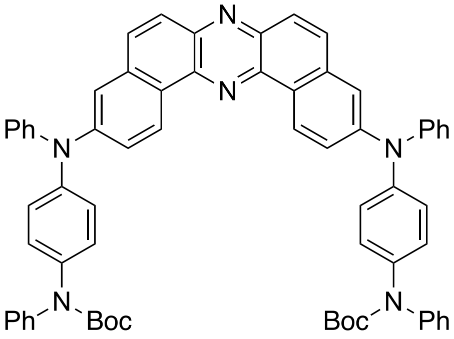

The intermediate **6b** was prepared according to a similar method reported in the literature[7] with a slight modification. Toluene was degassed through freeze-pump-thaw cycling for three times before used. In a glovebox, to a two-necked reaction tube (10 mL) equipped with a magnetic stir bar, NaO*t*-Bu (83.8 mg, 0.87 mmol, 2.2 equiv) was added, and the tube was sealed with a rubber septum. Outside the glovebox, DBPHZ-$Br_2$ **1** (175.5 mg, 0.40 mmol), donor **9b** (318.5 mg, 0.88 mmol, 2.2 equiv), $Pd_2(dba)_3$ (3.8 mg, 4.1 µmol, 1.0 mol%), QPhos (11.3 mg, 16 µmol, 4.0 mol%), and toluene (3 mL) were added under a stream of $N_2$ gas at room temperature, and the resulting mixture was stirred at 60 °C for 12 h. De-ionized water (5 mL) was added to the reaction mixture, and the organic layer was extracted with $CH_2Cl_2$ (20 mL × 3). The combined organic extracts were dried over $Na_2SO_4$, which was purified by flash column chromatography on NH silica gel (eluent: *n*-hexane/EtOAc 95:5–9:1). After dried in a vacuum oven at 120 °C for 2 h, product **6b** was obtained as orange solid in 94% yield (372.8 mg, 0.37 mmol). mp 154.9 °C; $R_f$ 0.33 (*n*-hexane/EtOAc 7:3, NH silica); $^1$H NMR (400 MHz, $CDCl_3$): δ 9.35 (d, *J* = 8.8 Hz, 2H), 7.94 (d, *J* = 9.2 Hz, 2H), 7.79 (d, *J* = 9.2 Hz, 2H), 7.54 (dd, *J* = 8.8, 2.4 Hz, 2H), 7.52 (d, *J* = 2.4 Hz, 2H), 7.38–7.11 (m, 28H), 1.48 (s, 18H); $^{13}$C NMR (100 MHz, $CDCl_3$): δ 154.0, 148.7, 147.2, 144.7, 142.9, 141.8, 140.8, 138.5, 134.6, 131.5, 129.6, 128.8, 127.9, 127.4, 127.1, 126.2, 125.9, 125.8, 125.2, 125.0, 123.9, 123.3, 119.7, 81.2, 28.3; IR (ATR, $cm^{-1}$): 1711, 1593, 1506, 1491, 1474, 1354, 1339, 1312, 1302, 1287, 1277, 1258, 1159; MS (FAB$^+$, NBA): m/z (relative intensity, %): 997 ($[M+H]^+$, 34), 996 ($M^+$, 22), 885 ([M+3H–*t*-Bu×2]$^+$, 13), 884 ([M+2H–*t*-Bu×2]$^+$, 10), 796 ([M+2H–Boc×2]+, 12), 795 ([M+H–Boc×2]$^+$, 10), 167 ($[C_{12}H_9N]^+$, 19), 89 ($[C_7H_5]^+$, 8), 77 ($[C_6H_5]^+$, 18), 57 ([*t*-Bu]$^+$, 100); HRMS (FAB$^+$, NBA): m/z calcd for $C_{66}H_{56}N_6O_4$ (M) 996.4346, found 996.4354.

### $N^1$,$N^{1'}$-(dibenzo[*a*,*j*]phenazine-3,11-diyl)bis($N^1$,$N^4$-diphenylbenzene-1,4-diamine) (3)

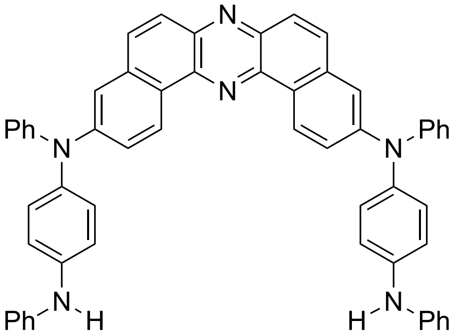

To a round-bottomed flask (50 mL) equipped with a magnetic stir bar, were added **6b** (349.0 mg, 0.35 mmol), dehydrated $CH_2Cl_2$ (4.8 mL), and TFA (1.2 mL, 15.7 mmol, 45 equiv). The resulting mixture was stirred at room temperature for 40 min. Saturated aqueous $NaHCO_3$ solution was added to the reaction mixture, and the organic layer was extracted with $CH_2Cl_2$ (20 mL × 3). The combined organic extracts were dried over $Na_2SO_4$, which was purified by flash column chromatography on NH silica gel (eluent: *n*-hexane/EtOAc 95:5–0:10). After dried in a vacuum oven at 140 °C for 2 h, product **3** was quantitatively obtained as red-orange solid (276.2 mg, 0.35 mmol). mp 219.5 °C (dec.); $R_f$ 0.33 (*n*-hexane/EtOAc 5:5, NH silica); $^1$H NMR (400 MHz, $CDCl_3$): δ 9.33 (d, $J$ = 8.8 Hz, 2H), 7.93 (d, $J$ = 9.2 Hz, 2H), 7.78 (d, $J$ = 9.2 Hz, 2H), 7.54 (dd, $J$ = 8.8, 2.4 Hz, 2H), 7.46 (d, $J$ = 2.8 Hz, 2H), 7.35–7.23 (m, 14H), 7.17 (d, $J$ = 8.8 Hz, 4H), 7.06–7.13 (m, 10H), 6.94 (t, $J$ = 7.2 Hz, 2H), 5.73 (brs, 2H); $^{13}$C NMR (100 MHz, $CDCl_3$): δ 149.1, 147.4, 143.1, 141.6, 140.9, 140.5, 139.8, 134.6, 131.5, 129.41, 129.39, 127.4, 127.3, 126.1, 125.2, 124.4, 122.4, 120.9, 119.1, 118.3, 117.6; IR (ATR, $cm^{-1}$): 1591, 1474, 1360, 1350, 1310, 1279, 1260, 1144, 872, 799, 760, 745; MS (FAB$^+$, NBA): m/z (relative intensity, %): 797 ([M+H]$^+$, 12), 796 (M$^+$, 14), 89 ([$C_7H_5$]$^+$, 14), 77 ([$C_6H_5$]$^+$, 14); HRMS (FAB$^+$, NBA): m/z calcd for $C_{56}H_{40}N_6$ (M) 796.3314, found 796.3298.

### 2,4,6,8-tetraphenyl-2,4,6,8-tetraaza-1,5(3,11)-didibenzo[*a*,*j*]phenazina-3,7(1,4)-dibenzenacyclooctaphane (*p*-MC)

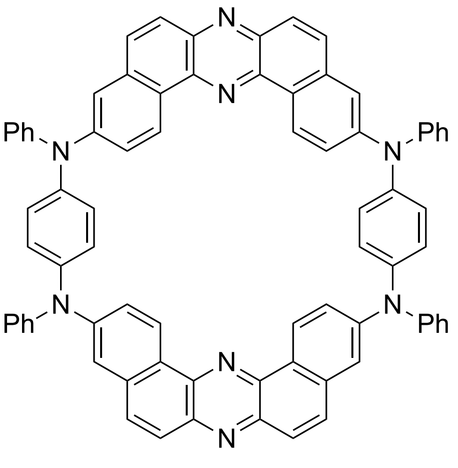

Dehydrated 1,4-dioxane was degassed through freeze-pump-thaw cycling for three times before use. A two necked reaction tube (10 mL) equipped with a magnetic stir bar, a rubber septum, and a glass stopper was flame-dried under reduced pressure and then purged with $N_2$ gas for three times. $Pd_2(dba)_3$ (4.5 mg, 4.9 µmol, 4.9 mol%), QPhos (14.3 mg, 20 µmol, 20 mol%), and 1,4-dioxane (1 mL) were added to the tube under a stream of $N_2$ gas. After the mixture was stirred at 60 °C for 1 h, DBPHZ-Br$_2$ **1** (43.9 mg, 0.10 mmol), **3** (79.7 mg, 0.10 mmol, 1.0 equiv), $K_2CO_3$ (30.4 mg, 0.22 mmol, 2.2 equiv), and 1,4-dioxane (1 mL) were added to the mixture under a stream of $N_2$ gas, and the mixture was stirred at 100 °C for 24 h. After the mixture was cooled to room temperature, de-ionized water (10 mL) was added to the mixture, which was then extracted with $CH_2Cl_2$ (20 mL × 3). The combined organic extracts were dried over $Na_2SO_4$, which was purified by flash column chromatography on NH silica gel (eluent: *n*-hexane/toluene 4:6–3:7). After dried in a vacuum oven at 200 °C for 1 h, ***p*-MC** was obtained as orange solid in 45% yield (48.8 mg, 45.5 μmol). mp 567.6 °C (dec.); $R_f$ 0.35 (*n*-hexane/EtOAc 6:4, NH silica).

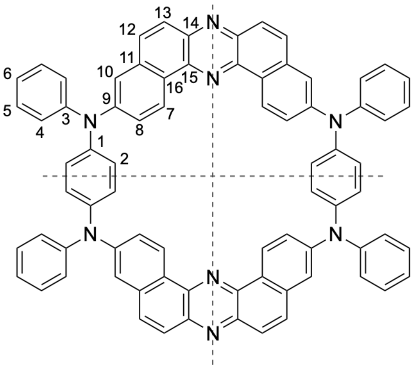

All the $^1$H and $^{13}$C signals were assigned as shown in the figure below based on the 2D $^1$H-$^1$H and $^1$H-$^{13}$C correlation NMR spectroscopy (see the Figures 4–6): δ 9.54 (d, $J$ = 9.0 Hz, 4H, H$^7$), 7.92 (d, $J$ = 9.0 Hz, 4H, H$^{13}$), 7.76 (d, $J$ = 9.0 Hz, 4H, H$^{12}$), 7.50 (d, $J$ = 2.4 Hz, 4H, H$^{10}$), 7.53 (dd, $J$ = 8.4, 2.4 Hz, 4H, H$^8$), 7.34 (t, $J$ = 7.8 Hz, 8H, H$^5$), 7.22 (d, $J$ = 7.2 Hz, 8H, H$^4$), 7.14 (t, $J$ = 7.2 Hz, 4H, H$^6$), 6.97 (s, 8H, H$^2$); $^{13}$C NMR (151 MHz, $CDCl_3$): δ 149.3 (C$^{10}$), 146.8 (C$^8$), 143.4 (C$^6$), 141.7 (C$^4$), 140.9 (C$^{16}$), 134.5 (C$^7$), 131.4 (C$^2$), 129.6 (C$^{13}$), 127.5 (C$^5$), 126.9 (C$^{12}$), 126.5 (C$^{11}$), 125.5 (C$^{15}$), 125.1 (C$^{14}$), 123.9 (C$^1$), 122.7 (C$^3$), 117.9 (C$^9$); IR (ATR, cm$^{-1}$): 3035, 3042, 1616, 1599, 1589, 1489, 1474, 1356, 1302, 1258, 1219, 1188, 1140, 1109, 997, 970, 860, 845, 789, 760, 746, 718, 704; MS (FAB$^+$): m/z (relative intensity, %): 1073 ([M+H]$^+$, 36), 1072 (M$^+$, 24), 91 ([$C_6H_5N$]$^+$, 32), 77 ([$C_6H_5$]$^+$, 22); HRMS (FAB$^+$): m/z calcd for $C_{76}H_{48}N_8$ (M) 1073.4002, found 1072.3998; Anal. Calcd for $C_{76}H_{48}N_8$: C, 4.51; H, 85.05; N, 10.44. found: C, 4.63; H, 84.77; N, 10.26.

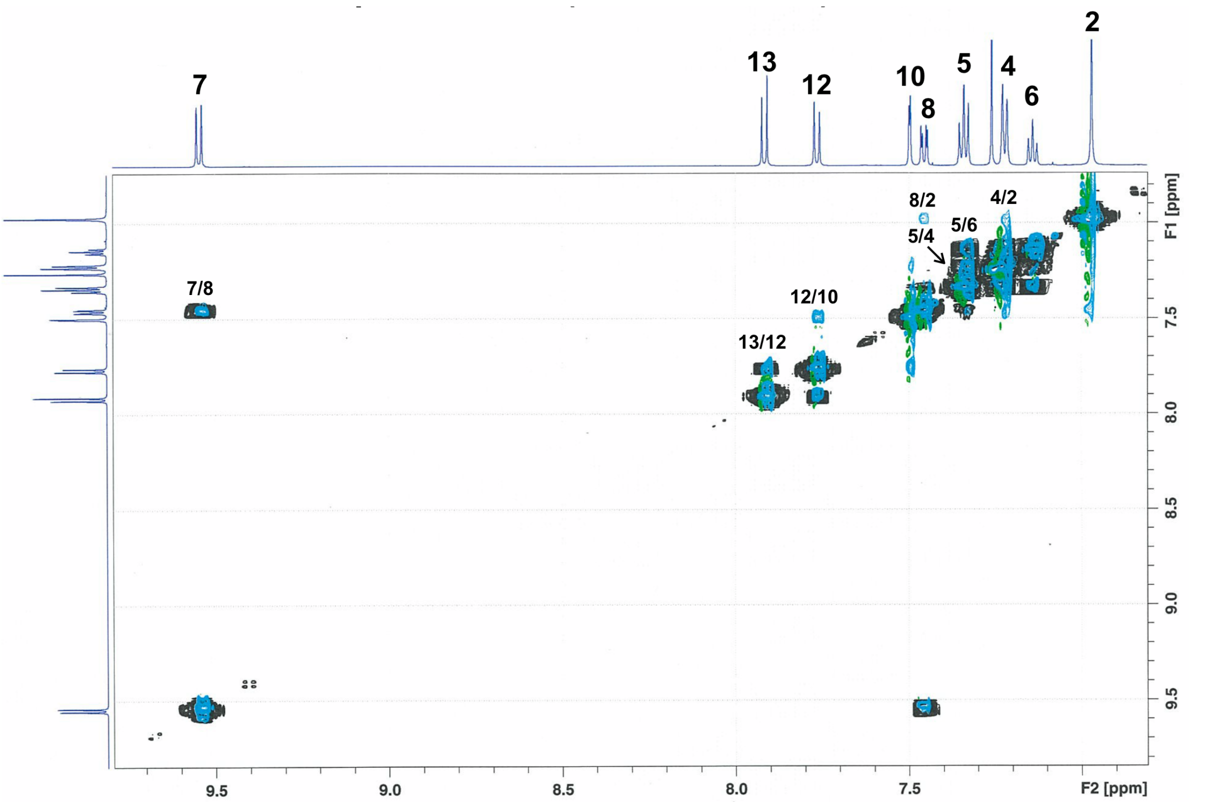

**Figure 4.** 2D $^{1}H$-$^{1}H$ COSY (black dots) and NOESY (blue-green dots) NMR spectra of ***p*-MC** (600 MHz, $CDCl_3$). Reproduced from ref. 10. Copyright 2020 American Chemical Society.

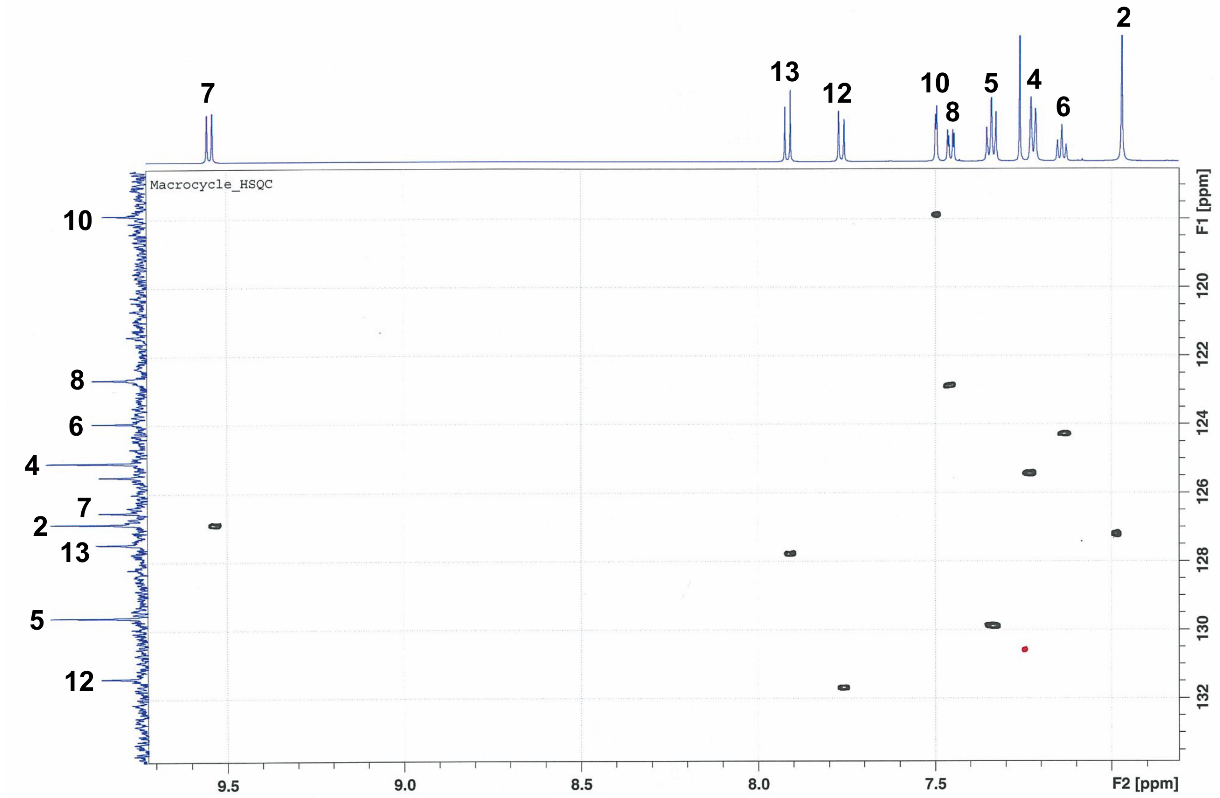

**Figure 5.** 2D $^{1}H$-$^{13}C$ HSQC NMR spectrum of ***p*-MC** (600 MHz, $CDCl_3$). Reproduced from ref. 10. Copyright 2020 American Chemical Society.

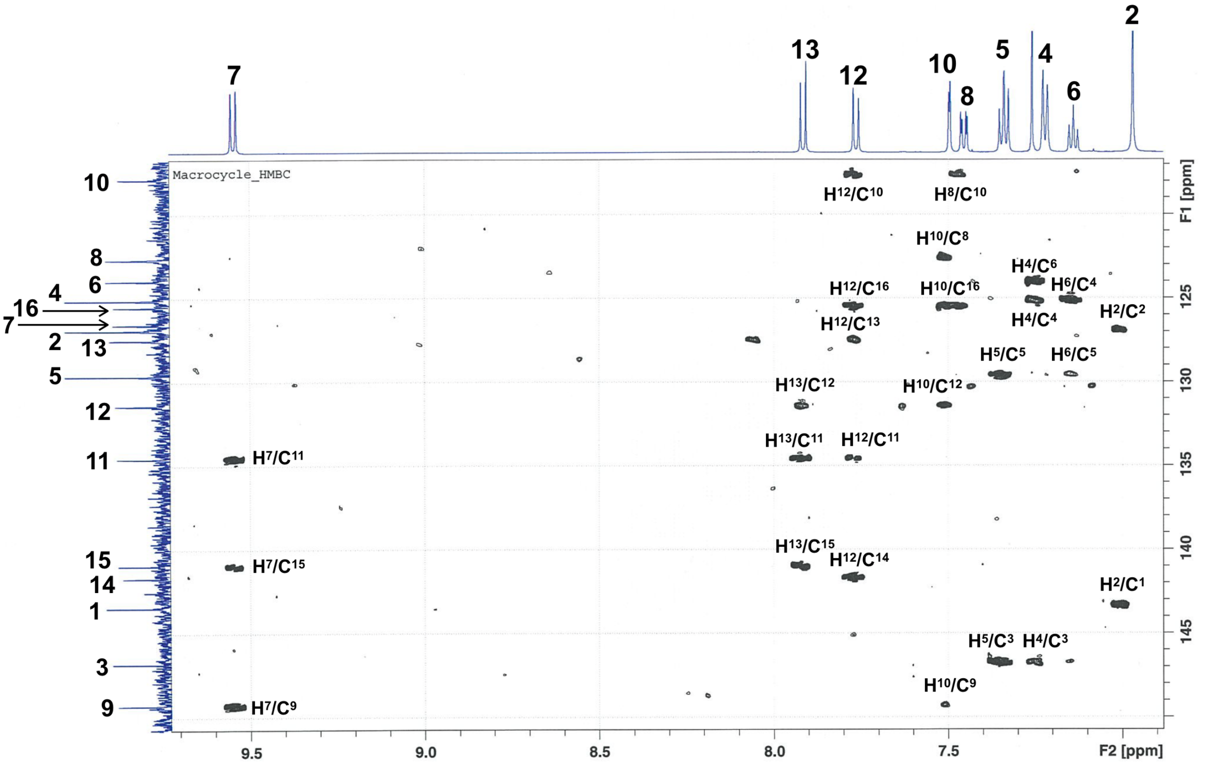

**Figure 6.** 2D $^{1}$H-$^{13}$C HMBC NMR spectrum of ***p*-MC** (600 MHz, $CDCl_3$). Reproduced from ref. 10. Copyright 2020 American Chemical Society.

### 4-((diphenylmethylene)amino)aniline (12) [1023292-39-8]

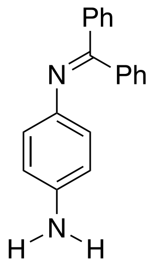

The title compound **12** was prepared according to a similar procedure for preparation of **10** with a slight modification. Montmorillonite K-10 was dried at 130 °C under reduced pressure for half a day. Three-necked round bottom flask (300 mL) equipped with a magnetic stir bar, glass stoppers and a Dean-Stark apparatus, was evacuated and refilled with $N_2$ gas for three times. *p*-phenylenediamine (5.42 g, 50 mmol), benzophenone (9.11g, 50 mmol, 1.0 equiv), montmorillonite K-10 (5.0 g), and toluene (180 mL) were added to the flask under a stream of $N_2$ gas at room temperature, and the resulting mixture was stirred for 24 h under reflux using an aluminium block heated at 160 ºC. The solvent was removed under reduced pressure, and the residue was purified by flash column chromatography on silica gel (eluent: *n*-hexane/EtOAc 9:1–7:3) to give product **12** as yellow solid in 58% yield (7.94 g, 29 mmol). Spectroscopic data were in good agreement with those previously reported:[11] $^{1}$H NMR (400 MHz, $CDCl_3$): δ 7.70 (d, $J$ = 7.4 Hz, 2H), 7.45–7.36 (m, 3H), 7.29–7.26 (m, 3H), 7.14–7.12 (m, 2H), 6.58 (d, $J$ = 8.4 Hz, 2H), 6.48 (d, $J$ = 8.4 Hz, 2H), 3.47 (brs, 2H); $^{13}$C NMR (100 MHz, $CDCl_3$): δ 166.9, 142.7, 142.4, 140.3, 136.9, 130.3, 129.6, 129.1, 128.3, 128.1, 128.0, 122.9, 115.2.

**4-(*tert*-butyl)-*N*-(4-((diphenylmethylene)amino)phenyl)aniline (13)**

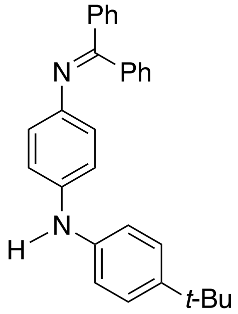

The title compound **13** was prepared according to a similar procedure for preparation of **9b** with a slight modification. In a glovebox, to a three-necked round bottom flask (100 mL) equipped with a magnetic stir bar and a rubber septum, was added *t*-BuXPhos (127.7 mg, 0.30 mmol, 2.9 mol%), and the flask was sealed with a rubber septum. To the flask, **12** (3.00 g, 11 mmol, 1.1 equiv), 1-bromo-4-*tert*-butylbenzene (2.18 g, 10 mmol), $Pd_2(dba)_3$ (91.5 mg, 0.10 mmol, 0.98 mol%), THF (20 mL), and *t*-BuOH (10 mL) were added. After the solution was degassed through the freeze-pump-thaw cycling for three times, $Cs_2CO_3$ (6.52 g, 20 mmol, 2.0 equiv) was added to the solution and it was stirred at 85 °C for 12 h. De-ionized water (20 mL) was added to the reaction mixture, and the organic layer was extracted with $CH_2Cl_2$ (30 mL × 3). The combined organic extracts were dried over $Na_2SO_4$, which was purified by flash column chromatography on NH silica gel (eluent: *n*-hexane/EtOAc 10:0–9:1) to give **13** as orange-yellow solid in 95% yield (3.91 g, 9.7 mmol). mp 161.3–162.1 °C; $R_f$ 0.30 (*n*-hexane/EtOAc 8:2, NH silica); $^1$H NMR (400 MHz, $CDCl_3$): δ 7.73 (d, *J* = 7.6 Hz, 2H), 7.47–7.34 (m, 3H), 7.31–7.24 (m, 5H), 7.16–7.14 (m, 2H), 6.92 (d, *J* = 8.4 Hz, 2H), 6.85 (d, *J* = 8.8 Hz, 2H), 6.66 (d, *J* = 6.0 Hz, 2H), 5.48 (brs, 1H), 1.29 (s, 9H); $^{13}$C NMR (100 MHz, $CDCl_3$): δ 167.4, 144.6, 143.5, 141.0, 140.1, 139.3, 136.7, 130.4, 129.6, 129.2, 128.5, 128.1, 128.0, 126.0, 122.7, 118.1, 117.2, 34.4, 31.4 ; IR (ATR, cm$^{-1}$): 3302, 2962, 1598, 1568, 1516, 1500, 1442, 1307, 1267, 1219, 1190, 1172, 1141, 1001, 960, 918, 825, 781, 765, 729, 700; MS (FAB$^+$, NBA): m/z (relative intensity, %): 405 ([M+H]$^+$, 90), 404 (M$^+$, 100), 389 ([M–$CH_3$]$^+$, 14), 77 ([$C_6H_5$]$^+$, 6), 57 ([*t*-Bu]$^+$, 3); HRMS (FAB$^+$, NBA): m/z calcd for $C_{29}H_{28}N_{24}$ (M) 404.2252, found 404.2246.

***tert*-butyl (4-(*tert*-butyl)phenyl)(4-((diphenylmethylene)amino)phenyl)carbamate (14)**

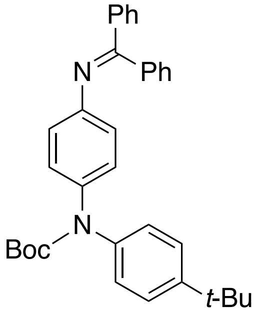

The title compound **14** was prepared according to a similar procedure for preparation of **11** with a slight modification. Three-necked round bottom flask (200 mL) equipped with a magnetic stir bar, was added **13** (3.63 g, 9.0 mmol) under the air. The flask was capped with glass stoppers and evacuated and refilled with $N_2$ gas for three times. THF (60 mL), di-*tert*-butyl dicarbonate (2.36 mg, 11 mmol, 1.2 equiv), and DMAP

(166.7 mg, 1.4 mmol, 15 mol%) were added to the flask under a stream of $N_2$ gas at room temperature, and the resulting mixture was stirred under 85 °C for 12 h. The solvent was removed under reduced pressure, and the residue was purified by flash column chromatography on silica gel (eluent: *n*-hexane/EtOAc 10:0–9:1) to give product **14** as pale-yellow solid in 92% yield (4.18 g, 8.3 mmol). mp 123.0–123.7 °C; $R_f$ 0.45 (*n*-hexane/EtOAc 8:2, NH silica); $^1$H NMR (400 MHz, $CDCl_3$): δ 7.74 (d, $J$ = 7.2 Hz, 2H), 7.47 (t, $J$ = 7.2 Hz, 1H), 7.40 (t, $J$ = 7.6 Hz, 2H), 7.29–7.24 (m, 5H), 7.13 (dd, $J$ = 8.0, 2.0 Hz, 2H), 7.07 (d, $J$ = 8.8 Hz, 2H), 6.98 (d, $J$ = 8.4 Hz, 2H), 6.67 (d, $J$ = 8.8 Hz, 2H), 1.39 (s, 9H), 1.29 (s, 9H); $^{13}$C NMR (100 MHz, $CDCl_3$): δ 168.6, 154.0, 149.0, 147.9, 140.3, 139.5, 138.4, 136.1, 130.8, 129.5, 129.3, 128.6, 128.2, 127.9, 127.5, 125.5, 125.4, 121.3, 80.7, 34.3, 31.3, 28.2; IR (ATR, cm$^{-1}$): 2966, 1705, 1620, 1597, 1573, 1514, 1498, 1446, 1365, 1330, 1317, 1294, 1220, 1174, 1161, 1145, 1109, 1055, 1014, 960, 856, 831, 800, 767, 748, 715; MS (FAB$^+$, NBA): m/z (relative intensity, %): 505 ([M+H]$^+$, 88), 504 (M$^+$, 56), 448 ([M+H–*t*-Bu]$^+$, 100), 447 ([M–*t*-Bu]$^+$, 6), 404 ([M+H–Boc]$^+$, 37), 403 ([M–Boc]$^+$, 42), 108 ([$C_{13}H_{10}N$]$^+$, 10), 77 ([Ph]$^+$, 6), 57 ([*t*-Bu]$^+$, 41); HRMS (FAB$^+$, NBA): m/z calcd for $C_{34}H_{36}N_2O_2$ (M) 504.2777, found 504.2781.

### ***tert*-butyl (4-aminophenyl)(4-(*tert*-butyl)phenyl)carbamate (15)**

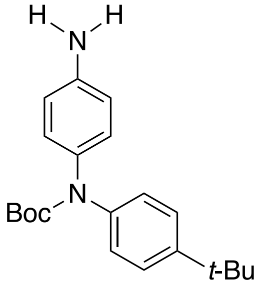

The title compound **15** was prepared according to a similar procedure for preparation of **8b** with a slight modification. Three-necked round bottom flask (200 mL) equipped with a magnetic stir bar, was added **14** (3.52 g, 7.0 mmol) under the air. The flask was capped with glass stoppers and evacuated and refilled with $N_2$ gas for three times. To the flask, ammonium formate (5.29 g, 84 mmol, 12 equiv), 10% Pd/C (1.12 g, 1.0 mmol based on Pd, 15 mol% based on Pd), THF (20 mL) and MeOH (30 mL) were added under a stream of $N_2$ gas at room temperature, and the resulting mixture was stirred at 85 °C for 3 h. The solution was filtered through a Celite pad, and the solvent was removed under reduced pressure to give solid residue. The solid was washed by *n*-hexane and filtered to give product **15** as white solid in 87% yield (2.08 g, 6.1 mmol). mp 131.7–132.5 °C; $R_f$ 0.18 (*n*-hexane/EtOAc 6:4, NH silica); $^1$H NMR (400 MHz, $CDCl_3$): δ 7.28–7.25 (m, 2H), 7.13 (d, $J$ = 8.8 Hz, 2H), 6.99 (d, $J$ = 8.8 Hz, 2H), 6.62 (d, $J$ = 8.8 Hz, 2H), 3.64 (brs, 2H), 1.44 (s, 9H), 1.28 (s, 9H); $^{13}$C NMR (100 MHz, $CDCl_3$): δ 154.4, 147.7, 144.3, 140.7, 134.3, 128.5, 125.5, 125.4, 115.2, 80.6, 34.3, 31.3, 28.3; IR (ATR, cm$^{-1}$): 3433, 3360, 2966, 1691, 1631, 1606, 1514, 1390, 1367, 1344, 1294, 1257, 1224, 1159, 1112, 1055, 854, 831, 819, 800, 767, 732; MS (FAB$^+$, NBA): m/z (relative intensity, %): 341 ([M+H]$^+$, 23), 340 (M$^+$, 54), 284 ([M+H–*t*-Bu]$^+$, 100), 283 ([M–*t*-Bu]$^+$, 6), 240 ([M+H–Boc]$^+$, 30), 239 ([M–Boc]$^+$, 38), 77 ([Ph]$^+$, 4), 57 ([*t*-Bu]$^+$, 47); HRMS (FAB$^+$, NBA): m/z calcd for $C_{21}H_{28}N_2O_2$ (M) 340.2151, found 340.2155.

**_tert_-butyl (4-(_tert_-butyl)phenyl)(4-((4-(_tert_-butyl)phenyl)amino)phenyl)carbamate (16)**

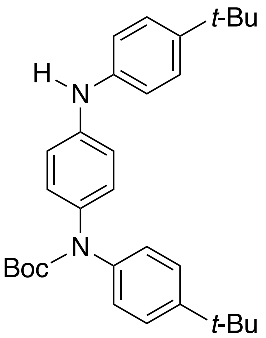

The title compound **16** was prepared according to a similar procedure for preparation of **9b** with a slight modification. In a glovebox, to a three-necked round bottom flask (200 mL) equipped with a magnetic stir bar and a rubber septum, was added *t*-BuXPhos (63.4 mg, 0.15 mmol, 2.8 mol%), and the flask was sealed with a rubber septum. To the flask, **15** (2.07 g, 6.1 mmol, 1.1 equiv), 1-bromo-4-*tert*-butylbenzene (1.13 g, 5.3 mmol), $Pd_2(dba)_3$ (46.0 mg, 0.05 mmol, 0.9 mol%), THF (10 mL) and *t*-BuOH (5 mL) were added. After the solution was degassed through the freeze-pump-thaw cycling for three times, $Cs_2CO_3$ (3.26 g, 10 mmol, 1.9 equiv) was added to the solution, and the resulting mixture was stirred at 85 °C for 24 h. De-ionized water (20 mL) was added to the reaction mixture, and the organic layer was extracted with $CH_2Cl_2$ (30 mL × 3). The combined organic extracts were dried over $Na_2SO_4$, which was purified by flash column chromatography on NH silica gel (eluent: *n*-hexane/EtOAc 10:0–8:2) to give **16** as white solid in 95% yield (2.38 g, 5.0 mmol). mp 73.0–74.0 ºC; $R_f$ 0.35 (*n*-hexane/EtOAc 8:2, NH silica); $^1$H NMR (400 MHz, $CDCl_3$): δ 7.32–7.26 (m, 4H), 7.15 (d, *J* = 8.8 Hz, 2H), 7.08 (d, *J* = 8.8 Hz, 2H), 7.01 (d, *J* = 8.0 Hz, 2H), 6.97 (d, *J* = 8.0 Hz, 2H), 5.62 (brs, 1H), 1.45 (s, 9H), 1.30 (s, 9H), 1.29 (s, 9H); $^{13}$C NMR (100 MHz, $CDCl_3$): δ 154.3, 148.0, 144.2, 141.4, 140.5, 140.2, 135.7, 128.2, 126.1, 125.8, 125.5, 118.0, 117.2, 80.8, 34.4, 34.1, 31.4, 31.3, 28.3; IR (ATR, cm$^{-1}$): 3342, 2960, 1705, 1681, 1604, 1512, 1392, 1365, 1328, 1313, 1294, 1269, 1159, 1109, 1055, 1012, 958, 852, 823, 767, 752, 727; MS (FAB$^+$, NBA): m/z (relative intensity, %): 473 ([M+H]$^+$, 29), 472 (M$^+$, 71), 416 ([M+H–*t*-Bu]$^+$, 100), 415 ([M–*t*-Bu]$^+$, 11), 372 ([M+H–Boc]$^+$, 29), 371 ([M–Boc]$^+$, 45), 57 ([*t*-Bu]$^+$, 29); HRMS (FAB$^+$, NBA): m/z calcd for $C_{31}H_{40}N_2O_2$ (M) 472.3039, found 472.3093.

### di-*tert*-butyl ((dibenzo[*a*,*j*]phenazine-3,11-diylbis((4-(*tert*-butyl)phenyl)azanediyl))bis(4,1-phenylene))bis((4-(*tert*-butyl)phenyl)carbamate) (17)

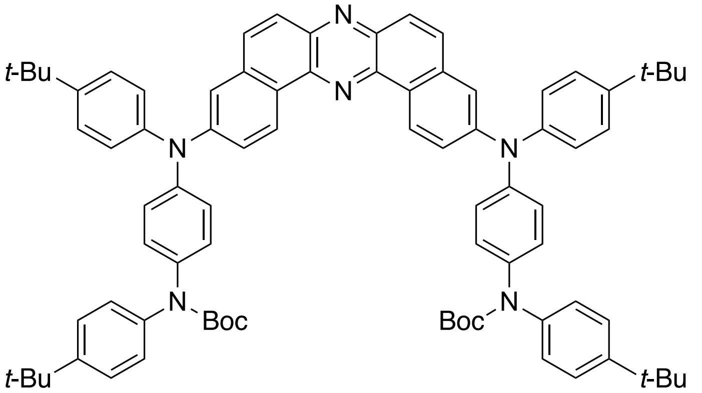

The intermediate **17** was prepared according to a similar method for preparation of **6b**. Toluene was degassed through freeze-pump-thaw cycling for three times before used. In a glovebox, to a two-necked reaction tube (10 mL) equipped with a magnetic stir bar, NaO*t*-Bu (84.6 mg, 0.88 mmol, 2.2 equiv) was added, and the tube was sealed with a rubber septum. Outside the glovebox, DBPHZ-Br$_2$ **1** (175.2 mg, 0.40 mmol), donor **16** (415.9 mg, 0.88 mmol, 2.2 equiv), Pd$_2$(dba)$_3$ (3.7 mg, 4.0 μmol, 1.0 mol%), QPhos (11.3 mg, 16 μmol, 4.0 mol%), and toluene (3 mL) were added under a stream of N$_2$ gas at room temperature, and the resulting mixture was stirred at 60 °C for 12 h. De-ionized water (5 mL) was added to the reaction mixture, and the organic layer was extracted with CH$_2$Cl$_2$ (20 mL × 3). The combined organic extracts were dried over Na$_2$SO$_4$, which was purified by column chromatography on NH silica gel (eluent: *n*-hexane/EtOAc 95:5–9:1) to give **17** as orange solid in 89% yield (364.1 mg, 0.36 mmol). mp 151.9–152.8 °C; $R_f$ 0.33 (*n*-hexane/EtOAc 7:3, NH silica); $^1$H NMR (400 MHz, CDCl3): δ 9.33 (d, *J* = 8.8 Hz, 2H), 7.93 (d, *J* = 9.2 Hz, 2H), 7.79 (d, *J* = 9.2 Hz, 2H), 7.54 (dd, *J* = 8.8, 2.4 Hz, 2H), 7.50 (d, *J* = 2.0 Hz, 2H), 7.36–7.32 (m, 8H), 7.20–7.13 (m, 16H), 1.35 (s, 18H), 1.32 (s, 18H); $^{13}$C NMR (100 MHz, CDCl$_3$): δ 154.2, 148.9, 148.5, 147.0, 144.8, 144.4, 141.7, 140.9, 140.2, 138.5, 134.6, 131.5, 127.9, 127.4, 126.4, 126.3, 126.1, 125.7, 125.6, 124.9, 124.8, 123.0, 119.2, 81.1, 34.5, 34.4, 31.43, 31.37, 28.3; IR (ATR, cm$^{-1}$): 2972, 1705, 1614, 1591, 1504, 1489, 1473, 1354, 1336, 1301, 1274, 1255, 1157, 1053, 1024, 997, 974, 954, 875, 848, 794, 748, 723; MS (FAB$^+$, NBA): m/z (relative intensity, %): 1222 ([M+H]$^+$, 14), 1221 (M$^+$, 7), 1120 ([M+H–Boc]$^+$, 4), 1119 ([M–Boc]$^+$, 3), 57 ([*t*-Bu]$^+$, 100); HRMS (FAB$^+$, NBA): m/z calcd for $C_{82}H_{88}N_6O_4$ (M) 1220.6867, found 1220.6886.

**$N^1$,$N^{1'}$-(dibenzo[*a*,*j*]phenazine-3,11-diyl)bis($N^1$,$N^4$-bis(4-(*tert*-butyl)phenyl)benzene-1,4-diamine) (18)**

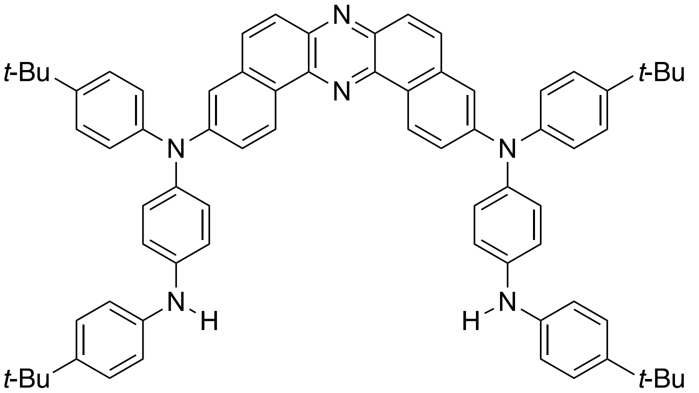

The intermediate **18** was prepared according to a similar method for preparation of **3**. To a two-necked tube (10 mL) equipped with a magnetic stir bar, were added **17** (256.4 mg, 0.21 mmol), dehydrated $CH_2Cl_2$ (3.0 mL), and TFA (1.2 mL, 16 mmol, 75 equiv). The resulting mixture was stirred at room temperature for 30 min. Saturated aqueous $NaHCO_3$ solution was added to the reaction mixture, and the organic layer was extracted with $CH_2Cl_2$ (10 mL × 3). The combined organic extracts were dried over $Na_2SO_4$, which was purified by column chromatography on NH silica gel (eluent: *n*-hexane/EtOAc 7:3) to give **18** quantitatively as red solid (213.5 mg, 0.21 mmol). mp 208.4–209.4 °C; $R_f$ 0.30 (*n*-hexane/EtOAc 7:3, NH silica); $^1$H NMR (400 MHz, $CDCl_3$): δ 9.31 (d, $J$ = 8.8 Hz, 2H), 7.91 (d, $J$ = 9.6 Hz, 2H), 7.78 (d, $J$ = 9.6 Hz, 2H), 7.52 (dd, $J$ = 8.8, 1.8 Hz, 2H), 7.43 (d, $J$ = 2.0 Hz, 2H), 7.34–7.30 (m, 8H), 7.17–7.14 (m, 8H), 7.07–7.04 (m, 8H), 5.66 (s, 2H), 1.35 (s, 18H), 1.32 (s, 18H); $^{13}$C NMR (100 MHz, $CDCl_3$): δ 149.4, 146.4, 144.6, 144.1, 141.5, 141.0, 140.5, 140.4, 140.2, 134.7, 131.5, 127.4, 127.2, 126.3, 126.2, 126.0, 124.9, 124.1, 121.9, 118.5, 117.9, 117.6, 34.4, 34.2, 31.5 (one signal corresponding to the Me group was not detected from the NMR chart, due to the overlap with the signal at 31.5 ppm); IR (ATR, cm$^{-1}$): 3394, 2962, 1604, 1508, 1473, 1390, 1357, 1315, 1288, 1265, 1238, 1190, 1184, 1143, 1107, 999, 871, 848, 827, 792, 731, 719; MS (FAB$^+$, NBA): m/z (relative intensity, %): 1022 ($[M+H]^+$, 100), 1021 ($M^+$, 78), 1007 ($[M+H–CH_3]^+$, 24), 1006 ($[M–CH_3]^+$, 28), 966 ([M+H–*t*-Bu]$^+$, 11), 965 ([M–*t*-Bu]$^+$, 11), 57 ([*t*-Bu]$^+$, 26); HRMS (FAB$^+$, NBA): m/z calcd for $C_{72}H_{72}N_6$ (M) 1020.5818, found 1020.5822.

**2,4,6,8-tetrakis(4-(*tert*-butyl)phenyl)-2,4,6,8-tetraaza-1,5(3,11)-didibenzo[*a*,*j*]phenazina-3,7(1,4)-dibenzenacyclooctaphane**

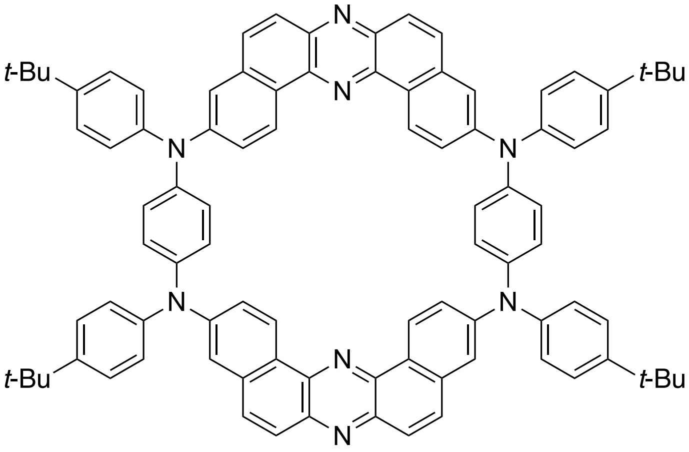

***t*-Bu-MC** was prepared according to a similar method for preparation of ***p*-MC**. Dehydrated 1,4-dioxane was degassed through freeze-pump-thaw cycling for three times before use. A two necked reaction tube (10 mL) equipped with a magnetic stir bar, a rubber septum, and a glass stopper was flame-dried under reduced pressure and then purged with $N_2$ gas for three times. $Pd_2(dba)_3$ (4.5 mg, 4.9 μmol, 4.9 mol%), QPhos (14.1 mg, 20 μmol, 20 mol%), and 1,4-dioxane (1 mL) were added to the tube under a stream of $N_2$ gas. After the mixture was stirred at 60 °C for 1 h, DBPHZ-$Br_2$ **1** (43.8 mg, 0.10 mmol), **18** (102.0 mg, 0.10 mmol, 1.0 equiv), $K_2CO_3$ (30.4 mg, 0.22 mmol, 2.2 equiv), and 1,4-dioxane (1 mL) were added to the mixture under a stream of $N_2$ gas, and the mixture was stirred at 100 °C for 24 h. After the mixture was cooled to room temperature, de-ionized water (10 mL) was added to the mixture, which was then extracted with $CH_2Cl_2$ (20 mL × 3). The combined organic extracts were dried over $Na_2SO_4$, which was purified by column chromatography on NH silica gel (eluent: *n*-hexane/toluene 6:4–4:6). After dried in a vacuum oven at 240 °C for 1 h, macrocycle ***t*-Bu-MC** was obtained as orange solid in 30% yield (39.0 mg, 30 μmol). mp >400 °C; $R_f$ 0.28 (*n*-hexane/EtOAc 8:2, NH silica); $^1$H NMR (400 MHz, $CDCl_3$): δ 9.52 (d, $J$ = 9.2 Hz, 4H), 7.92 (d, $J$ = 8.8 Hz, 4H), 7.80 (d, $J$ = 9.6 Hz, 4H), 7.52 (br, 8H), 7.37 (d, $J$ = 8.4 Hz, 8H), 7.29–7.22 (m, 8H), 7.10 (s, 8H), 1.38 (s, 36H); $^{13}$C NMR (151 MHz, $CDCl_3$): δ 149.5, 147.0, 144.0, 143.4, 141.6, 141.0, 134.6, 131.4, 127.3, 126.8, 126.44, 126.41, 125.2, 124.8, 122.2, 117.4, 34.5, 31.5; IR (ATR, cm$^{-1}$): 3035, 2960, 1598, 1544, 1504, 1475, 1355, 1317, 1305, 1261, 1219, 1176, 1141, 1111, 1016, 999, 972, 864, 823, 792, 748, 719; MS (FAB$^+$, NBA): m/z (relative intensity, %): 1297 ([M+H]$^+$, 2), 1296 (M$^+$, 1); HRMS (FAB$^+$, NBA): m/z calcd for $C_{92}H_{80}N_8$ (M) 1296.6506, found 1296.6501

### 3-bromo-*N*-phenylaniline (19) [88280-58-4]

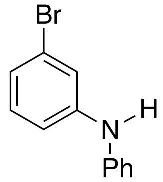

The title compound **19** was prepared according to a similar method reported in the literature[12] with a slight modification. Dehydrated toluene was degassed through freeze-pump-thaw cycling for three times before use. A two-necked flask (100 mL) equipped with a magnetic stir bar, a rubber septum, and a three-way stopcock was transferred into a glove box, and NaO*t*-Bu (2.70 g, 28 mmol, 1.4 equiv) was added to the flask. The flask was removed from the glove box, and to the flask, were added 1-bromo-3-iodobenzene (5.64 g, 20 mmol), aniline (1.95 g, 21 mmol, 1.05 equiv), and toluene (16 mL) under a stream of $N_2$ gas (*solution A*). A two-necked tube (5 mL) equipped with a magnetic stir bar, a rubber septum, and a glass stopper was flame-dried under reduced pressure and then purged with $N_2$ gas for three times. To the tube, were added $Pd(OAc)_2$ (22.4 mg, 0.10 mmol, 0.5 mol%), DPEPhos (81.0 mg, 0.15 mmol, 0.75 mol%), and toluene (2 mL) under a stream of $N_2$ gas, and the mixture was stirred at room temperature for an 1 h. The resulting solution was added to the *solution A* through the septum via cannula, and the rubber septum was replaced with a glass stopper, and then the mixture was stirred at 110 °C for 2 h. After the reaction mixture was allowed to cool to room temperature, de-ionized water (10 mL) was added to the reaction mixture, and the organic layer was extracted with EtOAc (20 mL × 3). The combined organic extracts were dried over $Na_2SO_4$, and the solvents were removed under reduced pressure to give the crude product as black oil, which was purified by flash column chromatography on NH silica gel (eluent: *n*-hexane/EtOAc 100:0–98:2). The obtained oil was distilled with a Kugelrohr distillation apparatus under reduced pressure, and the solid residue suspended in the purified oil was removed through filtration to give product **19** as colorless oil in 72% yield (3.58 g, 14 mmol). $^1$H NMR (400 MHz, $CDCl_3$): δ 7.32–7.27 (m, 2H), 7.19 (dd, *J* = 2.0, 2.0 Hz, 1H), 7.11–7.07 (m, 3H), 7.02–6.97 (m, 2H), 6.94 (ddd, J = 8.0, 2.0, 0.4 Hz, 1H), 5.69 (brs, 1H); $^{13}$C NMR (100 MHz, $CDCl_3$): δ 144.9, 141.9, 130.6, 129.4, 123.3, 123.1, 122.1, 119.5, 119.0, 115.5 These spectroscopic data were in good agreement with those previously repoted;[13] IR (ATR, cm$^{-1}$): 3396, 3034, 1584, 1494, 1472, 1448, 1402, 1310, 1275, 1236, 1164, 1067, 989, 901, 857, 748, 698, 677, 635.

### *tert*-butyl (3-bromophenyl)(phenyl)carbamate (20)

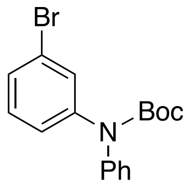

The title compound **20** was prepared according to a similar procedure for preparation of **11** with a slight modification. Three-necked round bottom flask (200 mL) equipped with a magnetic stir bar, a reflux condenser, and glass stoppers was evacuated and refilled with $N_2$ gas for three times. To the flask, were added **19** (5.55 g, 22 mmol), DMAP (407.3 mg, 3.3 mmol, 15 mol%), THF (88 mL), and di-*tert*-butyl 43henazine43e (5.22 g, 24 mmol, 1.1 equiv) under a stream of $N_2$ gas, and the resulting mixture was stirred under at 75 °C for 12 h. The solvent was removed under reduced pressure, and the residue was purified by flash column chromatography on silica gel (eluent: *n*-hexane/EtOAc 10:0–9:1) to give product **20** as colorless oil in 97% yield (7.50 g, 22 mmol). $R_f$ 0.48 (*n*-hexane/EtOAc 9:1, NH silica); $^1$H NMR (400 MHz, $CDCl_3$): δ 7.39 (dd, $J$ = 2.0, 2.0 Hz, 1H), 7.35–7.31 (m, 2H), 7.29 (ddd, $J$ = 6.8, 2.0, 2.0 Hz, 1H), 7.23–7.12 (m, 5H), 1.45 (s, 9H); $^{13}$C NMR (100 MHz, CDCl3): δ 153.4, 144.2, 142.3, 129.7, 129.6, 128.9, 128.4, 127.2, 126.1, 125.2, 121.9, 81.6, 28.1; IR (ATR, cm$^{-1}$): 3324, 2975, 1707, 1586, 1490, 1475, 1366, 1320, 1251, 1153, 1053, 848, 754, 700, 689; MS (EI$^+$): m/z (relative intensity, %): 349 ([M+2]$^+$, 10), 347 (M$^+$, 10), 293 ([M+2+H–*t*-Bu]$^+$, 21), 291 ([M+H–*t*-Bu]$^+$, 21), 249 ([M+2+H–Boc]$^+$, 95), 247 ([M+H–Boc]$^+$, 100), 167 ([$C_{12}H_9N$]$^+$, 50), 77 ([Ph]$^+$, 6), 57 ([*t*-Bu]$^+$, 70); HRMS (EI$^+$): m/z calcd for $C_{17}H_{18}BrNO_2$ (M) 347.0521, found 347.0517.

### *tert*-butylphenyl(3-(phenylamino)phenyl)carbamate (21)

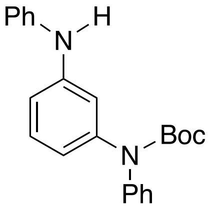

Dehydrated toluene was degassed through freeze-pump-thaw cycling for three times before use. A three-necked round bottom flask (100 mL) equipped with a magnetic stir bar, a rubber septum, and a glass stopper was transferred into a glove box. To the flask, were added NaO*t*-Bu (2.18 g, 23 mmol, 1.1 equiv) and Pd[P(*t*-Bu)$_3$]$_2$ (188.9 mg, 0.37 mmol, 1.7 mol%). The flask was removed from the glove box, and to the flask, were added **20** (7.50 g, 22 mmol), aniline (2.21 g, 24 mmol, 1.1 equiv), and toluene (22 mL) under a stream of $N_2$ gas. The resulting mixture was stirred at 80 °C for 12 h. After the reaction mixture was allowed to cool to room temperature, de-ionized water (20 mL) was added to the reaction mixture, and the organic layer was extracted with EtOAc (20 mL × 3). The combined organic extracts were dried over $Na_2SO_4$, and the solvents were removed under reduced pressure to give the crude product as brown solid, which was purified by flash column chromatography on NH silica gel (eluent: *n*-hexane/EtOAc 10:0–9:1). The obtained solid was recrystallized (EtOAc/*n*-hexane) to give product **21** as colorless solid in 84% yield (6.49 g, 18 mmol). Mp 96.8–97.5 °C; $R_f$ 0.38 (*n*-hexane/EtOAc 8:2); $^1$H NMR (400 MHz, $CDCl_3$): δ 7.33–7.29 (m, 2H), 7.25–7.15 (m, 6H), 7.02 (dd, *J* = 8.8, 0.8 Hz, 2H), 6.93–6.88 (m, 3H), 6.76 (ddd, *J* = 8.0, 1.6, 0.8 Hz, 1H), 5.69 (brs, 1H), 1.45 (s, 9H); $^{13}$C NMR (100 MHz, $CDCl_3$): δ 153.7, 143.9, 143.4, 142.9, 142.6, 129.3, 129.2, 128.6, 126.9, 125.6, 121.1, 119.4, 117.8, 116.3, 114.6, 81.1, 28.2; IR (ATR, cm$^{-1}$): 3339, 1682, 1587, 1536, 1496, 1483, 1367, 1341, 1265, 1254, 1159, 1061, 999, 856, 750, 741, 692; MS (EI$^+$): m/z (relative intensity, %): 360 (M$^+$, 14), 304 ([M+H –*t*-Bu]$^+$, 21), 260 ([M+H –Boc]$^+$, 100), 259 ([M–Boc]$^+$, 10), 167 ([$C_{12}H_9N$]$^+$, 24), 57 ([*t*-Bu]$^+$, 11); HRMS (EI$^+$): m/z calcd for $C_{23}H_{24}N_2O_2$ (M) 360.1838, found 360. 1835.

**di-*tert*-butyl ((dibenzo[*a,j*]phenazine-3,11-diylbis(phenylazanediyl))bis(3,1-phenylene)) bis(phenylcarbamate) (22)**

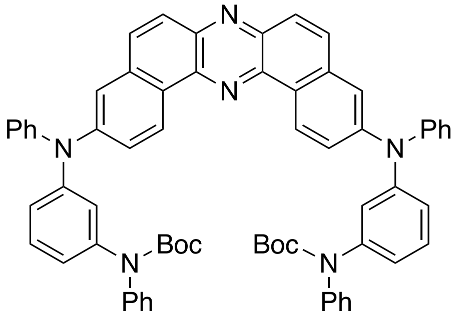

The intermediate **22** was prepared according to a similar method for preparation of **6b**. Dehydrated toluene was degassed through freeze-pump-thaw cycling for three times before used. A two-necked reaction tube (5 mL) equipped with a magnetic stir bar was transferred into a glove box. In the glove box, NaO*t*-Bu (84.6 mg, 0.88 mmol) was added to the tube, and the tube was sealed with a rubber septum and a glass stopper, and removed from the glove box. To the tube, DBPHZ-$Br_2$ **1** (175.2 mg, 0.40 mmol), donor **21** (302.5 mg, 0.84 mmol, 2.1 equiv), $Pd_2(dba)_3$ (3.7 mg, 4.0 μmol, 1.0 mol%), Qphos (11.4 mg, 16 μmol, 4.0 mol%), and toluene (3 mL) were added under a stream of $N_2$ gas at room temperature, and the resulting mixture was stirred at 60 °C for 12 h. De-ionize water (5 mL) was added to the reaction mixture, and the organic layer was extracted with $CHCl_3$ (20 mL × 3). The combined organic extracts were dried over $Na_2SO_4$, and the solvents were removed under reduced pressure to give the crude product as yellow-orange solid, which was purified by column chromatography on NH silica gel (eluent: *n*-hexane/EtOAc 95:5–8:2) to give **22** as yellow-orange solid in 93% yield (370.6 mg, 0.37 mmol). Mp 116.0–117.4 °C; $R_f$ 0.40 (*n*-hexane/EtOAc 7:3, NH silica); $^1$H NMR (400 MHz, $CDCl_3$): δ 9.33 (d, *J* = 8.8 Hz, 2H), 7.94 (d, *J* = 9.2 Hz, 2H), 7.76 (d, *J* = 9.2 Hz, 2H), 7.52 (dd, *J* = 8.8, 2.4 Hz, 2H), 7.48 (d, *J* = 2.4 Hz, 2H), 7.34–7.10 (m, 24H), 7.01 (ddd, *J* = 7.6, 2.4, 0.8 Hz, 2H), 6.96 (dd, *J* = 8.0, 2.4 Hz, 2H), 1.41 (s, 18H); $^{13}$C NMR (100 MHz, $CDCl_3$): δ 153.6, 148.5, 147.6, 146.9, 144.1, 142.8, 141.7, 140.7, 134.5, 131.5, 129.59, 129.54, 128.7, 127.3, 126.7, 126.1, 125.8, 125.6, 125.2, 124.0, 123.6, 123.2, 122.2, 122.0, 119.7, 81.2, 28.2; IR (ATR, $cm^{-1}$): 2973, 1706, 1588, 1485, 1475, 1352, 1294, 1252, 1155, 1055, 848, 764, 742, 720, 691; MS ($FAB^+$, NBA): m/z (relative intensity, %): 997 ($[M+H]^+$, 100), 996 ($M^+$, 79), 886 ($[M+4H–t\text{-}Bu\times2]^+$, 15), 885 ($[M+3H–t\text{-}Bu\times2]^+$, 21), 798 ($[M+4H–Boc\times2]^+$, 22), 797 ($[M+3H–Boc\times2]^+$, 45), 796 ($[M+2H–Boc\times2]^+$, 38), 795 ($[M+H–Boc\times2]^+$, 27), 167 ($[C_{12}H_9N]^+$, 25), 77 ($[Ph]^+$, 19), 57 ($[t\text{-}Bu]^+$, 84); HRMS ($FAB^+$, NBA): m/z calcd for $C_{66}H_{56}N_6O_4$ (M) 996.4363, found 996.4384.

**$N^1$,$N^{1'}$-(dibenzo[*a,j*]phenazine-3,11-diyl)bis($N^1$,$N^3$-diphenylbenzene-1,3-diamine) (23)**

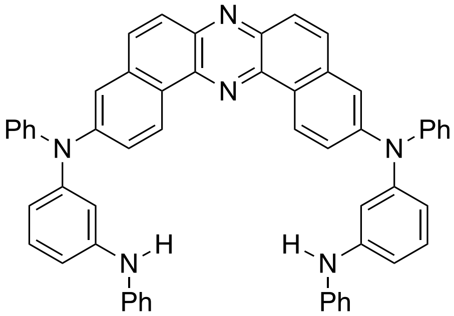

The intermediate **23** was prepared according to a similar method for preparation of **3**. To a round-bottomed flask (50 mL) equipped with a magnetic stir bar, were added **22** (295.8 mg, 0.30 mmol), dehydrated $CH_2Cl_2$ (5 mL), and TFA (1.2 mL, 16 mmol, 52 equiv). The resulting mixture was stirred at room temperature for 30 min. To the reaction mixture, saturated aqueous $NaHCO_3$ solution was added until the color of the solution turned from deep blue to orange, and the organic layer was extracted with $CH_2Cl_2$ (20 mL × 3). The combined organic extracts were dried over $Na_2SO_4$, the solvent was removed under reduced pressure to give the crude product as orange solid, which was purified by flash column chromatography on NH silica gel (eluent: *n*-hexane/EtOAc 7:3) to give **23** as red solid in 99% yield (237.8 mg, 0.30 mmol). Mp 120.5–122.6 ºC; $R_f$ 0.28 (*n*-hexane/EtOAc 7:3, NH silica); $^1H$ NMR (400 MHz, $CDCl_3$): δ 9.36 (d, $J$ = 8.8 Hz, 2H), 7.95 (d, $J$ = 9.2 Hz, 2H), 7.82 (d, $J$ = 9.2 Hz, 2H), 7.58 (dd, $J$ = 8.8, 2.0 Hz, 2H), 7.55 (d, $J$ = 2.0 Hz, 2H), 7.34 (dd, $J$ = 7.8, 7.8 Hz, 4H), 7.27–7.17 (m, 8H), 7.13 (t, $J$ = 7.2 Hz, 2H), 7.03 (d, $J$ = 7.2 Hz, 4H), 6.90 (dd, $J$ = 2.0, 2.0 Hz, 2H), 6.87 (d, $J$ = 7.2 Hz, 2H), 6.84 (dd, $J$ = 8.0, 2.4 Hz, 2H), 6.76 (dd, $J$ = 7.6, 2.4 Hz, 2H), 5.70 (brs, 2H); $^{13}C$ NMR (100 MHz, $CDCl_3$): δ 148.8, 148.4, 147.2, 144.1, 142.5, 141.7, 140.8, 134.5, 131.5, 130.2, 129.4, 129.2, 127.3, 126.1, 125.8, 125.2, 123.8, 123.4, 121.1, 119.8, 117.7, 117.3, 114.0, 112.6; IR (ATR, $cm^{-1}$): 3396, 3033, 1586, 1488, 1473, 1352, 1277, 1161, 1139, 993, 868, 849, 784, 744, 723, 691, 615; MS ($FAB^+$, NBA): m/z (relative intensity, %): 797 ($[M+H]^+$, 24), 796 ($M^+$, 21), 460 ($[M–C_{24}H_{20}N_2]^+$, 2), 89 ($[C_7H_5]^+$, 16), 77 ($[Ph]^+$, 14); HRMS ($FAB^+$, NBA): m/z calcd for $C_{56}H_{40}N_6$ (M) 796.3314, found 796.3317.

### **2,4,6,8-tetraphenyl-2,4,6,8-tetraaza-1,5(3,11)-didibenzo[*a*,*j*]phenazine-3,7(1,3)-dibenzenacyclooctaphane (*m*-MC)**

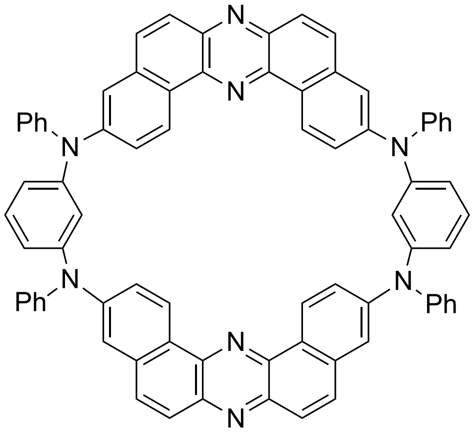

***m*-MC** was prepared according to a similar method for preparation of ***p*-MC**. Dehydrated 1,4-dioxane was degassed through freeze-pump-thaw cycling for three times before use. A two necked reaction tube (5 mL) equipped with a magnetic stir bar, a rubber septum, and a glass stopper was flame-dried under reduced pressure and then purged with $N_2$ gas for three times. To the tube, $Pd_2(dba)_3$ (9.2 mg, 10 μmol, 5 mol%), Qphos (28.2 mg, 40 μmol, 20 mol%), and 1,4-dioxane (0.5 mL) were added under a stream of $N_2$ gas. After the mixture was stirred at 60 °C for 1 h, DBPHZ-$Br_2$ **1** (87.7 mg, 0.20 mmol), **23** (159.3 mg, 0.20 mmol, 1.0 equiv), $K_2CO_3$ (60.7 mg, 0.44 mmol, 2.2 equiv), and 1,4-dioxane (0.5 mL) were added to the mixture under a stream of $N_2$ gas, and the mixture was stirred at 100 °C for 24 h. After the mixture was cooled to room temperature, de-ionized water (10 mL) was added to the mixture, which was then extracted with $CHCl_3$ (30 mL × 3). The combined organic extracts were dried over $Na_2SO_4$, the solvents were removed under reduced pressure to give the crude product as orange solid, which was purified by twice column chromatography on NH silica gel (eluent: *n*-hexane/toluene 5:5–10:0 for the first time, 6:4–10:0 for the second time). After dried in a vacuum oven at 240 °C for 1 h, ***m*-MC** was obtained as yellow-orange solid in 10% yield (21.2 mg, 20 μmol). Mp >400 ºC; $R_f$ 0.38 (toluene, NH silica); All the $^1$H and $^{13}$C signals were assigned as shown in the figure below based on the 2D $^1$H-$^1$H and $^1$H-$^{13}$C correlation NMR spectroscopy (see the Figures 10–13): $^1$H NMR (600 MHz, $CD_2Cl_2$): δ 9.45 (d, $J$ = 8.4 Hz, 4H, H$^9$), 7.76 (d, $J$ = 9.0 Hz, 4H, H$^{15}$), 7.66 (d, $J$ = 9.6 Hz, 4H, H$^{14}$), 7.62 (dd, $J$ = 9.0, 2.4 Hz, 4H, H$^{10}$), 7.39 (d, $J$ = 2.4 Hz, 4H, H$^{12}$), 7.37–7.34 (m, 10H, H$^1$&H$^7$), 7.29 (t, $J$ = 8.4 Hz, 2H, H$^4$), 7.26 (d, $J$ = 8.4 Hz, 8H, H$^6$), 7.16 (t, $J$ = 7.2 Hz, 4H, H$^8$), 6.86 (dd, $J$ = 8.4, 2.4 Hz, 4H, H$^3$); $^{13}$C NMR (151 MHz, $CD_2Cl_2$): δ 149.2 (C$^{11}$), 148.7 (C$^2$), 148.0 (C$^5$), 142.1 (C$^{16}$), 141.1 (C$^{17}$), 135.1 (C$^{13}$), 131.5 (C$^{14}$), 131.2 (C$^4$), 130.0 (C$^7$), 127.8 (C$^{15}$), 126.4 (C$^9$), 126.2 (C$^6$), 126.0 (C$^{18}$), 124.5 (C$^8$), 122.5 (C$^1$&C$^{10}$), 121.7 (C$^3$), 119.6 (C$^{12}$); IR (ATR, cm$^{-1}$): 3041,

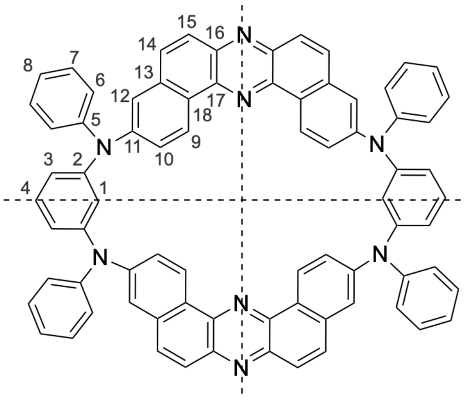

1613, 1577, 1541, 1475, 1347, 1287, 1254, 1149, 1137, 997, 873, 847, 789, 749, 717, 693, 648; MS (FAB$^+$, NBA): m/z (relative intensity, %): 1073 ([M+H]$^+$, 28), 1072 (M$^+$, 15), 91 ([$C_6H_5N$]$^+$, 64), 77 ([Ph]$^+$, 38); HRMS (FAB$^+$, NBA): m/z calcd for $C_{76}H_{49}N_8$ (M) 1073.4080, found 1073.4086.

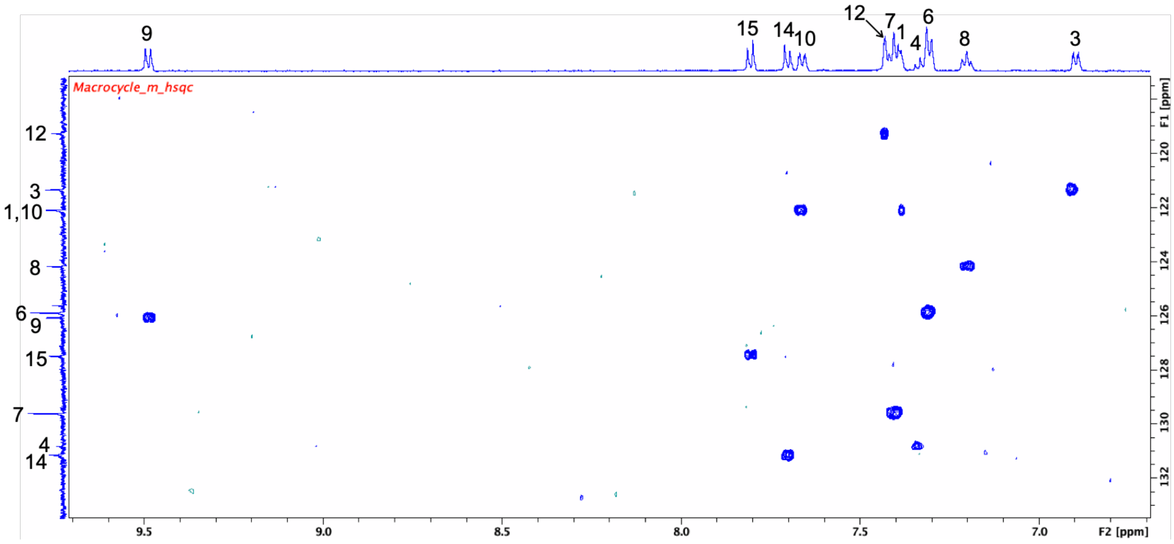

**Figure 7.** 2D $^1$H-$^{13}$C HSQC NMR spectrum of ***m*-MC** (600 MHz, $CD_2Cl_2$). Reproduced from ref. 14. Copyright 2020 Wiley-VCH Verlag GmbH.

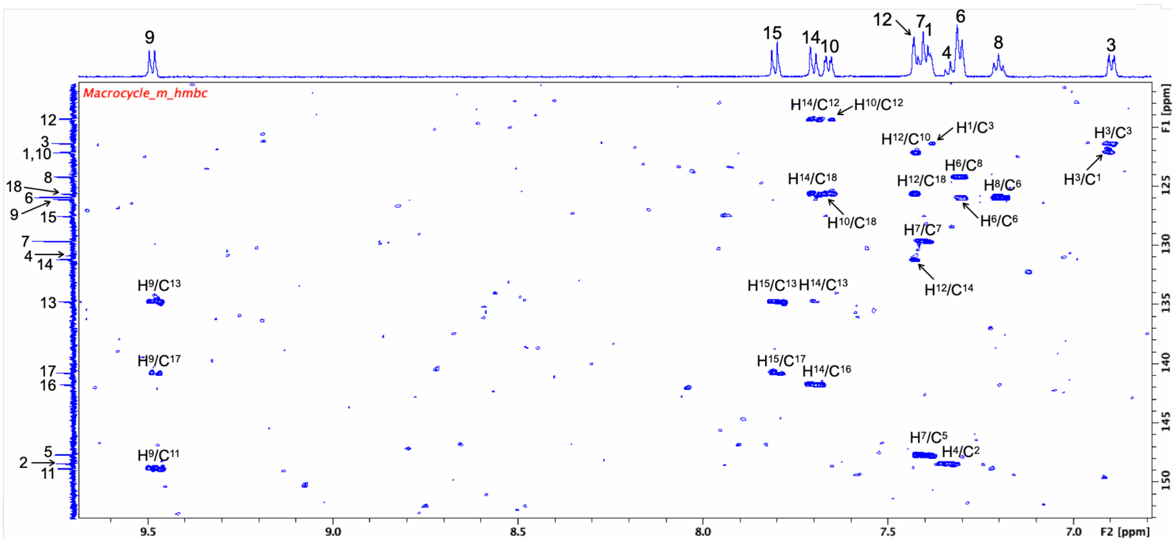

**Figure 8.** 2D $^1$H-$^{13}$C HMBC NMR spectrum of ***m*-MC** (600 MHz, $CD_2Cl_2$). Reproduced from ref. 14. Copyright 2020 Wiley-VCH Verlag GmbH.

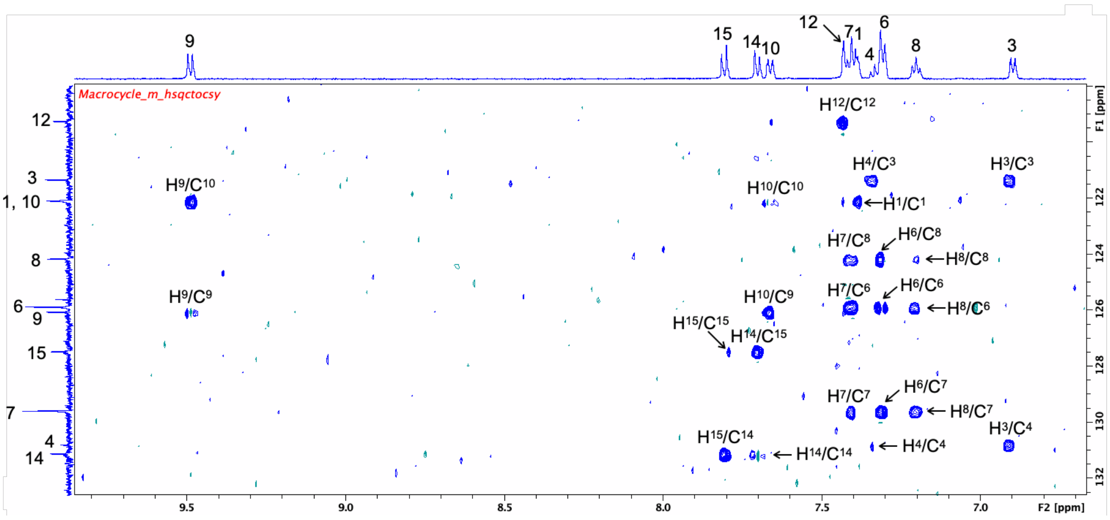

**Figure 9.** 2D $^1$H-$^{13}$C HSQC-TOCSY NMR spectrum of ***m*-MC** (600 MHz, $CD_2Cl_2$). Reproduced from ref. 14. Copyright 2020 Wiley-VCH Verlag GmbH.

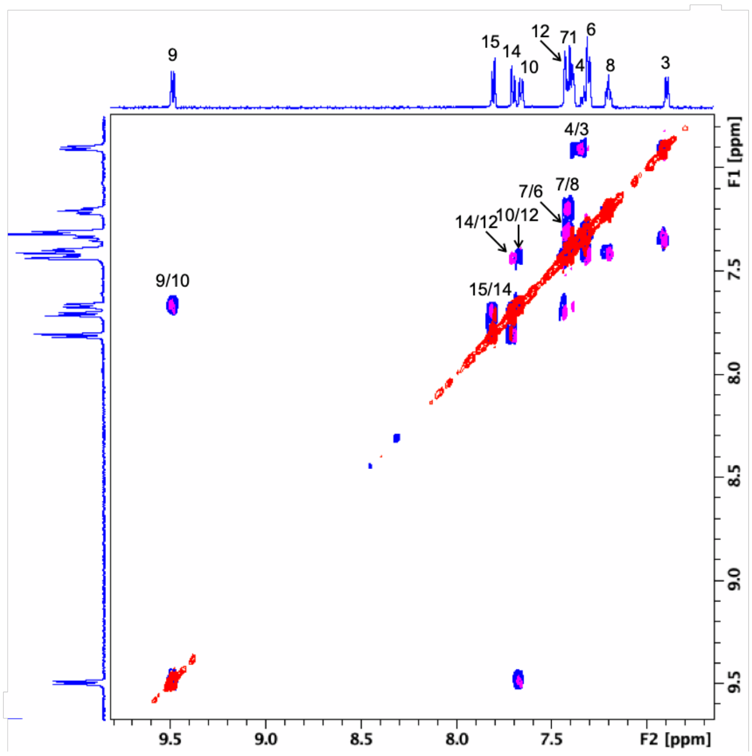

**Figure 10.** 2D $^1$H-$^1$H COSY (blue dots) and NOESY (red-pink dots) NMR spectra of ***m*-MC** (600 MHz, $CD_2Cl_2$). Reproduced from ref. 14. Copyright 2020 Wiley-VCH Verlag GmbH.

### *Tert*-butyl 1-(naphthalen-2-yl)hydrazine-1-carboxylate (24) [756822-60-3]

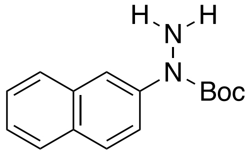

The title compound **24** was prepared according to a similar method reported in the literature[8] with a slight modification. Dehydrated toluene was degassed through freeze-pump-thaw cycling for three times before use. Three-necked round bottom flask (200 mL) equipped with a magnetic stir bar and reflux condenser, was capped with glass stoppers, and evacuated and refilled with $N_2$ gas for three times. To the vessel, were added 2-bromonaphthalene (14.15 g, 20 mmol), *tert*-butylcarbazate (7.93 g, 60 mmol, 3.0 equiv), $Pd_2(dba)_3$ (366.0 mg, 0.40 mmol, 2.0 mol%), XantPhos (695.1 mg, 1.2 mmol, 6.0 mol%), $Cs_2CO_3$ (9.77 g, 30 mmol. 1.5 equiv), and toluene (50 mL) under a stream of $N_2$ gas, and the mixture was stirred at 115 °C for 48 h. After the mixture was cooled to room temperature, de-ionized water (30 mL) was added to the reaction mixture, which was then extracted with EtOAc (50 mL × 3). The combined organic extracts were dried over $Na_2SO_4$, which was purified by flash column chromatography on silica gel (eluent: *n*-hexane/EtOAc 10:0–9:1). The recrystallization from a solution of EtOAc and *n*-hexane gave product **24** as beige solid in 57% yield (2.95 g, 11 mmol). Spectroscopic data were in agreement with those previously reported:[8] $^1H$ NMR (400 MHz, $CDCl_3$): δ 7.88 (d, $J$ = 1.6 Hz, 1H), 7.80–7.76 (m, 3H), 7.66 (dd, $J$ = 8.8, 2.0 Hz, 1H), 7.47–7.39 (m, 2H), 4.54 (brs, 2H), 1.52 (s, 9H); $^{13}C$ NMR (100 MHz, $CDCl_3$): δ 155.2, 140.6, 133.3, 130.8, 127.73, 127.66, 127.4, 126.1, 125.2, 123.1, 120.6, 81.9, 28.3.

### *tert*-butyl 1-(naphthalen-2-yl)-2-(6-(((trifluoromethyl)sulfonyl)oxy)-naphthalen-2-yl) hydrazine-1-carboxylate (25)

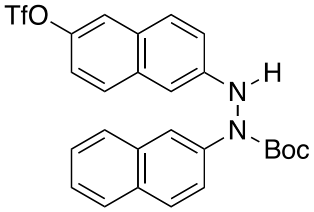

The title compound **25** was prepared according to a similar method reported in the literature[8] with a slight modification. Dehydrated toluene was degassed through freeze-pump-thaw cycling for three times before use. In glove box, to a three-necked round bottom flask (200 mL) equipped with a magnetic stir bar and a three-way stopcock, was added $Pd[P(t\text{-}Bu)_3]_2$ (256.1 mg, 0.50 mmol, 5.0 mol%), and the flask was sealed with glass stoppers. Outside the glovebox, the vessel was connected with a flame-dried reflux condenser, and the three-way stopcock was replaced with a glass stopper under a stream of $N_2$ gas. To the vessel, were added 6-bromo-2-naphthyltrifluoromethansulfonnate (3.55 g, 10 mmol, 1.0 equiv), **24** (2.59 g, 10 mmol), $Cs_2CO_3$ (4.89 g, 15 mmol, 1.5 equiv), and toluene (50 mL) under a stream of

$N_2$ gas, and the mixture was stirred at 115 °C for 5 h. After the mixture was cooled to room temperature, De-ionized water (20 mL) was added to the reaction mixture, and the organic layer was extracted with $CH_2Cl_2$ (20 mL × 3). The combined organic extracts were dried over $Na_2SO_4$, and the solvent was removed under reduced pressure to give the crude product. The crude product was purified by flash column chromatography on silica gel (eluent: *n*-hexane/EtOAc 10:1–8:2), and the obtained solid was then recrystallized from a $CHCl_3$ solution to give product **25** as white solid in 56% yield (2.99 g, 5.6 mmol). Mp 165.7–166.3 °C; $R_f$ 0.25 (*n*-hexane/EtOAc 8:2); $^1H$ NMR (400 MHz, $CDCl_3$): δ 8.01 (s, 1H), 7.83–7.76 (m, 5H), 7.69 (d, $J$ = 8.8 Hz, 1H), 7.65 (d, $J$ = 2.4 Hz, 1H), 7.48–7.40 (m, 2H), 7.28 (dd, $J$ = 9.2, 2.4 Hz, 1H), 7.21–7.18 (m, 2H), 6.74 (s, 1H), 1.41 (s, 9H); $^{13}C$ NMR (100 MHz, $CDCl_3$): δ 153.9, 147.0, 145.4, 140.0, 133.6, 133.5, 130.9, 129.4, 128.94, 128.86, 128.3, 127.8, 127.5, 126.4, 125.4, 121.2, 120.1, 119.1, 118.8 (q, $J_{C\text{–}F}$ = 319.4 Hz), 118.6, 117.2, 107.0, 82.9, 28.7; $^{19}F\{^1H, ^{13}C\}$ NMR (377 MHz, $CDCl_3$): δ –76.0 (s); IR (ATR, $cm^{-1}$): 3316, 3065, 2986, 2938, 1699, 1630, 1607, 1539, 1508, 1422, 1395, 1368, 1323, 1252, 1206, 1138, 1126, 1109, 966, 947, 935, 901, 889, 854, 826, 812, 795, 768, 750; MS ($FAB^+$): m/z (relative intensity, %): 533 ($[M+1]^+$, 22), 532 ($M^+$, 42), 477 ([M+2–*t*-Bu]$^+$, 33), 476 ([M+1–*t*-Bu]$^+$, 33), 432 ($[M+1\text{–}Boc]^+$, 45), 431 ($[M+1\text{–}Boc]^+$, 73), 291 ($[C_{11}H_8F_3NO_3S]^+$, 23), 290 ($[C_{11}H_7F_3NO_3S]^+$, 23), 158 ($[C_{10}H_{10}N_2]^+$, 36), 143 ($[C_{10}H_9N]^+$, 27), 142 ($[C_{10}H_8N]^+$, 22), 127 ($[C_{10}H_7]^+$, 13), 90 ($[C_6H_5N]^+$, 11), 89 ($[C_7H_5]^+$, 16), 77 ($[Ph]^+$, 15), 57 ([*t*-Bu]$^+$, 100); HRMS ($FAB^+$): m/z calcd for $C_{26}H_{23}F_3N_2O_5S$ (M) 532.1280, found 532.1288.

**2,2’-diamino-[1,1’-binaphthalen]-6-yl trifluoromethanesulfonate (26)**

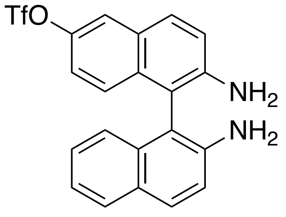

The title compound **26** was prepared according to a similar method reported in the literature[8] with a slight modification. A three-necked round bottom flask (100 mL) equipped with a magnetic stir bar and reflux condenser, was capped with glass stopper, and evacuated and refilled with $N_2$ gas for three times. To the vessel, were added **25** (1.07 g, 2.0 mmol), ethanol (30 mL), and conc. HCl (1.2 mL, 14 mmol, 7.0 equiv) under a stream of $N_2$ gas, and the mixture was stirred at room temperature until **25** was dissolved. The resulting mixture was stirred at 80 °C for 1.5 h. After the mixture was cooled to room temperature, the reaction mixture was neutralized by saturated aqueous $NaHCO_3$ solution, and the organic layer was extracted with $CH_2Cl_2$ (20 mL × 3). The combined organic extracts were dried over $Na_2SO_4$, and the solvent was removed under reduced pressure to give the crude product. The crude product was purified by flash column chromatography on NH silica gel (eluent: *n*-hexane/EtOAc 8:2–6:4) to obtain the title compound S6 with some impurities. To further purify, the obtained solid was dissolved into MeOH (10 mL), and conc. HCl (5 mL) was added to the solution which was then cooled to 0 °C. Precipitated solid was separated by filtration, and the solid was neutralized by 1 M NaOH aqueous solution, and which was extracted with $Et_2O$ (10 mL × 3). The combined organic extracts were dried over $Na_2SO_4$, and the solvent was removed under reduced pressure to give pure **26** as white solid in 64% yield (554.3 mg, 1.3 mmol). Mp 119.4–120.4 °C; $R_f$ 0.23 (*n*-hexane/EtOAc 6:4, NH silica); $^1$H NMR (400 MHz, $CDCl_3$): δ 7.84–7.80 (m, 3H), 7.68 (d, $J = 2.4$ Hz, 1H), 7.28–7.21 (m, 3H), 7.14 (t, $J = 8.8$ Hz, 2H), 7.06 (dd, $J = 9.2$, 2.4 Hz, 1H), 7.01 (dd, $J = 7.2$, 2.4 Hz, 1H), 3.83 (brs, 2H), 3.89 (brs, 2H); $^{13}$C NMR (100 MHz, $CDCl_3$): δ 144.9, 143.9, 142.7, 133.4, 133.0, 130.0, 129.4, 128.4, 128.3, 127.9, 127.1, 126.5, 123.5, 122.6, 120.2, 119.9, 119.5, 118.8 (q, $J_{C–F} = 319.5$ Hz), 118.2, 112.5, 111.3 (one of the splitting $CF_3$ signals was not recognized from the NMR chart, due to the overlap with a signal at 123.5 ppm); $^{19}$F{$^1$H, $^{13}$C} NMR (377 MHz, $CDCl_3$): δ –76.1 (s); IR (ATR, cm$^{-1}$): 3468, 3370, 3204, 3057, 1618, 1508, 1416, 1383, 1366, 1352, 1244, 1206, 1136, 1109, 941, 918, 880, 853, 814, 750; MS (EI$^+$): m/z (relative intensity, %): 433 ([M+1]$^+$, 11), 432 (M$^+$, 44), 300 ([M+1–$SO_2CF_3$]$^+$, 23), 299 ([M–$SO_2CF_3$]$^+$, 100); (EI$^+$): m/z calcd for $C_{21}H_{15}F_3N_2O_3S$ (M) 432.0755, found 432.0753.

**dibenzo[*a,j*]phenazine-3-yl trifluoromethanesulfonate (DBPHZ-OTf) (27)**

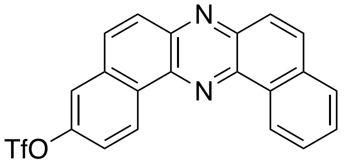

The title compound **27** was prepared according to a similar method reported in the literature[1] with a slight modification. To the vessel, were added **26** (260.8 mg, 0.60 mmol) and methanol (60 mL) under a stream of $N_2$ gas, and the mixture was stirred at room temperature until **26** was completely dissolved. Into the solution, 1,3-diiodo-5,5-dimethylhydantoin (1.83 g, 4.8 mmol, 8.0 equiv) was added under a stream of $N_2$ gas at room temperature. The resulting mixture was stirred at room temperature for 12 h before quenching with 2 M $Na_2S_2O_3$ aqueous solution (60 mL). The reaction mixture was extracted with $CH_2Cl_2$ (20 mL × 3), and the combined organic extracts were dried over $Na_2SO_4$. The solvent was removed under reduced pressure to give the crude product, which was purified by flash column chromatography on silica gel (eluent: *n*-hexane/EtOAc 95:5–8:2). Further purification was carried out through recrystallization from a $CHCl_3$ solution to give product **27** as yellow solid in 40% yield (101.7 mg, 0.24 mmol). Mp 173.8–174.6 °C; $R_f$ 0.23 (*n*-hexane/EtOAc 8:2); $^1$H NMR (400 MHz, $CDCl_3$): δ 9.69 (d, $J = 9.2$

Hz, 1H), 9.66 (d, *J* = 6.8 Hz, 1H), 8.19–7.98 (m, 5H), 7.90–7.81 (m, 3H), 7.72 (dd, *J* = 8.8, 2.4, Hz, 1H); $^{13}$C NMR (100 MHz, $CDCl_3$): δ 149.5, 143.1, 142.2, 140.6, 139.0, 133.9, 133.2, 133.0, 130.8, 130.7, 130.5, 129.6, 129.0, 128.1, 127.74, 127.70, 126.6, 125.0, 120.4, 118.8 (q, $J_{\mathrm{C-F}}$ = 319.4 Hz) (one of the splitting $CF_3$ signals was not recognized from the NMR chart, due to the overlap with a signal at 120.4 ppm); $^{19}$F{1H, 13C} NMR (377 MHz, $CDCl_3$): δ –75.3 (s); IR (ATR, cm$^{-1}$): 3063, 2976, 1614, 1516, 1476, 1418, 1358, 1250, 1211, 1138, 1119, 1107, 943, 887, 880, 862, 845, 814, 783, 754; MS (EI$^+$): m/z (relative intensity, %): 429 ([M+1]$^+$, 20), 428 (M$^+$, 80), 296 ([M+1–$SO_2CF_3$]$^+$, 22), 295 ([M–$SO_2CF_3$]$^+$, 93), 267 ([M–$COSO_2CF_3$]$^+$, 100), 266 ([M–$COSO_2CF_3H$]$^+$, 32); HRMS (EI$^+$): m/z calcd for $C_{21}H_{11}F_3N_2O_3S$ (M) 428.0442, found 428.0447.

### tert-butylphenyl(4-(phenyl(11-(phenyl(4-(phenylamino)phenyl)amino)dibenzo[*a,j*]phenazin-3-yl)amino)phenyl)carbamate (28)

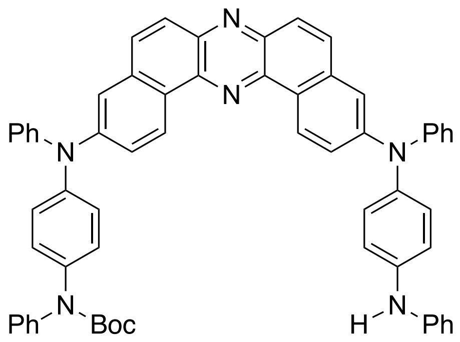

A Schlenk flask (20 mL) equipped with a magnetic stir bar, were added **6b** (800.7 mg, 0.80 mmol), dehydrated $CH_2Cl_2$ (2 mL), and TFA (0.5 mL, 6.5 mmol, 8.2 equiv). The resulting mixture was stirred at room temperature for 30 min. Saturated aqueous $NaHCO_3$ solution was added to the reaction mixture, and the organic layer was extracted with $CH_2Cl_2$ (10 mL × 3). The combined organic extracts were dried over $Na_2SO_4$, which was purified by flash column chromatography on NH silica gel (eluent: *n*-hexane/EtOAc 9:1–8:2). After dried in a vacuum oven at 180 °C for 1 h, product **28** was obtained as red solid in 47% yield (338.1 mg, 0.38 mmol). Mp 194.9 °C (dec.); $R_f$ 0.40 (*n*-hexane/EtOAc 6:4, NH silica); $^1$H NMR (400 MHz, $CDCl_3$): δ 9.35 (d, *J* = 8.8 Hz, 1H), 9.33 (d, *J* = 8.8 Hz, 1H), 7.94 (d, *J* = 9.2 Hz, 1H), 7.92 (d, *J* = 9.2 Hz, 1H), 7.79 (d, *J* = 9.2 Hz, 1H), 7.77 (d, *J* = 9.2 Hz, 1H) 7.55–7.50 (m, 3H), 7.46 (d, *J* = 2.0 Hz, 1H), 7.37–7.07 (m, 27H), 6.93 (t, *J* = 7.2 Hz, 1H), 5.72 (brs, 1H), 1.48 (s, 9H); $^{13}$C NMR (100 MHz, $CDCl_3$): δ 154.0, 149.2, 148.7, 147.4, 147.2, 144.7, 143.2, 142.9, 141.7, 141.6, 141.0, 140.8, 140.5, 139.9, 138.5, 134.7, 134.6, 131.6, 131.3, 129.5, 129.43, 129.40, 128.8, 127.9, 127.45, 127.40, 127.3, 127.1, 126.2, 126.1, 126.0, 125.8, 125.20, 125.17, 125.0, 124.5, 123.9, 123.4, 123.3, 122.4, 121.0, 119.8, 119.1, 118.3, 117.6, 76.7, 28.2; IR (ATR, cm$^{-1}$): 3389, 3057, 1709, 1593, 1504, 1491, 1474, 1354, 1310, 1277, 1258, 1155, 1141, 1055, 1026, 997, 874, 849, 795, 746, 721; MS (FAB$^+$): m/z (relative intensity, %): 897 ([M+H]$^+$, 35), 896 (M$^+$, 33), 796 ([M+H–Boc]$^+$, 13), 795 ([M–Boc]$^+$, 9), 167

([$C_{12}H_9N$]$^+$, 17), 149 ([$C_{10}H_7N_2$]$^+$, 49), 91 ([$C_6H_5N$]$^+$, 12), 89 ([$C_7H_5$]$^+$, 18), 77 ([$C_6H_5$]$^+$, 20), 57 ([*t*-Bu]$^+$, 41); HRMS (FAB$^+$): m/z calcd for $C_{61}H_{48}N_6O_2$ (M) 896.3839, found 896.3835.

**tert-butyl (4-((11-((4-(diphenylamino)phenyl)(phenyl)amino)dibenzo[*a,j*]phenazine-3-yl) (phenyl)amino)phenyl)(phenyl)carbamate (29)**

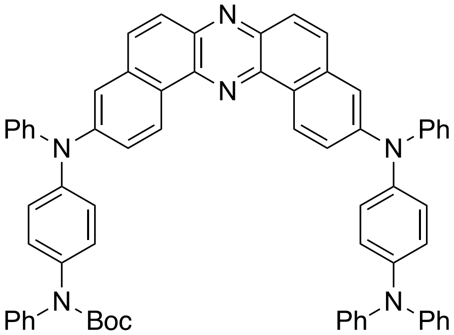

Dehydrated 1,4-dioxane was degassed through freeze-pump-thaw cycling for three times before use. In a glovebox, to a two-necked reaction tube (10 mL) equipped with a magnetic stir bar, was added Pd[P(*t*-Bu)$_3$]$_2$ (10.3 mg, 20 μmol, 10 mol%), and the tube was sealed with a rubber septum and a glass stopper. Outside the glovebox, **28** (179.7 mg, 0.20 mmol), bromobenzene (93.9 mg, 0.60 mmol, 3.0 equiv), $K_2CO_3$ (83.1 mg, 0.60 mmol, 3.0 equiv), and toluene (1 mL) were added to the tube under a stream of $N_2$ gas at room temperature, and the mixture was stirred at 100 °C for 24 h. After the reaction mixture was cooled to room temperature, de-ionized water (5 mL) was added to the reaction mixture, and which was extracted with $CH_2Cl_2$ (10 mL × 3). The combined organic extracts were dried over $Na_2SO_4$, which was purified by flash column chromatography on NH silica gel (eluent: *n*-hexane/EtOAc 8:2). After dried in a vacuum oven at 180 °C for 1 h, product **29** was obtained as red solid in 69% yield (134.1 mg, 0.14 mmol). Mp 229.9 °C; $R_f$ 0.38 (*n*-hexane/EtOAc 7:3, NH silica); $^1$H NMR (400 MHz, $CDCl_3$): δ 9.36 (d, $J$ = 8.8 Hz, 1H), 9.35 (d, $J$ = 8.8 Hz, 1H), 7.94 (d, $J$ = 9.2 Hz, 2H), 7.82 (d, $J$ = 9.2 Hz, 1H), 7.79 (d, $J$ = 9.2 Hz, 1H), 7.57–7.50 (m, 4H), 7.38–7.00 (m, 33H), 1.48 (s, 9H); $^{13}$C NMR (100 MHz, $CDCl_3$): δ 154.0, 149.0, 148.7, 147.7, 147.3, 147.2, 144.7, 144.0, 142.9, 141.9, 141.8, 141.7, 140.9, 140.8, 138.5, 134.7, 134.6, 131.6, 131.4, 129.54, 129.50, 129.3, 128.8, 127.9, 127.5, 127.4, 127.1, 126.4, 126.2, 125.9, 125.8, 125.5, 125.2, 125.1, 125.0, 124.8, 124.1, 123.9, 123.6, 123.3, 122.8, 122.7, 119.8, 118.9, 81.2, 28.3 (one aryl signal was not detected from the NMR chart, due to the overlap with other aromatic resonances); IR (ATR, cm$^{-1}$): 3038, 2930, 1709, 1589, 1504, 1489, 1479, 1354, 1302, 1275, 1155, 1144, 1055, 1026, 876, 849, 795, 750, 721; MS (FAB$^+$): m/z (relative intensity, %): 973 ([M+H]$^+$, 100), 972 ([M]$^+$, 90), 916 ([M+H–*t*-Bu] $^+$, 23), 872 ([M+H–Boc]$^+$, 69), 871 ([M–Boc]$^+$, 37), 705 ([$C_{50}H_{35}N_5$]$^+$, 11), 704 ([$C_{50}H_{34}N_5$]$^+$, 10), 335 ([$C_{24}H_{19}N_2$]$^+$, 13), 168 ([$C_{12}H_{10}N$]$^+$, 19), 167 ([$C_{12}H_9N$]$^+$, 48), 91 ([$C_6H_5N$]$^+$, 10), 89 ([$C_7H_5$]$^+$, 14), 77 ([$C_6H_5$]$^+$, 31), 57 ([*t*-Bu]$^+$, 66); HRMS (FAB$^+$): m/z calcd for $C_{67}H_{52}N_6O_2$ (M) 972.4152, found 972.4174.

### *N*3-(4-(diphenylamino)phenyl)-*N*3,*N*11-diphenyl-*N*11-(4-(phenylamino)phenyl) dibenzo[*a*,*j*]phenazine-3,11-diamine (30)

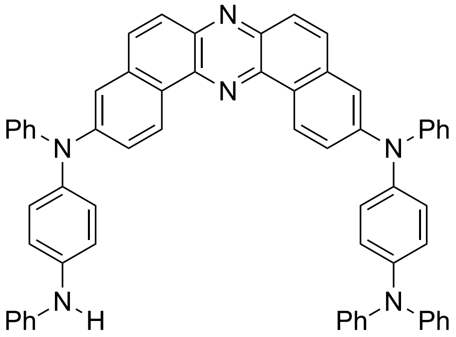

To a Schlenk flask (20 mL) equipped with a magnetic stir bar, were added **29** (146.5 mg, 0.16 mmol), dehydrated $CH_2Cl_2$ (2 mL), and TFA (0.5 mL, 6.53 mmol, 41 equiv). The resulting mixture was stirred at room temperature for 30 min. Saturated aqueous $NaHCO_3$ solution was added to the reaction mixture, and the organic layer was extracted with $CH_2Cl_2$ (10 mL × 3). The combined organic extracts were dried over $Na_2SO_4$, which was purified by flash column chromatography on NH silica gel (eluent: *n*-hexane/EtOAc 8:2–7:3). After dried in a vacuum oven at 180 °C for 1 h, product **30** was obtained as red solid in 98% yield (128.6 mg, 0.15 mmol). Mp 267.1 °C; $R_f$ 0.23 (*n*-hexane/EtOAc 7:3, NH silica); $^1$H NMR (400 MHz, $CDCl_3$): δ 9.36 (d, *J* = 8.8 Hz, 1H), 9.34 (d, *J* = 8.8 Hz, 1H), 7.94 (d, *J* = 8.4 Hz, 1H), 7.92 (d, *J* = 8.8 Hz, 1H), 7.81 (d, *J* = 8.4 Hz, 1H), 7.79 (d, *J* = 8.8 Hz, 1H), 7.56 (dd, *J* = 8.8, 2.0 Hz, 1H), 7.55 (dd, *J* = 8.8, 2.4 Hz, 1H), 7.51 (d, *J* = 2.0 Hz, 1H), 7.47 (d, *J* = 2.0 Hz, 1H), 7.37–7.24 (m, 12H), 7.19–7.00 (m, 20H), 6.94 (t, *J* = 7.2 Hz, 1H), 5.74 (s, 1H); $^{13}$C NMR (100 MHz, $CDCl_3$): δ 149.1, 148.9, 147.7, 147.4, 147.3, 143.9, 143.0, 141.9, 141.6, 141.5, 140.9, 140.8, 140.5, 139.8, 134.62, 134.59, 131.5, 131.4, 129.5, 129.41, 129.38, 129.2, 127.4, 127.3, 126.3, 126.2, 126.1, 125.5, 125.2, 125.0, 124.8, 124.4, 124.0, 123.6, 123.3, 122.8, 122.7, 122.3, 120.9, 119.0, 118.9, 118.3, 117.5 (one aryl signal was not detected from the NMR chart, due to the overlap with other aromatic resonances); IR (ATR, $cm^{-1}$): 3404, 3036, 2926, 1589, 1503, 1489, 1474, 1354, 1310, 1265, 1142, 1107, 1074, 1028, 997, 974, 874, 849, 795, 748, 721; MS (FAB$^+$): m/z (relative intensity, %): 873 ([M+H]$^+$, 25), 872 ([M]$^+$, 27), 167 ([$C_{12}H_9N$]$^+$, 10), 149 ([$C_{10}H_7N_2$]$^+$, 23), 91 ([$C_6H_5N$]$^+$, 10), 89 ([$C_7H_5$]$^+$, 16), 77 ([$C_6H_5$]$^+$, 16); HRMS (FAB$^+$): m/z calcd for $C_{62}H_{44}N_6$ (M) 872.3627, found 872.3649.

### $N^3$-(4-(dibenzo[*a*,*j*]phenazine-3-yl(phenyl)amino)phenyl)-$N^{11}$-(4-(diphenylamino)phenyl)-$N^3$, $N^{11}$-diphenyldibenzo[*a*,*j*]phenazine-3,11-diamine (Linear)

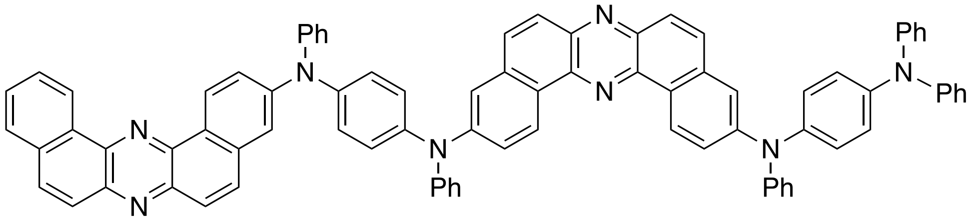

Dehydrated 1,4-dioxane was degassed through freeze-pump-thaw cycling for three times before use. A two necked reaction tube (10 mL) equipped with a magnetic stir bar, a rubber septum, and a glass stopper was flame-dried under reduced pressure and then purged with $N_2$ gas for three times. To the tube, were added **30** (87.3 mg, 0.10 mmol), DBPHZ-Otf **27** (64.3 mg, 0.15 mmol, 1.5 equiv), $Pd_2(dba)_3$ (4.7 mg, 5.1 µmol, 5.1 mol%), Sphos (6.1 mg, 15 µmol, 15 mol%), $K_2CO_3$ (21.1 mg, 0.15 mmol, 1.5 equiv), and 1,4-dioxane (1 mL) under a stream of $N_2$ gas, and the mixture was stirred for 24 h at 100 °C. After the mixture was cooled to room temperature, de-ionized water (5 mL) was added to the reaction mixture, which was extracted with $CH_2Cl_2$ (10 mL × 3). The combined organic extracts were dried over $Na_2SO_4$, and the solvent was removed under reduced pressure to give the crude product. The crude product was washed with a mixed solvent *n*-hexane/EtOAc (9:1, 20 mL) and filtrated. The resulting solid was reprecipitated from a biphasic solution of $CHCl_3$ and *n*-hexane to give product **Linear** as yellow solid in 80% yield (91.6 mg, 80 µmol). Mp 354.7 °C; $R_f$ 0.43 (*n*-hexane/EtOAc 6:4, NH silica).

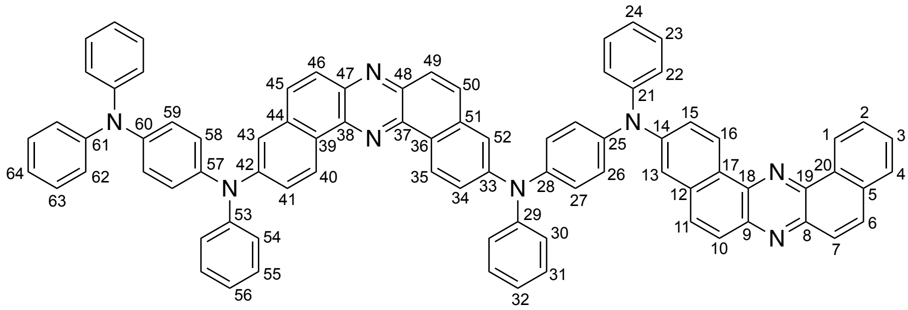

All the $^1$H and $^{13}$C signals were tentatively assigned as shown in the figure below based on the 2D $^1$H-$^1$H and $^1$H-$^{13}$C correlation NMR spectroscopy (see the Figures 7–9). *Note: Due to the lack of correlation information among some segments (e.g., N-Ph groups and the phenylene ring, and the half segment of DBPHZ unit and N-Ph groups) isolated by the nitrogen atoms, some other assignments might be possible: $^1$H NMR (600 MHz, $CDCl_3$): δ 9.59 (d, $J$ = 7.8 Hz, 1H, H$^1$), 9.47 (d, $J$ = 8.4 Hz, 1H, H$^{16}$), 9.40 (d, $J$ = 9.0 Hz, 1H, H$^{35}$), 9.37 (d, $J$ = 9.0 Hz, 1H, H$^{40}$), 8.05 (s, 2H, H$^6$ and , H$^7$), 8.00 (d, $J$ = 9.6 Hz, 1H, H$^{10}$), 7.98 (d, $J$ =7.2 Hz, 1H, H$^4$), 7.97 (d, $J$ = 9.0 Hz, 1H, H$^{49}$), 7.95 (d, $J$ = 9.0 Hz, 1H, H$^{46}$), 7.90 (d, $J$ = 9.0 Hz, 1H, H$^{11}$), 7.85 (d, $J$ = 9.6 Hz, 1H, H$^{50}$), 7.84 (dd, $J$ = 6.6, 1.2 Hz, 1H, H$^{2}$), 7.82 (d, $J$ = 9.6 Hz, 1H, H$^{45}$), 7.79 (dd, $J$ = 7.2, 1.2 Hz, 1H, H$^{3}$), 7.65 (dd, $J$ = 9.0, 2.4 Hz, 1H, H$^{15}$), 7.61 (dd, $J$ = 9.0, 2.4 Hz, 1H, H$^{34}$), 7.58 (d, $J$ = 1.8 Hz, 1H, H$^{13}$), 7.57 (d, $J$ = 2.4 Hz, 1H, H$^{52}$), 7.56 (dd, $J$ = 9.6, 2.4 Hz, 1H, H$^{41}$), 7.51 (d, $J$ = 2.4 Hz, 1H, H$^{43}$), 7.39 (t, $J$ = 7.8 Hz, 2H, H$^{23}$), 7.38 (t, $J$ = 7.8 Hz, 2H, H$^{31}$), 7.35 (t, $J$ = 7.8 Hz, 2H, H$^{55}$), 7.32 (d, $J$ = 5.4 Hz, 2H, H$^{22}$), 7.30 (d, $J$ = 4.8 Hz, 2H, H$^{30}$), 7.28 (t, $J$ = 6.9 Hz, 4H, H$^{63}$), 7.26 (d, $J$ = 6.0 Hz, 2H, H$^{54}$), 7.20 (s, 4H, H$^{26}$ and , H$^{27}$), 7.16 (d, $J$ = 7.2 Hz, 1H, H$^{24}$), 7.15 (t, $J$ = 6.0 Hz, 1H, H$^{32}$), 7.15 (d, $J$ = 7.2 Hz, 4H, H$^{62}$), 7.12 (t, $J$ = 7.2 Hz, 1H, H$^{56}$), 7.11 (d, $J$ = 9.0 Hz, 2H, H$^{58}$), 7.06 (d, $J$ = 8.4 Hz, 2H, H$^{59}$), 7.02 (t, $J$ = 7.2 Hz, 2H, H$^{64}$); $^{13}$C NMR (151 MHz, $CDCl_3$): δ 149.1 (C$^{42}$), 149.02 (C$^{14}$), 148.85 (C$^{33}$), 147.7 (C$^{61}$), 147.32 (C$^{53}$), 147.28 (C$^{29}$), 147.2 (C$^{21}$), 144.0 (C$^{60}$), 143.2 (C$^{25}$), 143.0 (C$^{28}$), 142.4 (C$^{9}$), 142.1 (C$^{8}$), 141.9 (C$^{57}$), 141.8 (C$^{47}$), 141.7 (C$^{48}$), 141.0 (C$^{38}$), 140.9 (C$^{37}$), 140.8 (C$^{18}$), 140.7 (C$^{19}$), 134.69 (C$^{44}$), 134.68 (C$^{51}$), 134.65 (C$^{12}$), 133.4 (C$^{5}$), 132.2 (C$^{11}$), 131.8 (C$^{7}$), 131.6, (C$^{45}$) 131.44 (C$^{50}$), 131.35 (C$^{20}$), 129.64 (C$^{23}$), 129.62 (C$^{31}$), 129.5 (C$^{55}$), 129.3 (C$^{63}$), 129.2 (C$^{3}$), 128.1 (C$^{4}$), 127.52 (C$^{2}$), 127.50 (C$^{49}$), 127.42 (C$^{10}$), 127.39 (C$^{46}$), 127.0 (C$^{6}$), 126.4 (C$^{16}$, C$^{58}$), 126.3 (C$^{35}$), 126.21 (C$^{40}$), 126.19 (C$^{26}$), 126.1 (C$^{27}$), 125.9 (C$^{36}$), 125.8 (C$^{17}$), 125.5 (C$^{39}$), 125.2 (C$^{1}$, C$^{22}$), 125.08 (C$^{30}$), 125.05 (C$^{59}$), 124.8 (C$^{54}$), 124.1 (C$^{62}$), 124.0 (C$^{24}$), 123.9 (C$^{32}$), 123.6 (C$^{56}$), 123.13 (C$^{15}$), 123.12 (C$^{34}$), 122.8 (C$^{41}$), 122.7 (C$^{64}$), 119.5 (C$^{52}$), 119.3 (C$^{13}$), 119.0 (C$^{43}$); IR (ATR, cm$^{-1}$): 3034, 1614, 1591, 1489, 1476, 1356, 1321, 1310, 1281, 1260, 1148, 1001, 976, 858, 849, 795, 750, 734, 721; MS (FAB$^{+}$): m/z (relative intensity, %): 1151 ([M+H]$^{+}$, 11), 1150 ([M]$^{+}$, 10), 91 ([$C_6H_5N$]$^{+}$, 10), 77 ([$C_6H_5$]$^{+}$, 22); HRMS (FAB$^{+}$): m/z calcd for $C_{82}H_{52}N_8$ (M) 1150.4471, found 1150.4478; Anal. Calcd for $C_{82}H_{54}N_8$: C, 4.73; H, 85.54; N, 9.73. found: C, 4.65; H, 85.15; N, 9.35.

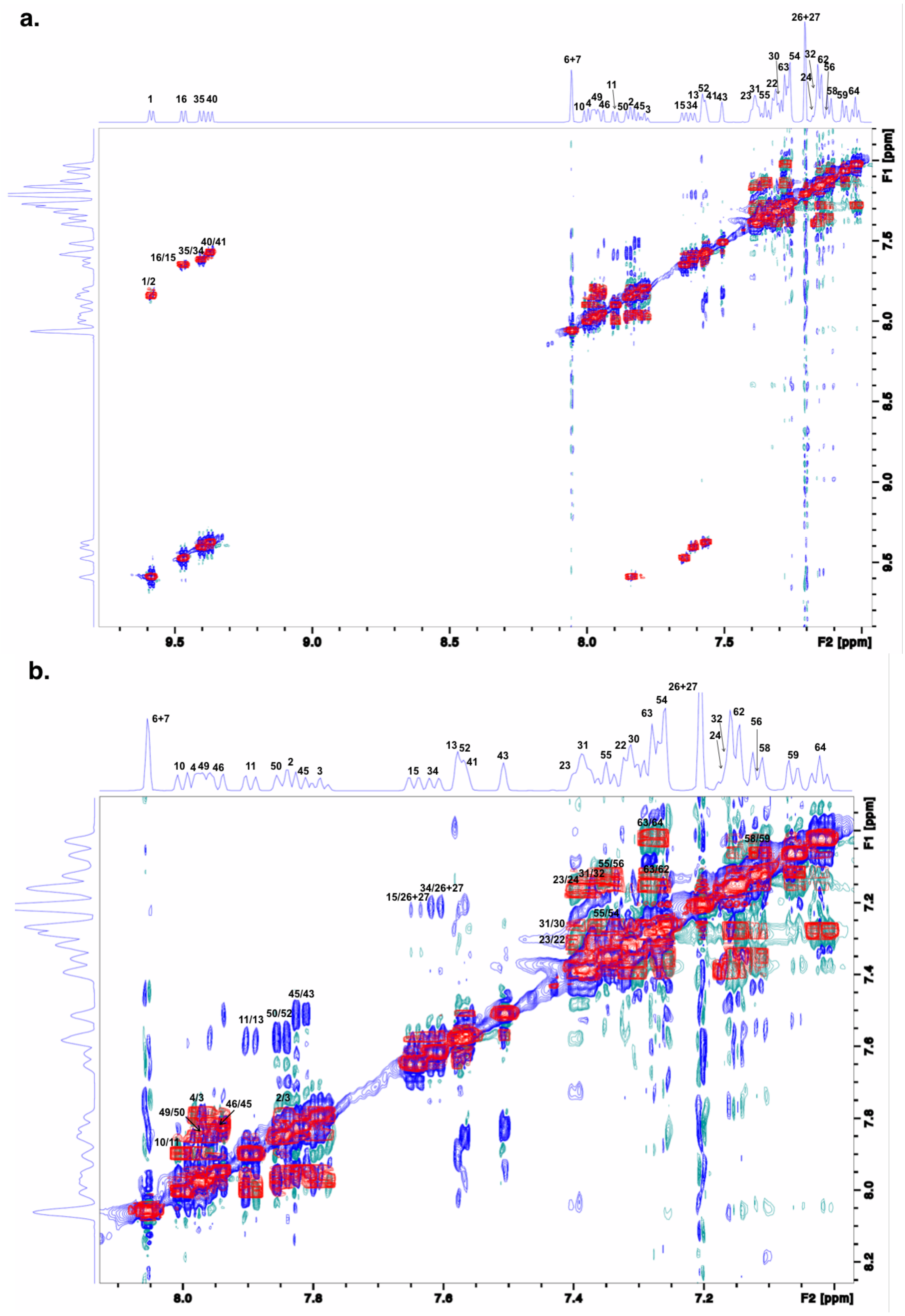

**Figure 11.** (a) 2D $^1$H-$^1$H COSY (red and blue dots) and NOESY (blue-green dots) NMR spectra of **Linear** (600 MHz, $CDCl_3$) and (b) magnified spectra (range: from 7.0 ppm to 8.1 ppm). Reproduced from ref. 10. Copyright 2020 American Chemical Society.

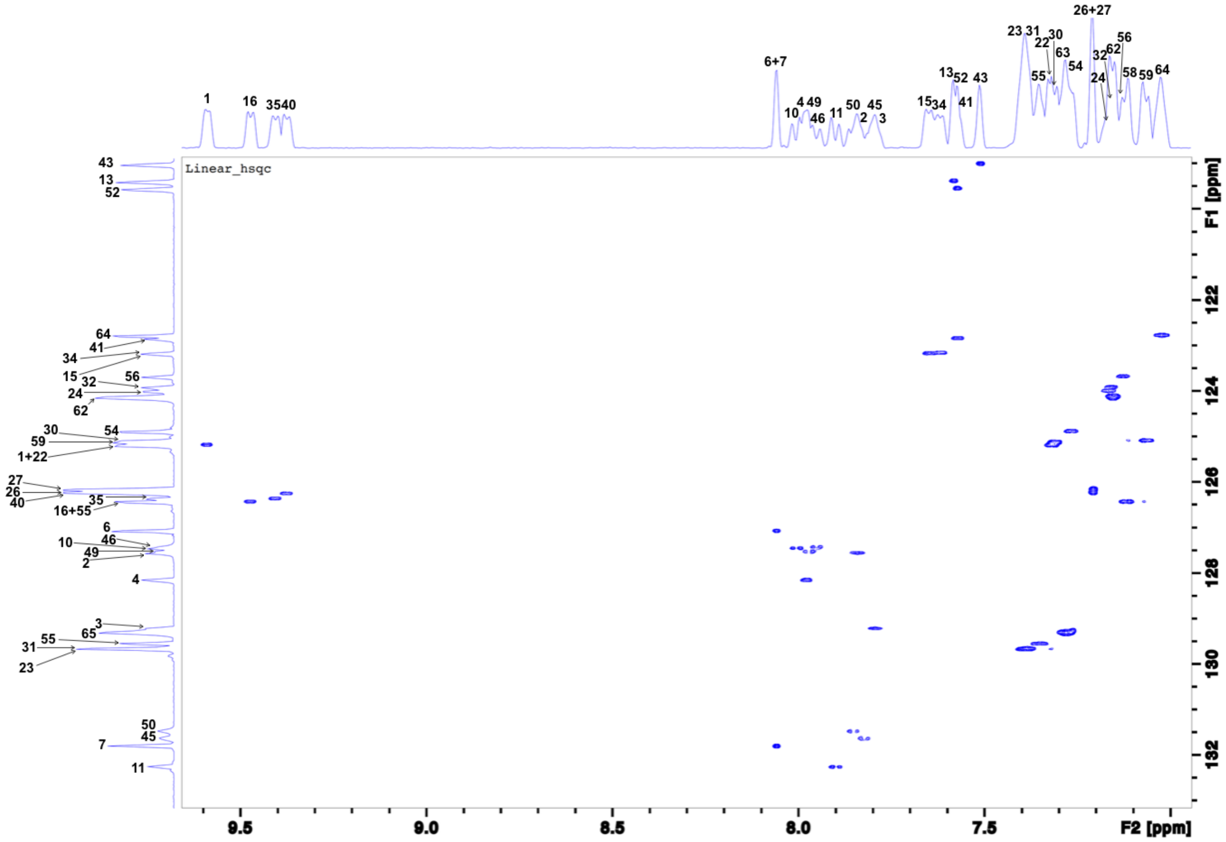

**Figure 12.** 2D $^1$H-$^{13}$C HSQC NMR spectrum of **Linear** (600 MHz, CDCl$_3$). Reproduced from ref. 10. Copyright 2020 American Chemical Society.

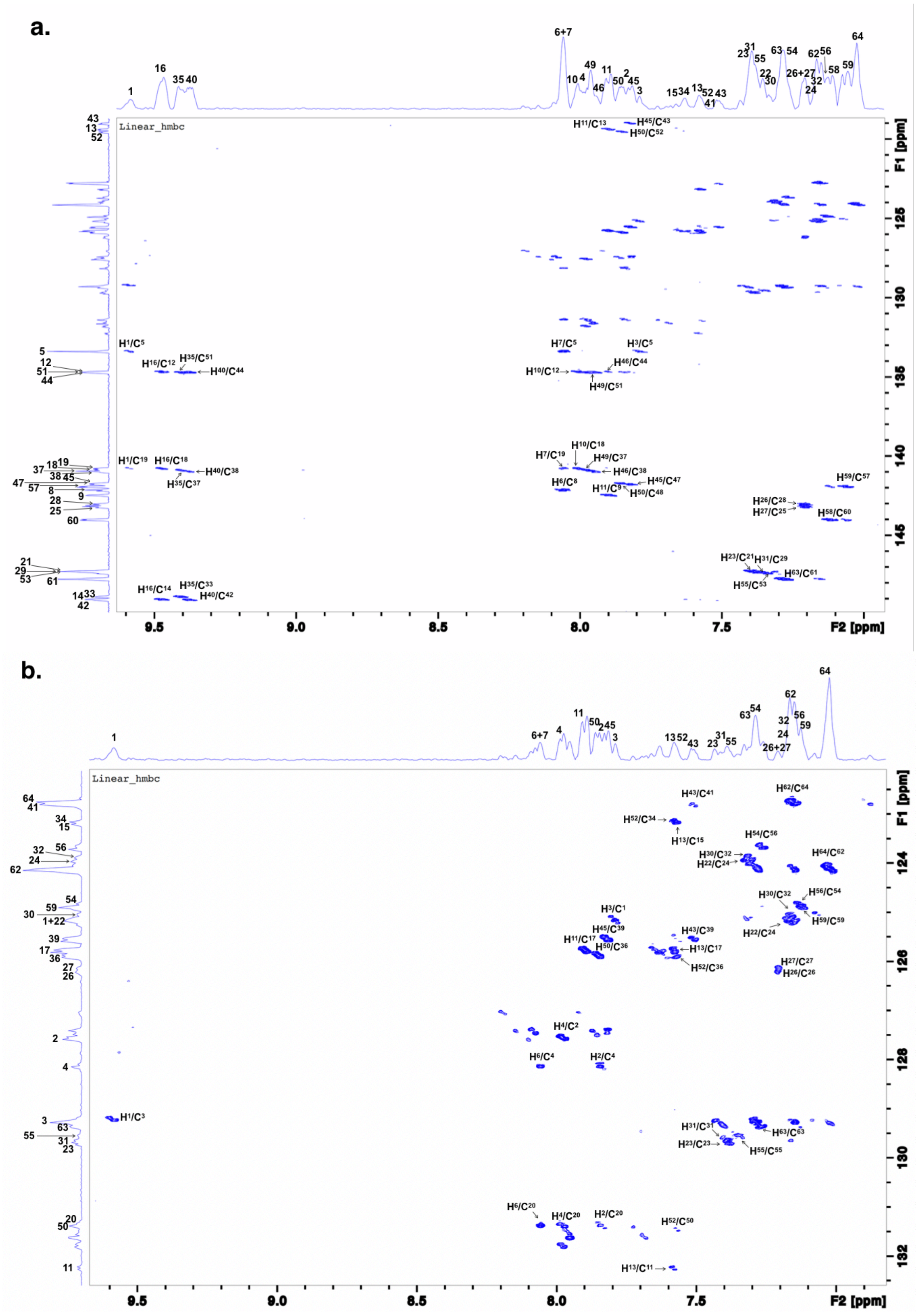

**Figure 13.** (a) 2D $^{1}$H-$^{13}$C HMBC NMR spectrum of **Linear** (600 MHz, CDCl$_3$) and (b) magnified spectra (range: from 122 ppm to 132 ppm (F1)). Reproduced from ref. 10. Copyright 2020 American Chemical Society.

## 1-12. References

1. Takeda, Y.; Okazaki, M.; Minakata, S. *Chem. Commun.* **2014**, *50*, 10291–10294.
2. (a) Data, P.; Pander, P.; Okazaki, M.; Takeda, Y.; Minakata, S.; Monkman, A. P. *Angew. Chem., Int. Ed.* **2016**, *55*, 5739−5744. (b) Okazaki, M.; Takeda, Y.; Data, P.; Pander, P.; Higginbotham, H.; Monkman, A. P.; Minakata, S. *Chem. Sci.* **2017**, *8*, 2677–2686. (c) Data, P.; Okazaki, M.; Minakata, S.; Takeda, Y. *J. Mater. Chem. C* **2019**, *7*, 6616−6621. (d) Takeda, Y.; Kaihara, T.; Okazaki, M.; Higginbotham, H.; Data, P.; Tohnai, N.; Minakata, S. *Chem. Commun.* **2018**, *54*, 6847−6850.
3. Martí-Centelles, V.; Pandey, M. D.; Burguete, M. I.; Luis, S. V. *Chem. Rev.* **2015**, *115*, 8736−8834.
4. Sobolev, A. N.; Belsky, V. K.; Romm, I. P.; Chernikova, N. Y.; Guryanova, E. N. *Acta Crystallogr., Sect. C: Cryst. Struct. Commun.* **1985**, *41*, 967−971.
5. Chen, R.; Benicewicz, B. C. *Macromolecules* **2003**, *36*, 6333–6339.
6. Eelkema, R.; Anderson, H. L. *Macromolecules* **2008**, *41*, 9930–9933.
7. Kataoka, N.; Shelby, Q.; Stambuli, J. P.; Hartwig, J. F. *J. Org. Chem.* **2002**, *67*, 5553–5566.
8. Lim, Y.-K.; Jung, J.-W.; Lee, H.; Cho, C.-G. *J. Org. Chem.* **2004**, *69*, 5778–5781.
9. Tam, V. K.; Liu, Q.; Tor, Y. *Chem. Commun.* **2006**, 2684–2686.
10. Izumi, S.; Higginbotham, H. F.; Nyga, A.; Stachelek, P.; Tohnai, N.; de Silva, P. Data, P.; Takeda, Y.; Minakata, S. *J. Am. Chem. Soc.* **2020**, *142*, 1482–1491.
11. Grossman, O.; Rueck-Braun, K.; Gelman, D. *Synthesis* **2008**, 537–542.
12. Hempe, M.; Schnellbächer, L.; Wiesner, T.; Reggelin, M. *Synthesis* **2017**, *49*, 4489–4499.
13. Yu, J.; Wang, Y.; Zhang, P.; Wu, J. *Synlett* **2013**, *24*, 1448–1454.
14. Izumi, S.; Nyga, A.; de Silva, P.; Tohnai, N.; Minakata, S.; Data, P.; Takeda, Y.; *Chem. Asian J.* **2020**, *15*, 4098–4103.

# Chapter 2

# Structures and Physicochemical Properties of D–A–D–A π-Conjugated Macrocycles

## 2-1. Structure of Macrocycles

The structures of ***p*-MC** and ***m*-MC** were revealed by single-crystal X-ray crystallographic analyses. ***p*-MC** formed two polymorphs depending on recrystallization conditions: orange prism crystals (denoted as "polymorph ***p*-MC**-O") were grown from a *n*-hexane/$CHCl_3$ biphasic solution through a liquid–liquid diffusion technique, while deep-red prism crystals (denoted as "polymorph ***p*-MC**-R") formed through slow evaporation of a $CHCl_3$ solution of ***p*-MC** over two weeks. Notably, significant differences in molecular geometries and packing structures were found between the two polymorphs (Figure 1 and 2).[1] The polymorph ***p*-MC**-O formed a triclinic system with the space group *P*1 and exhibited weak orange emission under a irradiation of a UV light ($\lambda_{max}$ 594 nm, $\Phi_{PL}$ 0.01; for the photoluminescence (PL) spectra, see Figure 11a in the Experimental Section). In the crystal, the macrocycle takes a highly symmetric structure with the symmetric center (*i*) (Figure 1a). As designed, the donor units take a propeller-structure, with the twisting angles between the phenylene and external *N*-phenyl planes being

85.6° and 88.9° (Figure 1b). The phenylene planes of the donors are also twisted against the DBPHZ acceptor unit, with the dihedral angles between the phenylene plane and the terminal benzene unit of the DBPHZ being 56.9° and 62.8°. Intriguingly, both DBPHZ units are helically twisted, with the dihedral angle between the terminal fused benzene rings being 17.4° (Figure 1b), while the central phenazine unit is nearly flat (deviation angle: 5.9°). The twist of the DBPHZ would indicate that a large strain energy is accommodated into the molecule through the process of macrocyclization. In the crystal polymorph ***p*-MC**-O, the macrocycle molecules align along the *c* axis, and the highly organized assemblies form porous columns with the cavity diameter of 6.58 Å, where chloroform molecules are trapped within the cavity (Figure 1c). Looking closer at the columns, the benzo[*f*]quinoxaline moieties of the DBPHZ unit are contiguously stacked in a face-to-face manner with a very close interplane distance (3.39 Å), which indicates the existence of a strong electronic interaction between the molecules through π-orbitals.

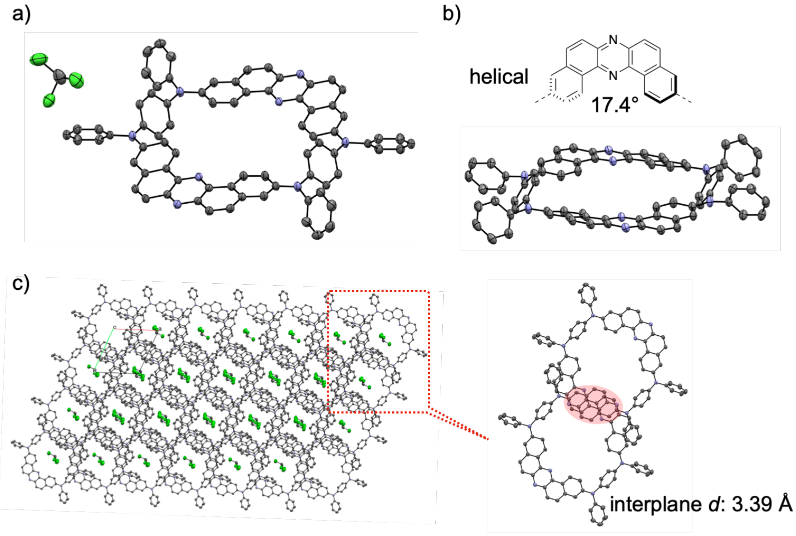

**Figure 1.** ORTEP drawings of ***p*-MC** in polymorph ***p*-MC**-O: (a) a molecular structure; (b) a side view; and (c) packing structure (thermal ellipsoids are set at the 50% probability level). The hydrogen atoms and partial crystal solvents $CHCl_3$ were omitted for clarity. Adapted from ref. 2. Copyright 2020 American Chemical Society.

The polymorph ***p*-MC**-R crystallized in the monoclinic space group $P2_1$/m and exhibited weak red emission ($\lambda_{\mathrm{max}}$ 654 nm, $\Phi_{\mathrm{PL}}$ 0.01; for the PL spectra, see Figure 11a). Importantly, in this crystal, the macrocycle takes a saddle-shaped conformation unlike the helical structure in the polymorph ***p*-MC**-O (Figure 2a and b). The phenylene donor units once again take a propeller shape (the twisting angles between the phenylene and external N-phenyl planes range from 72.8° to 82.3°), and the phenylene unit is more twisted against the acceptor than in the polymorph ***p*-MC**-O (the dihedral angle between the phenylene plane and the terminal benzene unit of the DBPHZ: 66.6°). In sharp contrast to polymorph ***p*-MC**-O, the DBPHZ units of the macrocycle in polymorph ***p*-MC**-R are flat (Figure 2b). The less distortion of the DBPHZ units allow for a more thermodynamically stable conformation than that in ***p*-MC**-O, which was indeed supported by the theoretical calculations by the density functional theory (DFT) method (see the following paragraph). Each porous column independently aligns along the *a* axis in polymorph ***p*-MC**-R, with the voids among each column being filled with chloroform molecules (Figure 2c). Interestingly, in each column, donor moieties and acceptor moieties are alternately stacked with a very close distance (the interplane distances between the phenylene and the DBPHZ plane: 2.98–3.18 Å, Figure 2c) like dimeric pairs of the macrocycle forming four D···A pairs. This would indicate that strong intermolecular charge-transfer interactions between the two molecules are operative, which would be in good agreement with a significant red-shift in absorption and emission wavelength (Figure 11 in the Experimental Section).

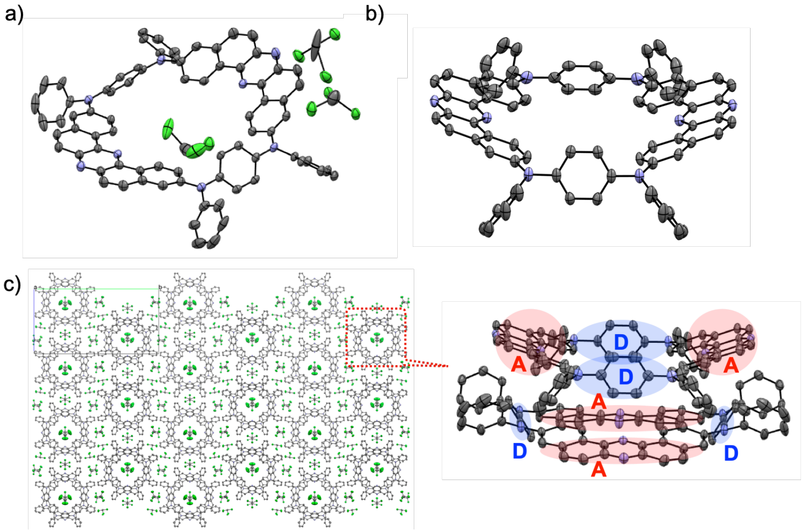

**Figure 2.** ORTEP drawings of ***p*-MC** in polymorph ***p*-MC**-R: (a) a molecular structure; (b) a side view; and (c) packing structure (thermal ellipsoids are set at the 50% probability level). The hydrogen atoms and partial crystal solvents $CHCl_3$ were omitted for clarity. Adapted from ref. 2. Copyright 2020 American Chemical Society.

To compare the stability between the conformations of ***p*-MC** in the two polymorphs, the DFT calculations with the several exchange-correlation functionals were conducted. The structural optimization of ***p*-MC** was conducted with the geometries obtained from the X-ray crystallographic analyses. The comparison of the energies of helical-type conformer (denoted as "**helical**") related to that found in the polymorph ***p*-MC**-O (Figure 1) and of saddle-type conformer (denoted as "**saddle**") related to that found in the polymorph ***p*-MC**-R (Figure 2) revealed that there is a large energy difference between these conformers. The **saddle** is approximately 5 kcal/mol stable than the **helical** (for detailed values, see Table 7 in the Experimental Section), suggesting that >99% of the ***p*-MC** takes the saddle-like conformation as the single molecule. This thermodynamic preference of the saddle conformer would rationally explain the experimental observation that polymorph ***p*-MC**-O (**helical** conformer) was obtained under kinetic crystallization conditions, while polymorph ***p*-MC**-R (**saddle** conformer) was formed under thermodynamic conditions, although the packing effect cannot be completely excluded.

On one hand, ***m*-MC** was recrystallized as tiny orange single crystals from *n*-hexane/1,2-

dichlorobenzene biphasic solution. Although ***p*-MC** exhibited two different polymorphs with different conformers (**helical** and **saddle** conformers), ***m*-MC** formed only one polymorph with the single conformer (Figure 3). In the crystal, ***m*-MC** takes a saddle conformation in a similar with ***p*-MC**-R (Figure 3a). The interplane angle of the two DBPHZ planes is much smaller (91°) than that of ***p*-MC**-R (148°), reflecting the closer distance of the two N atoms on the phenylene donor (Figure 3b). In the crystal, ***m*-MC** forms a 1D self-assembled structure, where intermolecular DBPHZ units stack, with the contact between adjacent molecules being 3.43 Å (Figure 3c). According to the conformational search, as in the case of ***p*-MC**, the saddle shape is the most stable conformer, which is ca. 4 kcal $mol^{-1}$ more stable than the secondarily stable conformer (for details, see the Experimental Section). By the irradiation of a UV light, the solids of ***m*-MC** showed orange emission ($\lambda_{em}$ 636 nm) with a low PLQY ($\Phi_{PL}$ 0.04) (Figure 12 in the Experimental Section). Compared with the PL of ***p*-MC**-R ($\lambda_{em}$ 654 nm, $\Phi_{PL}$ 0.01), the PL of the solids of ***m*-MC** was observed in the slightly blue-shifted region. This suggests that ***m*-MC** has a weaker charge-transfer nature in the excited states than ***p*-MC**, which is matches with the solvatochromic behavior of ***m*-MC** in organic solvents (*vide infra)*.

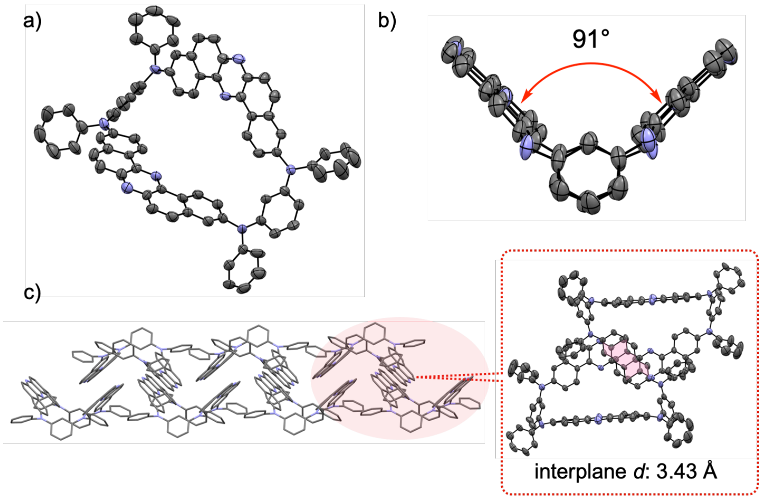

**Figure 3.** ORTEP drawings of ***m*-MC**: (a) a molecular structure; (b) a side view (all the N-Ph groups were omitted for clarity); and (c) packing structures (thermal ellipsoids are set at the 50% probability level). The hydrogen atoms and solvent molecules were omitted for clarity. Adapted from ref. 3. Copyright 2020 Wiley-VCH Verlag GmbH.

The crystal of **Linear** was not obtained regardless of a number of attempts, implying the more flexibility of the conformations than macrocycles. The solids of **Linear** displayed an orange PL ($\lambda_{\mathrm{max}}$ 605 nm, $\Phi_{\mathrm{PL}}$ 0.08; for the PL spectra, see Figure 11b in the Experimental Section) with a slightly higher PLQY than those of ***p*-MC** polymorphs, which indicates that the strong electronic interactions of macrocycle quench PL in the crystal. According to the conformational search, the most stable conformer takes a twisted geometry (see the following section, Figure 7).

### 2-2. Steady-State Photophysical Properties

To investigate fundamental photophysical properties of ***p*-MC**, **Linear** and ***m*-MC**, the steady-state UV-vis absorption (Abs) and PL spectra of their diluted solutions ($c \sim 10^{-5}$ M) were acquired (Figure 4, 6, 8, and Table 1–3). As a whole, the line shapes, the maximum absorption wavelength ($\lambda_{\mathrm{abs}}$), and molar absorption coefficients ($\varepsilon$) of the UV–vis absorption spectra of diluted solutions of ***p*-MC** were not significantly affected by the difference in polarity of solvents used (Figure 4 and Table 1). However, on close investigation of the absorption onsets of solutions of ***p*-MC**, a slight red-shift was observed as a function of solvent polarity (Figure 4). The absorption peaked at around 470 nm showed a relatively large $\varepsilon$ value (ca. 50,000 $\mathrm{M}^{-1}$ $\mathrm{cm}^{-1}$), which was not formed in the absorption spectra of DBPHZ[4] and TPDA,[5] indicating that the electronic transition observed at around 470 nm has the mixed character of intramolecular charge-transfer (ICT) and $\pi$–$\pi$* transition or hybrid CT (Figure 4). To support the experimental data, the TD-DFT calculations were conducted on the conformers obtained from the X-ray crystallographic analyses. For both conformers (**saddle** and **helical**) of the macrocycle ***p*-MC**, the HOMO and HOMO−1 orbitals are delocalized over the entire ring, whereas the LUMO and LUMO+1 orbitals are mostly on the acceptors (Figure 5), as expected. The localization of unoccupied frontier orbitals is more pronounced for the saddle conformer. The lowest singlet excited state for both conformers is dominated by the HOMO→LUMO transition but is symmetrically forbidden (red arrows in Figure 5). The second and third electronic transitions are allowed and dominated by HOMO→LUMO+1 (green arrows) and HOMO−1→LUMO (blue arrows) transitions, respectively (Figure 5). The comparison of the calculated and experimental UV–vis spectra (Figure 15 in the Experimental Section) for both conformers of ***p*-MC** in toluene indicates that the saddle-type conformer is dominant in diluted solutions. This is supported by the closer match of the lowest absorption peak as well as the fact that only the calculated spectrum for the **saddle** shows a double peak in the 300–400 nm range (Figure 15b in the Experimental Section). The comparison of the spectra is also consistent with the thermodynamic stability of both conformers. The experimental lowest-lying absorption peak of ***p*-MC** is very close to the symmetry-forbidden transition to $S_1$ in **saddle** (476 nm), which suggests the mixing of electronic states through vibrations would make the transition to $S_1$ allowed. This would lead to the red-shift of the calculated band and increase of its intensity, thereby improving the agreement with the experiment. An analogous mixing of states to make forbidden transitions allowed has been recently proposed in the four-state model of TADF to explain the possibility of simultaneous efficient rISC and fluorescence in donor–acceptor TADF emitters.[6] In contrast to absorption spectra, PL spectra of ***p*-MC** in solutions were affected by solvent polarity change (Figure 4 and Table 1). Under the UV light, ***p*-MC** in the cyclohexane displayed bright green emission from the singlet charge-transfer excited state ($^1$CT) ($\lambda_{em}$ 540 nm) with a moderate PLQY ($\Phi_{PL}$ 0.31). Slightly polar toluene solution of ***p*-MC** showed orange emission ($\lambda_{em}$ 595 nm, $\Phi_{PL}$ 0.28) from the more stabilized $^1$CT state. In more polar solvents (e.g., THF, $CH_2Cl_2$, and $CHCl_3$), ***p*-MC** exhibited no emission, indicating strong ICT nature in the excited states of the macrocycle.[7]

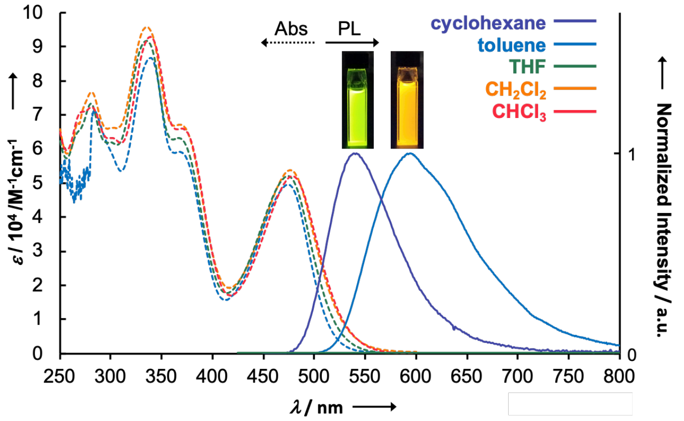

**Figure 4.** Steady-state UV–vis absorption and photoluminescence spectra of dilute solutions (purple, cyclohexane; sky blue, toluene; green, THF; orange, $CH_2Cl_2$; red, $CHCl_3$) of ***p*-MC** ($\lambda_{ex}$ = 340 nm, *c*: $10^{-6}$–$10^{-5}$ M). Adapted from ref. 2. Copyright 2020 American Chemical Society.

**Table 1.** Summary of steady-state photophysical data of solutions of ***p*-MC**.

| solvent[a] | $\lambda_{abs}$ (nm) | $\lambda_{PL}$ (nm) | $\Phi_{PL}$ (nm)[b] |
|---|---|---|---|
| cyclohexane[c] | 268, 338, 370, 476 | 540 | 0.31 |
| toluene | 283, 336, 367, 473 | 595 | 0.28 |
| THF | 280, 335, 366, 474 | ND | <0.01 |
| $CH_2Cl_2$ | 281, 335, 368, 476 | ND | <0.01 |
| $CHCl_3$ | 281, 339, 369, 478 | ND | <0.01 |

[a]Concentration: $10^{-5}$ M. [b]Determined with an integrated sphere.
[c]Saturated solution was used, due to the low solubility in cyclohexane.

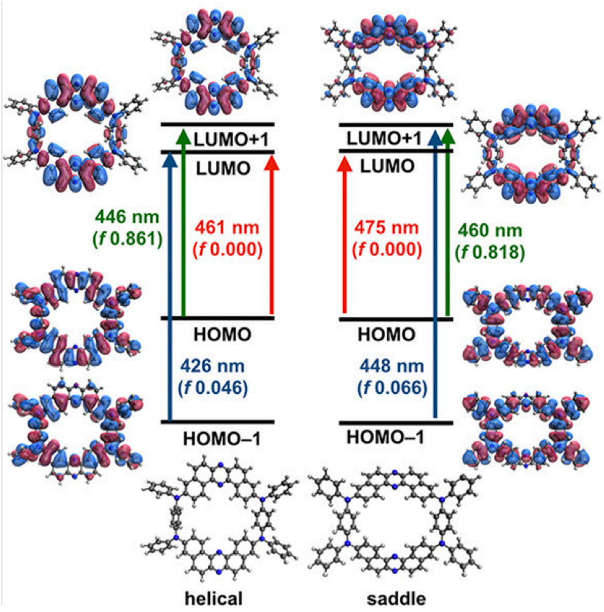

**Figure 5.** An illustrative summary of the theoretical calculations for helical and saddle-shaped conformers of ***p*-MC** at the *ω**PBE/cc-pVDZ level. The first three vertical electronic transitions are shown in red, green, and blue arrows. Adapted from ref. 2. Copyright 2020 American Chemical Society.

From the diluted solutions of **Linear**, similar absorption spectra with an ICT peak ($\lambda_{\mathrm{abs}}$ 477−485 nm) and the π–π* transition ($\lambda_{\mathrm{abs}}$ 332−337 nm) assigned to the TPDA unit were obtained (Figure 6). When closely compared to ***p*-MC**, **Linear** displayed a broader band with a slightly smaller $\varepsilon$, which could indicate the fluctuation of the conformers. From the calculations, it was revealed that the occupied frontier orbitals are rather delocalized, however most of the amplitude is clearly localized on the donor (Figure 7). The unoccupied frontier orbitals are mostly localized on the acceptor units, similar to that for the macrocycles (Figure 7). The TD-DFT calculation for the energetically lowest conformer of **Linear** suggested that the absorption peak at around 480 nm is composed of three nearly lying excitations, which are dominated by the HOMO−1→LUMO, HOMO→LUMO+1, and HOMO−1→LUMO+1 transitions, respectively (Figure 7). The calculated spectrum also matches the experimental spectrum rather well (Figure 16 in the Experimental Section). In particular, the predicted absorption peak is shown at 485 nm, which is very close to the experimental one at 479 nm. As is the case with ***p*-MC**, **Linear** in solutions showed PL, which were affected by the difference of the solvent polarity (Figure 6 and Table 2). The cyclohexane solution of **Linear** exhibited a green emission ($\lambda_{\mathrm{em}}$ 534 nm) similar to that of ***p*-MC**, but with a higher $\Phi_{\mathrm{PL}}$ (0.53). Notably, **Linear** in toluene showed a red emission ($\lambda_{\mathrm{em}}$ 615 nm) with a lower $\Phi_{\mathrm{PL}}$ (0.20). It is noteworthy that the larger red-shift in emission ($\lambda_{\mathrm{em}}$ 2466 $\mathrm{cm}^{-1}$ for **Linear** *vs* 1712 $\mathrm{cm}^{-1}$ for ***p*-MC**) would indicate that the conformation of **Linear** in the excited states is much more flexible than that of ***p*-MC**, probably due to free D–A rotation around the connecting bond leading to the dissipation of the excited energies through thermal processes.[8]

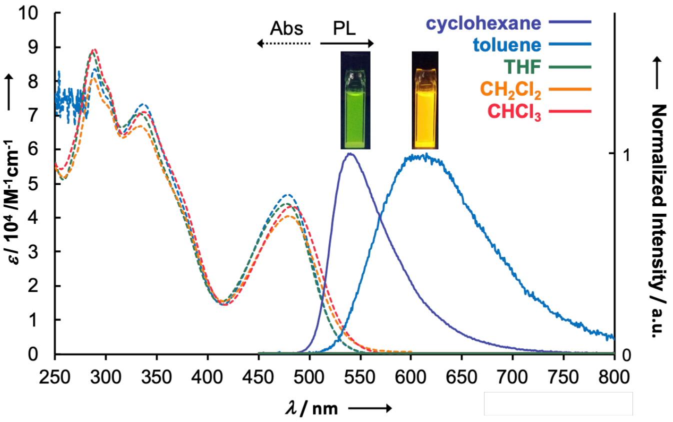

**Figure 6.** Steady-state UV–vis absorption and photoluminescence spectra of dilute solutions (purple, cyclohexane; sky blue, toluene; green, THF; orange, $CH_2Cl_2$; red, $CHCl_3$) of **Linear** ($\lambda_{ex} = 340$ nm, $c$: $10^{-6}$–$10^{-5}$ M). Adapted from ref. 2. Copyright 2020 American Chemical Society.

**Table 2.** Summary of steady-state photophysical data of solutions of **Linear**.

| solvent[a] | $\lambda_{abs}$ (nm) | $\lambda_{PL}$ (nm) | $\Phi_{PL}$ (nm)[b] |
|---|---|---|---|
| cyclohexane[c] | 286, 334, 475 | 534 | 0.53 |
| toluene | 289, 336, 479 | 615 | 0.20 |
| THF | 286, 332, 477 | ND | <0.01 |
| $CH_2Cl_2$ | 288, 334, 479 | ND | <0.01 |
| $CHCl_3$ | 288, 337, 485 | ND | <0.01 |

[a] Concentration: $10^{-5}$ M. [b] Determined with an integrated sphere.
[c] Saturated solution was used, due to the low solubility in cyclohexane.

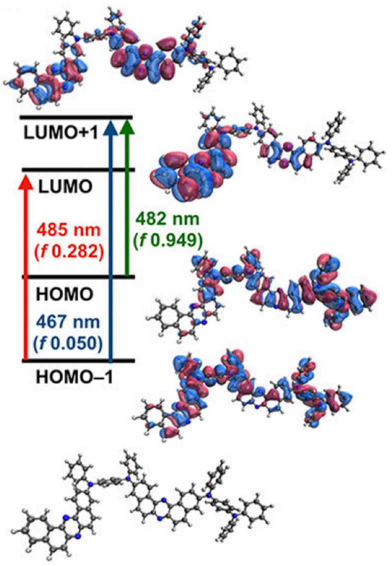

**Figure 7.** An illustrative summary of the theoretical calculations for helical and saddle-shaped conformers of **Linear** at the $\omega$*PBE/cc-pVDZ level. The first three vertical electronic transitions are shown in red, green, and blue arrows. Adapted from ref. 2. Copyright 2020 American Chemical Society.

***m*-MC** also displayed similar UV-vis absorptions with intramolecular charge-transfer (ICT) transition at around $\lambda_{\mathrm{abs}}$ 470 nm, which is mainly ascribed to the HOMO→LUMO transition (for details, see the Experimental Section), and π-π* transitions at around $\lambda_{\mathrm{abs}}$ 315 nm (Figure 8, dotted lines). The experimental absorption spectra of ***m*-MC** in toluene nicely agreed with the simulated one using the conformation found in the single crystal (saddle shape) (Figure 18 in the Experimental Section). Considering that the saddle shape is the most stable conformer, almost all the ***m*-MC** molecules take saddle conformer in solutions, as is the case with ***p*-MC**. Similar to ***p*-MC**, the absorption peaked at around $\lambda_{\mathrm{abs}}$ 470 nm is ascribed to a hybrid type CT, because the onset in the lower energy region ($\lambda_{\mathrm{abs}}$ 500–550 nm) slightly red-shifting as increasing of the solvent polarity. When the absorption spectra of ***m*-MC** are compared with those of ***p*-MC**, both of the ICT and π-π* bands of ***m*-MC** are located in the bluer region than ***p*-MC** by ca. 10 nm, due to shorter effective conjugation length of the phenylenediamine unit of ***m*-MC** than ***p*-MC**. ***m*-MC** nicely displayed positive solvatoluminochromism as a function of solvent polarity (Figure 8). Given that the UV-vis absorption is less affected by solvent polarity, when compared to PL spectra, ***m*-MC** has a much larger charge transfer nature in the excited states rather than in the ground states, as same as ***p*-MC**. In contrast to ***p*-MC**, ***m*-MC** showed emission even in highly polar solvents such as DMF (Figure 8 and Table 3), which indicates a much larger CT character of ***p*-MC** in the excited states. Interestingly, the solvatochromic behavior of ***p*-MC** is very similar with that of 3,11-bis(*N*,*N*-diphenylamino)-substituted DBPHZ, which is regarded as the half structure of the macrocycle.[7b] Take together with the result of absorption and PL of ***p*-MC** and ***m*-MC**, it would be safe to conclude that the CT nature in excited state is strongly influenced by the topology of the phenylene unit in the D–A–D–A macrocycle, probably due to the difference in effective π-conjugation length through the molecule.

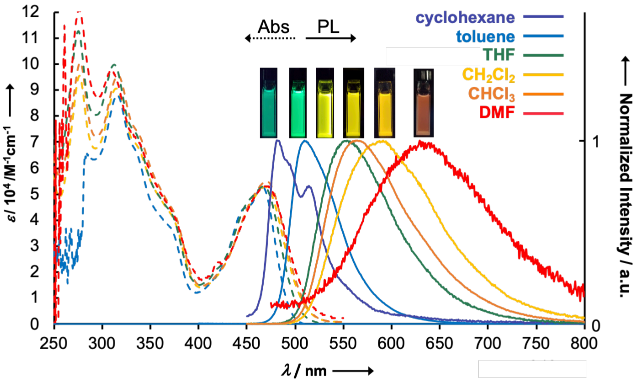

**Figure 8.** Steady-state UV–vis absorption and photoluminescence spectra of dilute solutions (purple, cyclohexane; sky blue, toluene; green, THF; yellow, $CH_2Cl_2$; orange, $CHCl_3$; DMF, red) of ***m*-MC** ($\lambda_{ex}$ = 340 nm, *c*: $10^{-6}$–$10^{-5}$ M). Adapted from ref. 3. Copyright 2020 Wiley-VCH Verlag GmbH.

**Table 3.** Summary of steady-state photophysical data of solutions of ***m*-MC**.

| solvent[a] | $\lambda_{abs}$ (nm) | $\lambda_{PL}$ (nm) | $\Phi_{PL}$ (nm)[b] |
|---|---|---|---|
| cyclohexane[c] | – | 481 | 0.30 |
| toluene[c] | 285, 316, 466 | 509 | 0.39 |
| THF[c] | 275, 313, 467 | 554 | 0.46 |
| $CH_2Cl_2$ | 277, 315, 469 | 591 | 0.43 |
| $CHCl_3$ | 277, 316, 470 | 564 | 0.35 |
| DMF[c] | 277, 310, 470 | 629 | 0.07 |

[a] Concentration: $10^{-5}$ M. [b] Determined with an integrated sphere.
[c] Saturated solution was used, due to the low solubility.

## 2-3. Electrochemical Properties

To investigate the electrochemical properties of the macrocycles and the linear compound, cyclic voltammetry experiments were performed (Figure 9). ***p*-MC** and **Linear** exhibited a reversible one-step reduction (${}^{red}E_{1/2}$ = –1.88 V for ***p*-MC**; –1.89 V for **Linear** vs Fc/$Fc^+$) and a two-step oxidation process (${}^{ox1}E_{1/2}$ = +0.27 V for ***p*-MC**; +0.22 V for **Linear** vs Fc/$Fc^+$, ${}^{ox2}E_{1/2}$ = +0.69 V for ***p*-MC**; +0.63 V for **Linear** vs Fc/$Fc^+$) (Figure 9), indicating their sufficient electrochemical stabilities suitable for carrier injection/transportation in optoelectronic devices. The ionization potential (IP)/electron affinity (EA) of ***p*-MC** and **Linear** determined by the CV experiments are estimated to be 5.37 eV/3.22 eV and 5.32 eV/3.21 eV, respectively. The EA of

***p*-MC** and **Linear** are very close to that of DBPHZ (3.22 eV).[4] The IPs of ***p*-MC** and **Linear** are similar to that of TPDA (5.28 eV)[9] but slightly lowered, probably due to the presence of electron-withdrawing aryl moieties (DBPHZ) on the donor units.[10] Consequently, these data would suggest the localization of the HOMO and LUMO orbitals of both compounds on the donors and acceptors, respectively, which would be beneficial for small $\Delta E_{ST}$. This is also in consistent with theoretically calculated IPs by the DFT ($^{calc}$IP for ***p*-MC**: 5.10 eV, $^{calc}$IP for **Linear**: 5.00 eV) (Table 12 in the Experimental Section). The calculations also reveal that the two electrons can be removed at almost the same potential ($^{calc}$IP1 (radical cation) for ***p*-MC**: 5.10 eV, $^{calc}$IP2 (diradical dication) for ***p*-MC** 5.03 eV) to form a diradical dication, suggesting the 2-electron transfer process of the first oxidation wave in the CV (Table 12 in the Experimental Section). It is noted that mono- and di-cations may still be mixed by the kinetic factor. According to the calculations, the second oxidation wave would correspond to further oxidation to monoradical trication and closed-shell tetracation, which are more thermodynamically stable than triradical and tetraradical species.

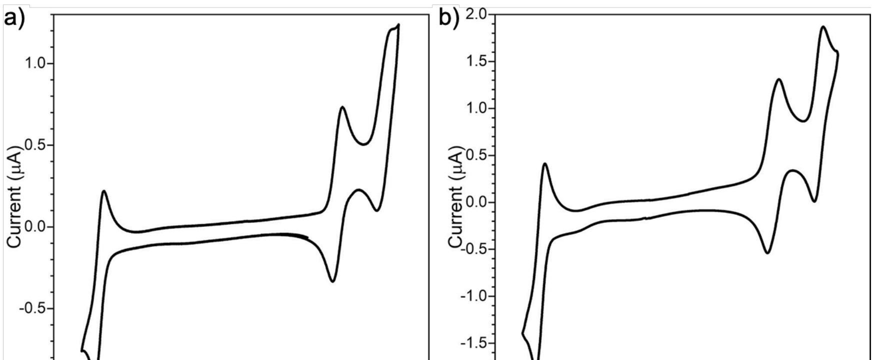

**Figure 9.** Cyclic voltammograms of (a) ***p*-MC** ($5\times10^{-4}$ M) and (b) **Linear** ($1\times10^{-3}$ M) in $CH_2Cl_2$ containing 0.1 M *n*-$Bu_4NBF_4$. Electrodes: working (Pt), counter (Pt wire), reference (Ag/AgCl). Scan rate: 50 mV $s^{-1}$. Adapted from ref. 2. Copyright 2020 American Chemical Society.

In contrast to above compounds, ***m*-MC** showed one reversible reduction ($^{red}E_{1/2} = -1.93$ V vs Fc/Fc$^+$) and only one irreversible oxidation ($^{ox}E = +0.41$ V vs Fc/Fc$^+$) (Figure 10a). The IP/

EA of ***m*-MC** determined by the CV experiments are estimated to be 5.51 eV/3.17 eV. These values are close to the IP of the donor unit *N*,*N*,*N*’,*N*’-tetraphenyl-*m*-phenylenediamine (5.52 eV)[11] and the EA of the acceptor unit DBPHZ (3.22 eV),[4] respectively. This suggests that the HOMO and LUMO are localized on the donor and acceptor units, respectively, as is the case with ***p*-MC** and **Linear**. At the oxidation potential, two electrons would be removed to generate ***m*-MC**$^{2+\bullet\bullet}$, because the IP (5.51 eV) matched with the theoretically calculated IPs ($^{\mathrm{calc}}$IP1 (radical cation): 5.26 eV, $^{\mathrm{calc}}$IP2 (diradical cation): 5.31 eV), as is the case with ***p*-MC** (Table 13 in the Experimental Section). To investigate the irreversible oxidation, the cycle was repeated at around oxidative potential (Figure 10b). As cycle repeated, the peak current was increased, which implied the occurrence of oxidative polymerization of ***m*-MC** on the electrode. The calculation revealed that spin densities of the diradical dications localized on the *para*-positioned carbons against each nitrogen atom of the donor in ***m*-MC** (Figure 24 in the Experimental Section). This suggested that the electro-polymerization would occur at the donor part.

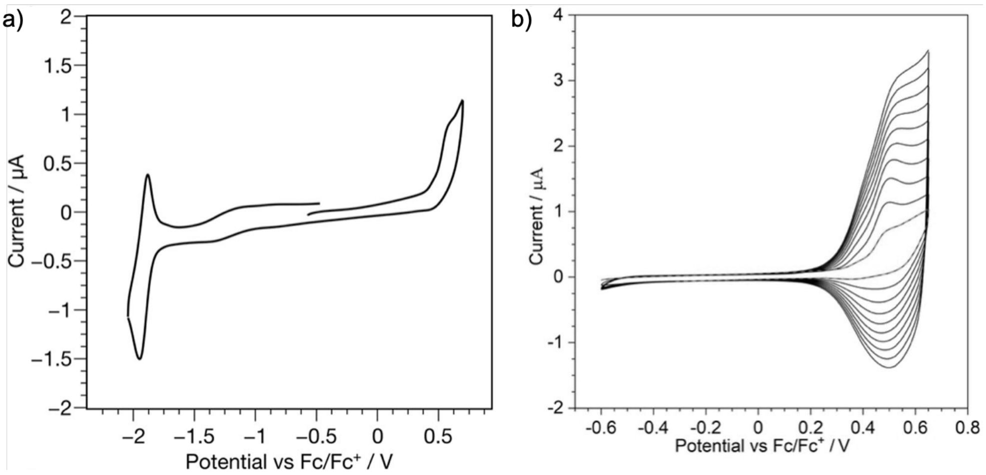

**Figure 10.** a) Cyclic voltammogram and b) sweep-repeated cyclic voltammograms in the positive potential regime of ***m*-MC** ($5\times10^{-4}$ M) in $CH_2Cl_2$ containing 0.1 M *n*-$Bu_4NBF_4$. Electrodes: working (Pt), counter (Pt wire), reference (Ag/AgCl). Scan rate: 50 mV $s^{-1}$. Adapted from ref. 3. Copyright 2020 Wiley-VCH Verlag GmbH.

## 2-4. Summary

In Chapter 2, the structures of the macrocycles (***p*-MC** and ***m*-MC**) were revealed, and the photophysical and electrochemical properties of the macrocycles and the linear compound were investigated. Depending on the condition of recrystallization, ***p*-MC** showed two polymorphs with different emitting colors under the irradiation of UV, which was probably caused by the difference of packing structures. ***m*-MC** showed weak ICT characteristics and electrochemical instability toward oxidation, which are unfavorable as a TADF material. In contrast, the UV-vis absorption and PL spectra of ***p*-MC** and **Linear** are obtained with strong ICT nature, and ***p*-MC** and **Linear** showed reversible redox behavior. Therefore, ***p*-MC** and **Linear** are expected to exhibit efficient TADF.

## 2-5. Experimental Section

### General Remarks.

UV-vis spectra were recorded on a Shimadzu UV-2550 spectrophotometer. Steady-state emission spectra were recorded on a HAMAMATSU C11347-01 spectrometer with an integrating sphere. Cyclic voltammetry was performed with Biologic SP150 system. Spectral measurements were carried out using UV-Vis Hewlett Packard spectrophotometer 8453 for potentiostatic analysis and Ocean Optics QE65000 and NIRQuest 512 for the potentiodynamic process. Spectroelectrochemical investigations were made by connected spectrometers described above with OMNI or AUTOLAB PGSTAT302N+BA potentiostat. EPR analysis was conducted on JEOL JES-FA 200, X-band CW-EPR spectrometer operating at 100 kHz field modulation.

### Materials.

Solvents of fluorescence spectroscopic grade were purchased from Nacalai Tesque Inc. and Kanto Chemical Co., Inc. for measurement of UV-vis and emission spectra. Dichloromethane (CHROMASOLV®, 99.9%) and $n$-$Bu_4NBF_4$ (99%, dried) for CV were purchased from Sigma Aldrich.

### Single Crystal X-ray Crystallographic Data of polymorph *p*-MC-O.

The X-ray diffraction data of the single crystal of polymorph ***p*-MC**-O, which has grown from a $CHCl_3$/*n*-hexane biphasic solution, were collected on a Rigaku XtaLAB P200 diffractometer with graphite monochromated Cu-Kα radiation ($\lambda = 1.54187$ Å) to a $2\theta_{max}$ value of 148.6° at 213 K. The cell refinements were performed with a software CrysAlisPro 1.171.39.20a.[12a] The crystal structure was solved by direct method (SHELXT Version 2014/5).[13a] All calculations were performed with the observed reflections [$I > 2\sigma(I)$] with the program CrystalStructure crystallographic software packages,[14a] except for refinement which was performed by SHELXL.[15a] The non-hydrogen atoms were refined anisotropically, and hydrogen atoms were refined using the riding model. The crystal data are summarized in Table 4. CCDC-1944729 contains the supplementary crystallographic data for polymorph ***p*-MC**-O, which are available free of charge from the Cambridge Crystallographic Data Center (CCDC) via http://www.ccdc.cam.ac.uk/data_request/cif.

### Single Crystal X-ray Crystallographic Data of polymorph *p*-MC-R.

The X-ray diffraction data of the single crystal of polymorph ***p*-MC**-R, which has grown from a $CHCl_3$ solution, were collected on a two dimensional X-ray detector (PILATUS 200K/R) equipped in Rigaku XtaLAB PRO diffractometer using thin multi-layer mirror monochromated Cu-K$\alpha$ radiation ($\lambda$ = 1.54187 Å) to a $2\theta_{\max}$ value of 148.9° at 93 K. The cell refinements were performed with a software CrysAlisPro 1.171.39.20a.[12a] The crystal structure was solved by direct methods (SHELXT Version 2014/5).[13a] All calculations were performed with the observed reflections [I > 2σ(I)] with the program CrystalStructure crystallographic software packages,[14b] except for refinement which was performed by SHELXL.[15b] The non-hydrogen atoms were refined anisotropically, and hydrogen atoms were refined using the riding model. The crystal data are summarized in Table 5. CCDC-1944734 contains the supplementary crystallographic data for polymorph ***p*-MC**-R, which are available free of charge from the Cambridge Crystallographic Data Center (CCDC) via www.ccdc.cam.ac.uk/data_request/cif.

### Single Crystal X-ray Crystallographic Data of polymorph *m*-MC.

The X-ray diffraction data of the single crystal of ***m*-MC**, which has grown from a *o*-dichlorobenzene/*n*-hexane biphasic solution, was collected on a two-dimensional X-ray detector (PILATUS 200K/R) equipped in Rigaku XtaLAB PRO diffractometer using thin multi-layer mirror monochromated Cu-K$\alpha$ radiation ($\lambda$ = 1.54187 Å) to a $2\theta_{\max}$ value of 147.1° at 213 K. The cell refinements were performed with a software CrysAlisPro 1.171.41.79a.[12b] The crystal structure was solved by direct methods (SHELXT 2015).[13b] All calculations were performed with the observed reflections [I > 2σ(I)] with the program Olex$^2$ 1.3 crystallographic software packages,[14c] except for refinement which was performed by SHELXL 2018/3.[15c] The non-hydrogen atoms were refined anisotropically, and hydrogen atoms were refined using the riding model. The crystal data are summarized in Table 6. CCDC-2031432 contains the supplementary crystallographic data for ***m*-MC**, which are available free of charge from the Cambridge Crystallographic Data Center (CCDC) via www.ccdc.cam.ac.uk/data_request/cif.

**Table 4.** Summary of crystallographic data of ***p*-MC**-O.

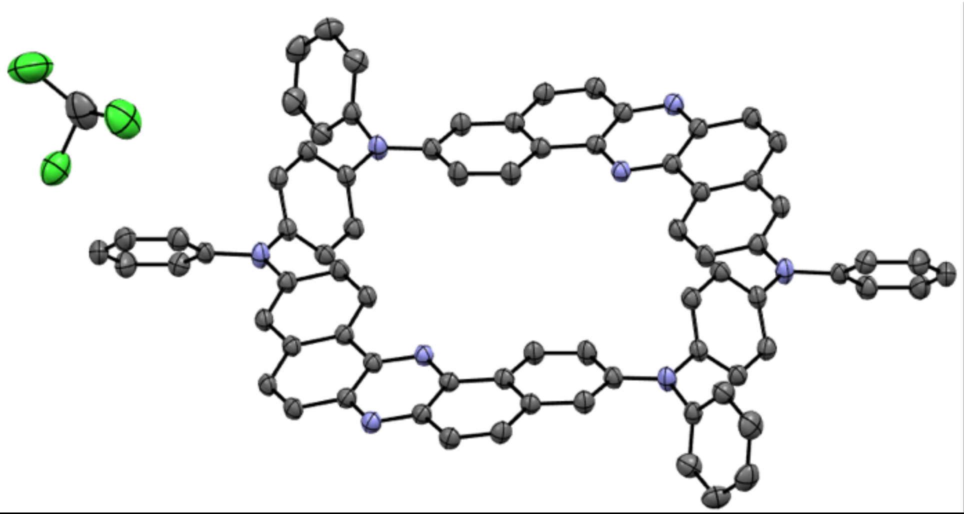

| | | |
|---|---|---|
| Experimental Formula | $C_{78}H_{50}Cl_6N_8$ | |
| Formula Weight | 1312.02 | |
| Crystal System | triclinic | |
| Space Group | *P*-1 (#2) | |
| Unit cell dimensions | $a$ = 11.5979(4) Å | $\alpha$ = 111.577(3)° |
| | $b$ = 12.4849(3) Å | $\beta$ = 107.619(2)° |
| | $c$ = 13.0234(5) Å | $\gamma$ = 103.415(3)° |
| $V$ | 1538.21(12) Å$^3$ | |
| $Z$ | 1 | |
| Density (calculated) | 1.4616 g/cm$^3$ | |
| Absorption coefficient | 29.822 cm$^{-1}$ | |
| $R_1$ [I>2$\sigma$(I)] | 0.0661 | |
| $wR_2$ (all data) | 0.1954 | |
| Crystal size | 0.300 × 0.300 × 0.200 mm | |
| Goodness-of-fit on $F^2$ | 1.077 | |
| Reflections collected/unique | 15339/6028 [$R$(int)= 0.0267] | |

**Table 5.** Summary of crystallographic data of ***p*-MC**-R.

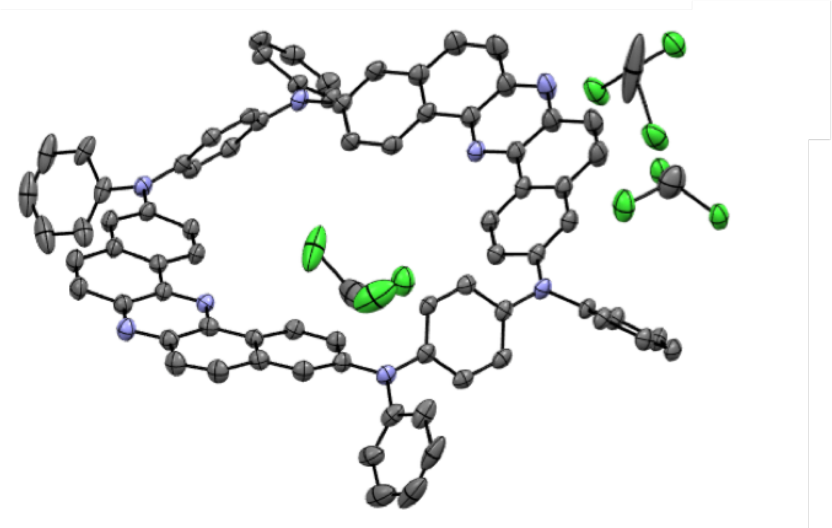

| | | |
|---|---|---|
| Experimental Formula | $C_{83}H_{55}Cl_{17}N_{10}$ | |
| Formula Weight | 1795.12 | |
| Crystal System | monoclinic | |
| Space Group | $P2_1/m$ (#11) | |
| Unit cell dimensions | $a$ = 8.76533(10) Å | $\alpha$ = 90° |
| | $b$ = 40.6863(4) Å | $\beta$ = 98.1999(10)° |
| | $c$ = 21.4744(2) Å | $\gamma$ = 90° |
| $V$ | 7580.09(14) Å$^3$ | |
| $Z$ | 4 | |
| Density (calculated) | 1.573 g/cm$^3$ | |
| Absorption coefficient | 60.848 cm$^{-1}$ | |
| $R_1$ [I>2$\sigma$(I)] | 0.1104 | |
| $wR_2$ (all data) | 0.3273 | |
| Crystal size | 0.100 × 0.050 × 0.050 mm | |
| Goodness-of-fit on $F^2$ | 1.043 | |
| Reflections collected/unique | 48472/15366 [$R$(int)= 0.0438] | |

**Table 6.** Summary of crystallographic data of ***m*-MC**.

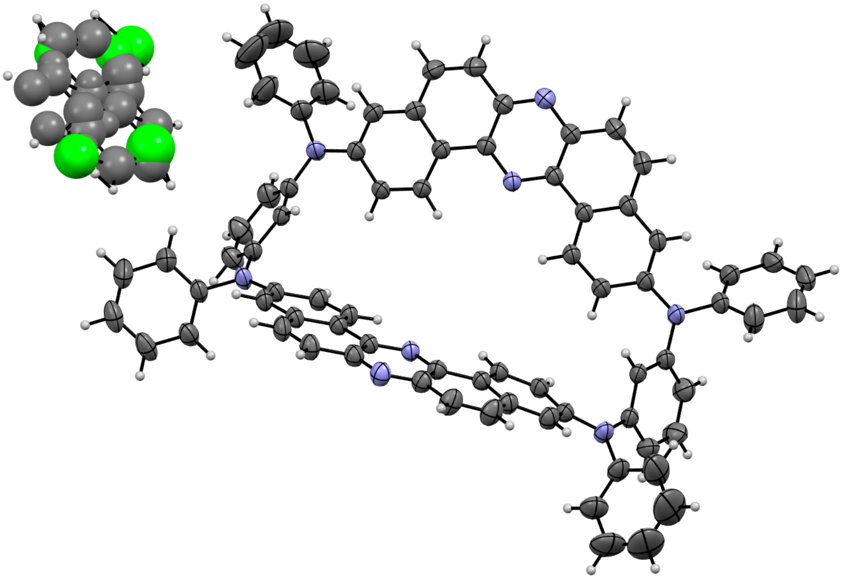

| | | |
|---|---|---|
| Experimental Formula | $C_{82}H_{52}Cl_2N_8$ | |
| Formula Weight | 1312.02 | |
| Crystal System | monoclinic | |
| Space Group | *I*2/*a* (#15) | |
| Unit cell dimensions | $a$ = 16.2134(3) Å | $\alpha$ = 90° |
| | $b$ = 10.0872(2) Å | $\beta$ = 90.409 (2)° |
| | $c$ = 38.3409(6) Å | $\gamma$ = 90° |
| $V$ | 6270.4(2) Å$^3$ | |
| $Z$ | 4 | |
| Density (calculated) | 1.293 g/cm$^3$ | |
| Absorption coefficient | 13.57 cm$^{-1}$ | |
| $R_1$ [I>2$\sigma$(I)] | 0.0668 | |
| $wR_2$ (all data) | 0.2159 | |
| Crystal size | 0.150 × 0.100 × 0.030 mm | |
| Goodness-of-fit on $F^2$ | 1.054 | |
| Reflections collected/unique | 6341/4771 [$R$(int)= 0.0833] | |

### Steady-state UV-vis Absorption and PL Spectra.

All the steady-state UV-vis absorption and PL spectra were measured at room temperature with crystals and diluted solutions ($10^{-6}$–$10^{-5}$ M), which were prepared from degassed spectroscopic grade solvents ($N_2$ for 30 min).

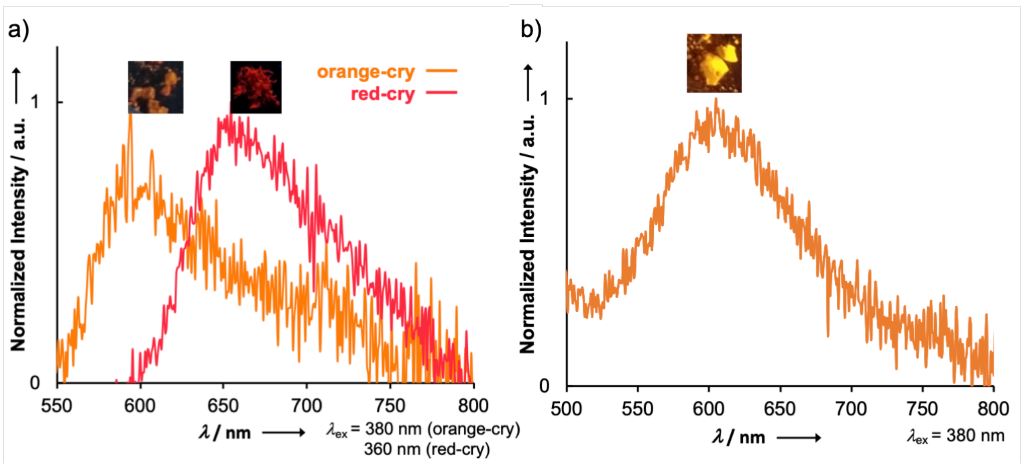

**Figure 11.** PL spectra of (a) polymorph ***p*-MC**-O and polymorph ***p*-MC**-R and (b) solid of **Linear**. Reproduced from ref. 2. Copyright 2020 American Chemical Society.

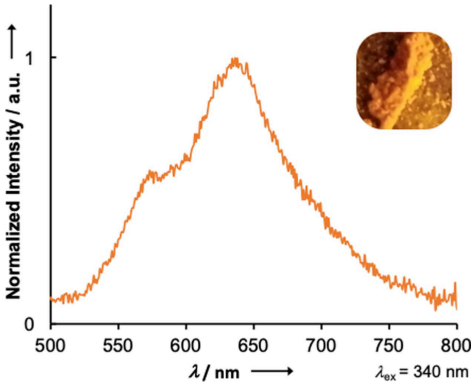

**Figure 12.** PL spectrum of ***m*-MC** in the solid states. Reproduced from ref. 3. Copyright 2020 Wiley-VCH Verlag GmbH.

### Cyclic Voltammetry.

CV experiments were conducted at room temperature using dichloromethane solutions of ***p*-MC**, **Linear**, ***m*-MC**, and ***t*-Bu-MC** (concentration: $5.0\times10^{-4}$ M for ***p*-MC**, $1.0\times10^{-3}$ M for **Linear**, $5.0\times10^{-4}$ M for ***m*-MC**, and $2.5\times10^{-4}$ M for ***t*-Bu-MC**) containing 0.1 M *n*-$Bu_4NBF_4$ as a supporting electrolyte. Solutions were purged with argon before measurements. Electrodes: working (Pt disc 1 mm of diameter), counter (Pt wire), reference (Ag/AgCl calibrated against ferrocene). Scan rate: 50 $mVs^{-1}$. Ionization potential (IP) and electron affinity (EA) were calculated from oxidation ($E^{\text{ox1}}$) and reduction ($E^{\text{red}}$) potentials, respectively, using following equations: IP = $E^{\text{ox1}}$ + 5.1, EA = $E^{\text{red}}$ + 5.1.[16]

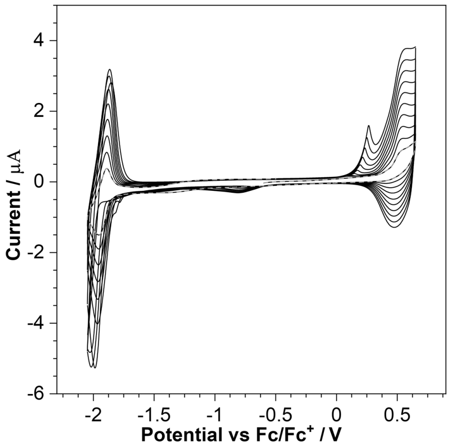

**Figure 13.** Multicycle cyclic voltammograms in wide potential range of ***m*-MC** ($5\times10^{-4}$ M) in $CH_2Cl_2$ containing 0.1 M *n*-$Bu_4NBF_4$. Electrodes: working (Pt), counter (Pt wire), reference (Ag/AgCl). Scan rate: 50 mV $s^{-1}$. Reproduced from ref. 3. Copyright 2020 Wiley-VCH Verlag GmbH.

***t*-Bu-MC** showed a reversible one-step reduction (${}^{\text{red}}E_{1/2}$ = –1.89 V vs Fc/Fc$^+$), as is the case with ***p*-MC**. On the other hands, ***t*-Bu-MC** showed two-step oxidation process, and the first redox couple of ***t*-Bu-MC** (${}^{\text{ox1}}E_{1/2}$ = +0.23 V vs Fc/Fc$^+$) is reversible, but the second one (${}^{\text{ox2}}E_{1/2}$ = +0.63 V vs Fc/Fc$^+$) is quasi-reversible with an untypically high peak current (Figure 14). It should be noted that the peak current of the second oxidation process decreased as the redox cycle repeated. Although the second oxidation process of ***t*-Bu-MC** is quasi-reversible, no additional peak relating to the formation of by-products through the redox process was detected. Additionally, the other part of the CV was not affected by repeated potential sweep. Given these behaviors, the decrease of the current peak would not result from the deposition of low conducting material on the electrode and the chemical degradation of ***t*-Bu-MC**. Also, the introduction of *t*-Bu groups has significant influences on the second oxidation process as already mentioned above. The ionization potential/electron affinity of ***t*-Bu-MC** determined by the CV experiment are 5.33 eV/3.21 eV. The ${}^{\text{ox1}}E_{1/2}$ potentials (vs Fc/Fc$^+$) of ***t*-Bu-MC** is negatively sifted compared to ***p*-MC**, which would be caused by the four σ-donating alkyl (*t*-Bu) groups introduced at *p*-position of the external aromatic rings on the donors.

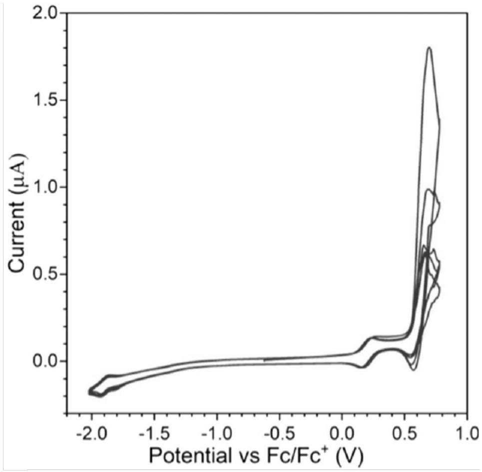

**Figure 14.** Cyclic voltammograms of ***t*-Bu-MC** ($2.5\times10^{-4}$ M) in $CH_2Cl_2$ containing 0.1 M *n*-$Bu_4NBF_4$. Electrodes: working (Pt), counter (Pt wire), and reference (Ag/AgCl). Scan rate: 50 mV $s^{-1}$. Reproduced from ref. 17. Copyright 2020 Wiley-VCH Verlag GmbH.

**Theoretical Calculations.**

The conformers of ***p*-MC** (**helical** and **saddle** conformers) were optimized at the DFT level using the B3LYP exchange-correlation functional and the cc-pVDZ basis set. The calculations were performed using Q-Chem 5.0 simulations package.[18] The structures acquired from the X-ray crystallographic analyses (see Table 4 and 5) were used as the initial guesses for geometry optimization. The energies of both optimized conformers in the toluene solution were calculated with several exchange-correlation functionals. This included an optimally tuned range-separated hybrid functional ω*PBE with the optimal parameter $\omega = 0.152$ bohr$^{-1}$. To model the effect of solvation, a continuum solvation model (C-PCM) was used with the toluene's dielectric constant $\varepsilon = 2.38$. To check the importance of intramolecular dispersion interaction for the structure and energetics of ***p*-MC**, the conformers were additionally optimized with the ωB97X-D functional. The calculated energies of ***p*-MC** in toluene solution are shown in Table 7.

**Table 7.** Summary of conformational energy differences in **helical** and **saddle** in toluene.

| | Exchange-correlation functional | | | | |
|---|---|---|---|---|---|
| | B3LYP | M06-2X | CAM-B3LYP | ωB97X-D | ω*PBE |
| **helical** (Hartree) | -3363.3281 | -3362.1770 | -3361.4515 | -3362.2086 | -3340.6949 |
| **saddle** (Hartree) | -3363.3366 | -3362.1842 | -3361.4590 | -3362.2167 | -3340.7031 |
| Energy difference (kcal/mol) | 5.39 | 4.58 | 4.73 | 5.10 | 5.19 |

The singlet and triplet vertical excitation energies at the ground state geometry were calculated with TD-DFT using the optimally tuned ω*PBE functional, which has a good balance in the description of CT and LE excitations. To account for the effect of the environment, and to compare the calculations directly to the measured absorption spectrum, a state-specific non-equilibrium C-PCM solvent model with the equilibrium dielectric constant $\varepsilon = 2.38$ and the high-frequency dielectric constant $\varepsilon_\infty = 2.24$, corresponding to toluene as the solvent was used. The results of TD-DFT calculations are summarized in Table 8 and 9. Predicted UV-vis absorption spectra of **helical** and **saddle** are illustrated in Figure 15. The spectra are plotted as vertical excitation energies of 100 lowest singlet states with a Gaussian broadening of 0.22 eV.

**Table 8.** Summary of TD-DFT calculations of **helical**.[a]

| | singlet | triplet |
|---|---|---|
| *excitation energy* [eV] (*f*) | 2.6893 (0.0000) | 2.1410 (0.0000) |
| *transition mode* | H→L (58%) | |
| | H–2→L+1 (29%) | |
| *excitation energy* [eV] (*f*) | 2.7746 (0.8605) | 2.1497 (0.0000) |
| *transition mode* | H→L+1 (51%) | |
| | H–2→L (32%) | |
| *excitation energy* [eV] (*f*) | 2.9105 (0.0462) | 2.2610 (0.0000) |
| *transition mode* | H–1→L (61%) | H→L (43%) |
| | H–3→L+1 (28%) | H–2→L+1 (37%) |
| *excitation energy* [eV] (*f*) | 2.9382 (0.0000) | 2.2694 (0.0000) |
| *transition mode* | H–1→L+1 (57%) | H→L+1 (41%) |
| | H–3→L (31%) | H–2→L (37%) |
| *excitation energy* [eV] (*f*) | 3.0968 (0.0000) | 2.6149 (0.0000) |
| *transition mode* | H–8→L (47%) | H–8→L (41%) |
| | H–7→L+1 (31%) | H–7→L+1 (32%) |

[a] The percentages of orbital transitions are shown in parentheses (only > 25% are shown).

**Table 9.** Summary of TD-DFT calculations of **saddle**.[a]

| | singlet | triplet |
|---|---|---|
| *excitation energy* [eV] (*f*) | 2.6071 (0.0000) | 2.1065 (0.0000) |
| *transition mode* | H→L (63%) | |
| *excitation energy* [eV] (*f*) | 2.6962 (0.8176) | 2.1236 (0.0000) |
| *transition mode* | H→L+1 (60%) | |
| *excitation energy* [eV] (*f*) | 2.7702 (0.0658) | 2.2734 (0.0000) |
| *transition mode* | H–1→L (69%) | H→L (44%)<br>H–2→L+1 (29%) |
| *excitation energy* [eV] (*f*) | 2.8071 (0.0002) | 2.2889 (0.0000) |
| *transition mode* | H–1→L+1 (66%) | H→L+1 (41%)<br>H–2→L (32%) |
| *excitation energy* [eV] (*f*) | 3.0771 (0.0062) | 2.5868 (0.0000) |
| *transition mode* | H–8→L (48%)<br>H–9→L+1 (47%) | H–9→L (46%)<br>H–8→L+1 (45%) |

[a]The percentages of orbital transitions are shown in parentheses (only > 25% are shown).

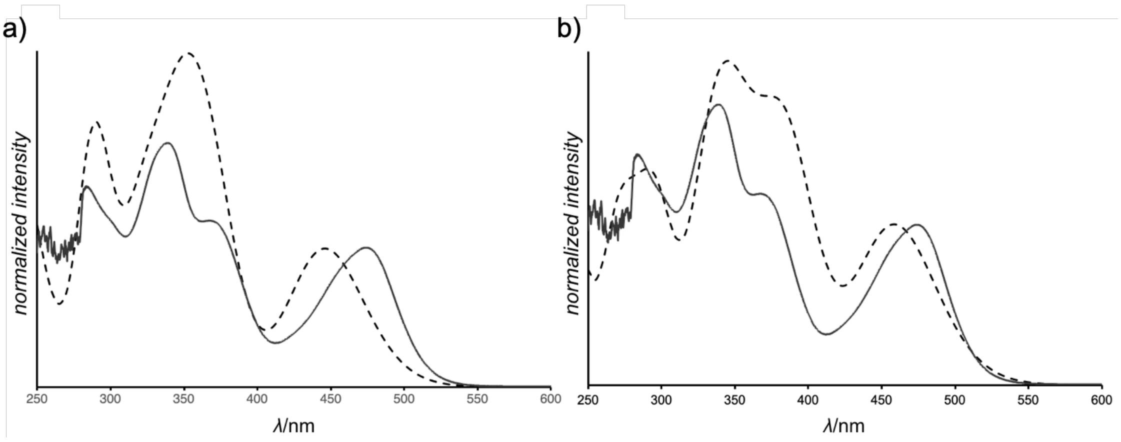

**Figure 15.** Comparison of the experimental UV-vis absorption spectra of toluene solution of ***p*-MC** (in solid black lines) and predicted spectra of (a) **helical** and (b) **saddle** conformer of ***p*-MC** in toluene (in black doted lines). Each spectrum was normalized at the intensity of the lowest energy absorption maxima. Adapted from ref. 2. Copyright 2020 American Chemical Society.

For the **Linear**, a conformational search with a UFF force field was performed using the ADF computational package.[19] Subsequently, TD-DFT calculations were done for 10 conformers with the lowest energies. The parameters for TD-DFT calculations were the same as for ***p*-MC**. No qualitative differences in the excitation energies were found for these conformers, so the summary of results is presented only for the energetically lowest conformer in Table 10. The predicted UV-vis absorption spectrum is shown in Figure 16.

**Table 10.** Summary of TD-DFT calculations of **Linear**.[a]

| | singlet | triplet |
|---|---|---|
| *excitation energy* [eV] (*f*) | 2.5545 (0.2821) | 2.1104 (0.0000) |
| *transition mode* | H–1→L (43%) | |
| *excitation energy* [eV] (*f*) | 2.5708 (0.9494) | 2.1391 (0.0000) |
| *transition mode* | H→L+1 (47%) | |
| *excitation energy* [eV] (*f*) | 2.6540 (0.0050) | 2.2281 (0.0000) |
| *transition mode* | H–1→L+1 (64%) | H→L+1 (41%) |
| *excitation energy* [eV] (*f*) | 3.0390 (0.0025) | 2.3818 (0.0000) |
| *transition mode* | H–9→L (91%) | H–4→L (44%) |
| *excitation energy* [eV] (*f*) | 3.0464 (0.0039) | 2.5593 (0.0000) |
| *transition mode* | H–8→L+1 (88%) | H–9→L (87%) |

[a]The percentages of orbital transitions are shown in parentheses (only > 25% are shown).

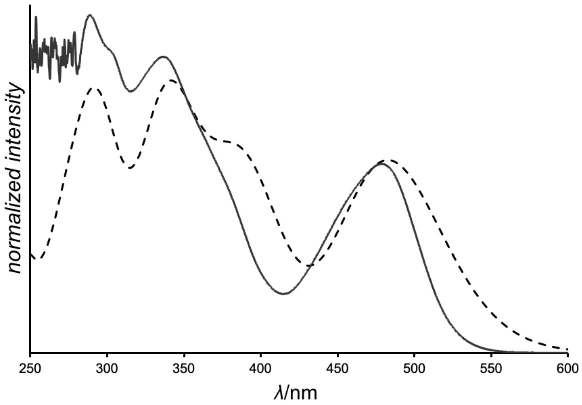

**Figure 16.** Comparison of the experimental UV-vis absorption spectrum of toluene solution of **Linear** (in solid black line) and predicted spectrum of the most energetically stable conformer of **Linear** in toluene (in black doted lines). Both spectra were normalized at the intensity of the lowest energy absorption maxima. Adapted from ref. 2. Copyright 2020 American Chemical Society.

To find the most stable conformer of ***m*-MC**, a conformational search at force field level using the conformer search module in the ADF package were conducted.[20] For the selected distinct structures found in the search, the geometries were optimized by the DFT level (PBE0/cc-pVDZ) using Q-Chem package.[18] The study revealed that using the geometry from the crystal structure leads to the most stable saddle conformer as is the case with ***p*-MC**. The most stable conformer is over 4 kcal/mol lower in energy than the next conformer type. The comparison of saddle conformations for ***m*-MC** and ***p*-MC** is shown in Figure 17.

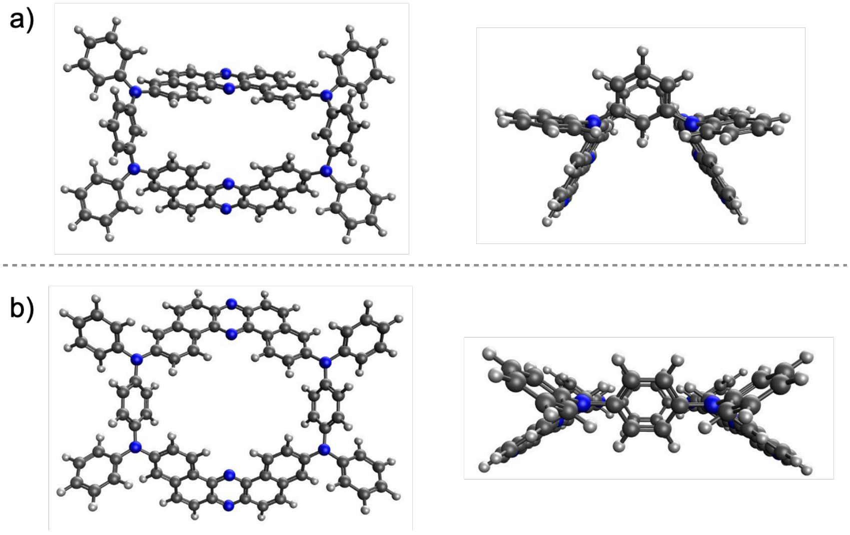

**Figure 17.** The most stable conformers of (a) ***m*-MC** and (b) ***p*-MC**. Geometries optimized at the PBE0/ccpVDZ level of theory. Adapted from ref. 3. Copyright 2020 Wiley-VCH Verlag GmbH.

For the most stable conformers, TD-DFT calculations were done using the optimally tuned ωPBE functional and a state-specific non-equilibrium PCM solvation model corresponding to the toluene solvent. The results of TD-DFT calculations are summarized in Table 11. The predicted UV-vis absorption spectrum is shown in Figure 18. The spectra for ***m*-MC** and ***p*-MC** qualitatively agree with the experiments. In particular, the blue shift of the bands in ***m*-MC** is well captured. The transition to the first singlet excited state ($S_1$) is forbidden due to the molecules' symmetry, and the lowest-lying bright state is $S_2$. The HOMO and LUMO frontier orbitals, which participate in $S_1$ and $S_2$ transitions, are plotted in Figure 19.

**Table 11.** Summary of the TD-DFT calculations for ***m*-MC**. 10 lowest singlet and triplet transitions are included.[a]

| | singlet | triplet |
|---|---|---|
| *excitation energy* [eV] (*f*) | 2.79 (0.0000) | 2.42 (0.0000) |
| *transition mode* | H→L (50%) | |
| | H–2→L+1 (32%) | |
| *excitation energy* [eV] (*f*) | 2.87 (1.0448) | 2.42 (0.0000) |
| *transition mode* | H→L+1 (43%) | |
| | H–2→L+1 (35%) | |
| *excitation energy* [eV] (*f*) | 3.07 (0.0071) | 2.43 (0.0000) |
| *transition mode* | H–1→L (37%) | H→L (28%) |
| | | H–2→L+1 (25%) |
| *excitation energy* [eV] (*f*) | 3.15 (0.0053) | 2.44 (0.0000) |
| *transition mode* | H–9→L (35%) | |
| | H–8→L+1 (34%) | |
| *excitation energy* [eV] (*f*) | 3.15 (0.0034) | 2.68 (0.0000) |
| *transition mode* | H–1→L+1 (32%) | H–9→L+1 (46%) |
| | H–3→L (28%) | H-8→L (47%) |
| *excitation energy* [eV] (*f*) | 3.18 (0.0113) | 2.68 (0.0000) |
| *transition mode* | H–8→L (35%) | H–9→L (46%) |
| | H–9→L+1 (34%) | H–8→L+1 (46%) |
| *excitation energy* [eV] (*f*) | 3.36 (0.0001) | 2.86 (0.0000) |
| *transition mode* | H–3→L+2 (36%) | H→L+3 (25%) |
| | H–1→L+3 (28%) | |
| *excitation energy* [eV] (*f*) | 3.40 (0.0034) | 2.86 (0.0000) |
| *transition mode* | | |
| *excitation energy* [eV] (*f*) | 3.40 (1.2041) | 2.93 (0.0000) |
| *transition mode* | H–1→L+2 (34%) | |
| *excitation energy* [eV] (*f*) | 3.42 (0.0085) | 2.97 (0.0000) |
| *transition mode* | H→L+2 (32%) | H–9→L (46%) |
| | | H–8→L+1 (45%) |

[a] The percentages of orbital transitions are shown in parentheses (only > 25% are shown).

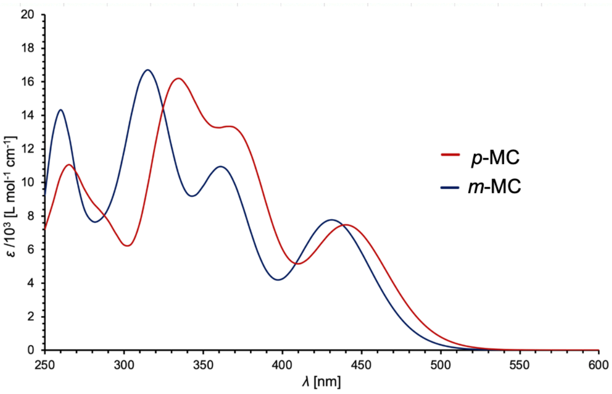

**Figure 18.** Calculated absorption spectra of ***m*-MC** and ***p*-MC** in toluene solvent. Reproduced from ref. 3. Copyright 2020 Wiley-VCH Verlag GmbH.

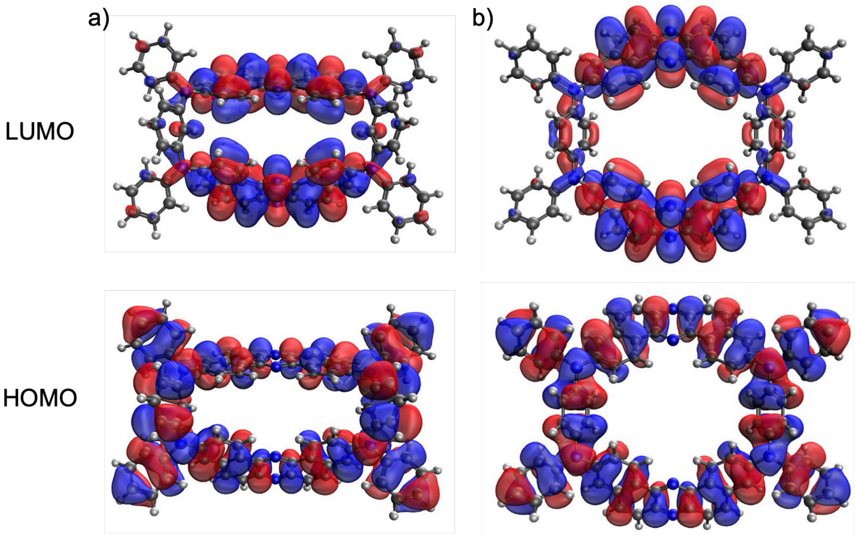

**Figure 19.** HOMO (bottom) and LUMO (top) orbitals of (a) ***m*-MC** and (b) ***p*-MC**. Adapted from ref. 3. Copyright 2020 Wiley-VCH Verlag GmbH.

To better visualize the character of the excited states, in Figure 20 the Natural Transition Orbitals (NTOs) with the highest eigenvalue for the lowest-lying triplet ($T_1$) and singlet ($S_1$) states were plotted. The NTOs for $S_2$ and $S_9$ states, which are the bright states responsible for the intensities of the first two bands in the calculated spectra, were also plotted. Due to the symmetry of the macrocycles, the canonical orbitals and NTOs are largely delocalized over the entire macrocycle. Nevertheless, the CT character of the $S_1$ and $S_2$ states is evident, as the hole has a large amplitude on the donors, while the electron is much more localized on the acceptors only. It is expected that molecular vibrations would break the symmetry and localize the states further, leading to much stronger CT character that would be stabilized in the excited state by the solvent. The transitions responsible for the second band in the absorption spectrum are local excitations, confirming the π–π* assignment.

| | | ***m*-MC** | ***p*-MC** |
|---|---|---|---|
| $T_1$ | hole | 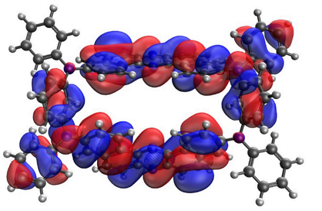 | 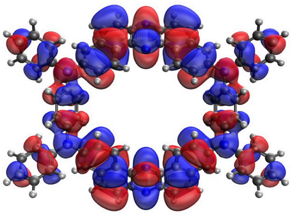 |
| | electron | 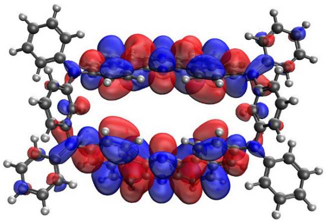 | 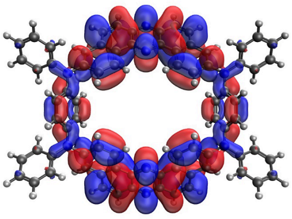 |
| $S_1$ | hole | 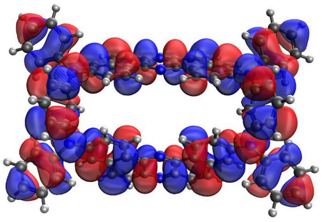 | 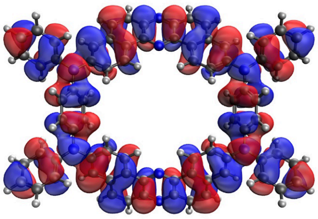 |
| | electron | 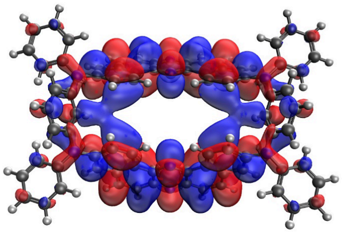 | 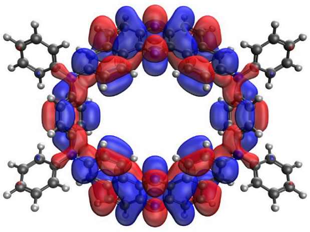 |
| $S_2$ | hole | 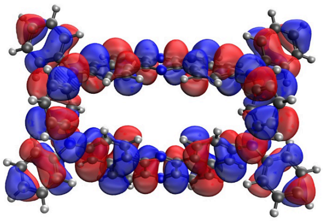 | 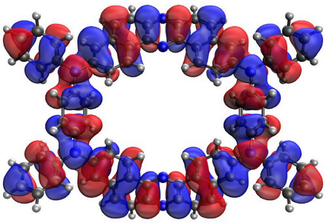 |
| | electron | 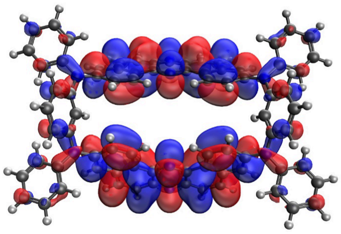 | 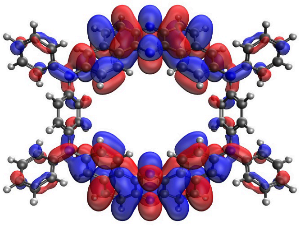 |

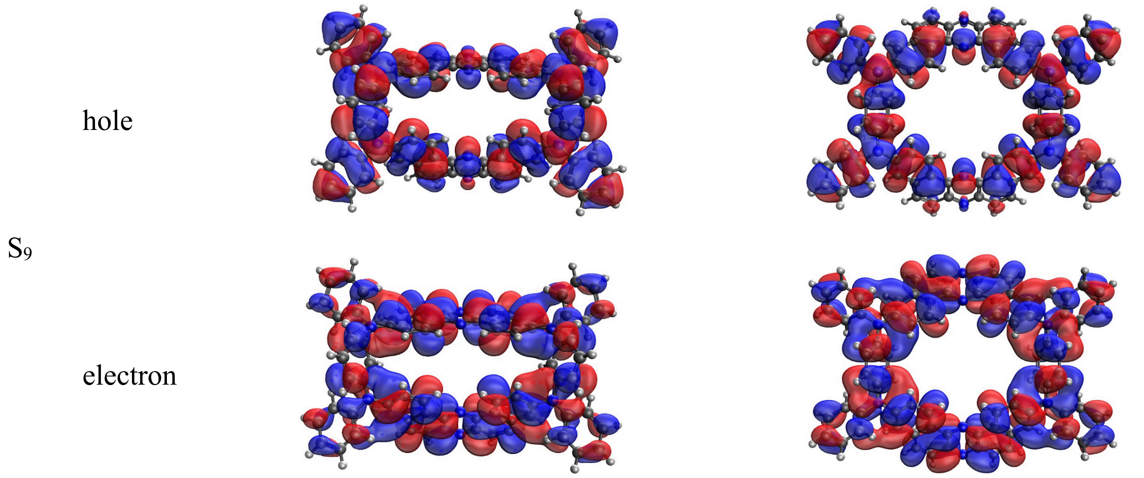

**Figure 20.** The dominant NTOs for $T_1$, $S_1$, $S_2$, and $S_9$ states of ***m*-MC** (left) and ***p*-MC** (right). For each NTO pair, hole NTO is at the top and electron NTO in the bottom. Adapted from ref. 3. Copyright 2020 Wiley-VCH Verlag GmbH.

To obtain insights about the charged species of ***p*-MC**, ***t*-Bu-MC**, and **Linear**, the calculations were done using the ADF modelling package. The geometries of neutral and charged species were optimized at the PBE0/DZP level. For **Linear**, one conformation was found to be the most stable in a conformation search with an UFF as implemented in ADF. For ***t*-BuMC**, the **saddle** conformation was more stable than the **helical** conformer as seen in the study of ***p*-MC**. For the multiply charged species, calculations for the low- and high-spin states were conducted to predict which are more thermodynamically stable. The IPs and EA were calculated at the PBE0/TZP level (Table 12) using COSMO implicit solvation model. The calculations revealed that both cations and open-shell dications are formed in the first oxidation wave while radical trication and closed-shell tetracation in the second. For the calculations of absorption spectra, the M06-2X functional was used, because an increased amount of exact exchange (relative to PBE0) is needed to capture qualitatively the excited state with CT character. Excitation energies were calculated using TD-DFT formalism with Tamm-Dancoff approximation and with non-equilibrium COSMO solvation model. Predicted absorption spectra for the most stable species of each charge are illustrated in Figures 21–23.

**Table 12.** Calculated electron removal/addition energies to form charged species in low- and high-spin states (PBE0/TZP + COSMO) and measured ionization potentials.

| | ***p*-MC** | **Linear** | ***t*-Bu-MC** |
|---|---|---|---|
| EA (radical amion) | 2.69 eV | 2.68 eV | 2.66 eV |
| IP (measured) | 5.37 eV | 5.32 eV | 5.33 eV |
| IP (radical cation) | 5.10 eV | 5.00 eV | 5.02 eV |
| IP2 (diradical dication) | 5.03 eV | 5.00 eV | 4.96 eV |
| IP2 (closed-shell dication) | 5.61 eV | 5.64 eV | 5.53 eV |
| IP3 (triradical trication) | 6.45 eV | 6.42 eV | 6.36 eV |
| IP3 (radical trication) | 6.17 eV | 6.10 eV | 6.09 eV |
| IP4 (tetraradical tetracation) | 6.50 eV | 6.61 eV | 6.34 eV |
| IP4 (closed-shell tetracation) | 6.20 eV | 6.20 eV | 6.12 eV |

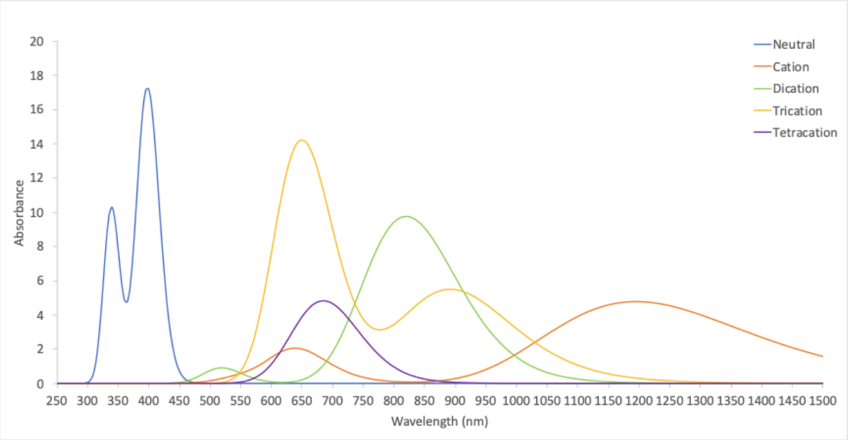

**Figure 21.** The calculated absorption spectrum of ***p*-MC** in different oxidation states (M06-2X/TZP + COSMO calculations). Reproduced from ref. 17. Copyright 2020 Wiley-VCH Verlag GmbH.

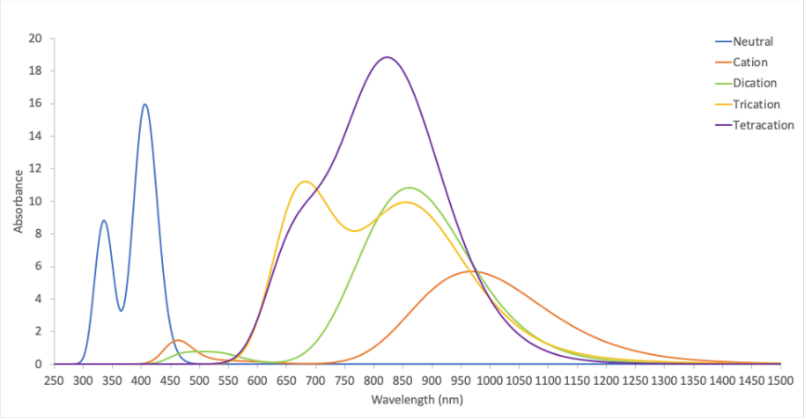

**Figure 22.** The calculated absorption spectrum of **Linear** in different oxidation states (M06-2X/TZP + COSMO calculations). Reproduced from ref. 17. Copyright 2020 Wiley-VCH Verlag GmbH.

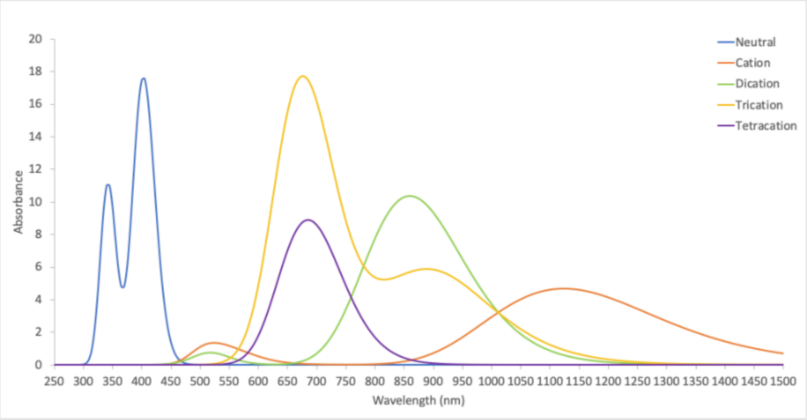

**Figure 23.** The calculated absorption spectrum of ***t*-Bu-MC** in different oxidation states (M06-2X/TZP + COSMO calculations). Reproduced from ref. 17. Copyright 2020 Wiley-VCH Verlag GmbH.

For ***m*-MC**, calculations for the charged species, done at the PBE0/aug-cc-pVDZ level, confirm that the oxidation wave in the CV is a 2-electron process as the first and second ionization potentials of ***m*-MC** are very close to each other. The corresponding potential is also within 0.3 V from the experimental value. The results of calculations for charged species of ***m*-MC** and ***p*-MC** are collected in Table 13 and the spin densities of diradical dications are plotted in Figure 24.

**Table 13.** Ionization potentials and electron affinities of ***p*-MC** and ***m*-MC** calculated at PBE0/aug-cc-pVDZ level.

| | ***p*-MC** | ***m*-MC** |
|---|---|---|
| EA (radical anion) | 2.66 eV | 2.66 eV |
| IP (radical cation) | 5.02 eV | 5.26 eV |
| IP2 (diradical dication) | 4.95 eV | 5.31 eV |

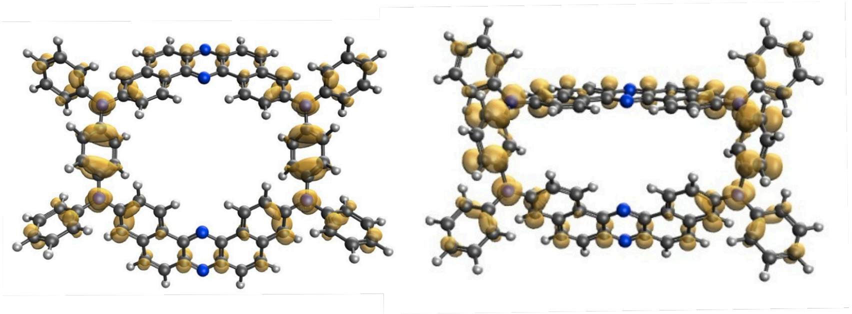

**Figure 24.** Spin densities of diradical dications of ***p*-MC** (left) and ***m*-MC** (right). Adapted from ref. 3. Copyright 2020 Wiley-VCH Verlag GmbH.

**Potentiostatic UV-Vis-NIR spectroelectrochemistry analysis.**

UV-Vis-NIR spectroelectrochemical studies, were performed using dichloromethane solutions of ***p*-MC**, **Linear**, and ***t*-Bu-MC** (concentration: $5.0\times10^{-4}$ M for ***p*-MC**, $5.0\times10^{-4}$ M for **Linear**, and $2.5\times10^{-4}$ M for ***t*-Bu-MC**) containing 0.1 M $n$-$Bu_4NBF_4$ as a supporting electrolyte. UV-Vis measurements were carried out in a thin layer spectroelectrochemical cell, which was a modification of cells described in the previous literature.[21] An ITO electrode was used as a working electrode, platinum spiral as an auxiliary electrode, and silver wire as a pseudo-reference electrode.

Spectroelectrochemical analysis of ***p*-MC**, **Linear**, and ***t*-Bu-MC** reveals that new vibronic bands between 500–800 nm (denoted as B1) and 800–1100 nm (denoted as B2) gradually arise by electrochemical oxidation of neutral species (Figure 25). Although all cases look similar at the first glance, there are significant differences between them. After the application of the potential to neutral ***p*-MC** up to 0.50 V, the bands connected to the neutral species (250–550 nm, Figure 25a) significantly increased, and the B1 slightly arises. Subsequently, the rise of B2 was observed (Figure 25a). B2 band corresponds to an intervalence charge-transfer (IV-CT) absorption band, which is commonly observed for radical cation species of *N*,*N*,*N*’,*N*’-tetraaryl-*p*-phenylenediamine derivatives (TPDA).[22] As mentioned in the CV section, the comparison of the calculated and experimental IPs revealed that two electrons are removed from ***p*-MC** at almost the same voltage. Given that IV-CT bands were not shifted through the first oxidation, one electron was removed from each donor (two electrons in total) to form open-shelled semiquinone diradical dication species through the 1st oxidation step. This behavior shows good agreement with the report on oxidation of macrocyclic oligoarylamines.[23] Above the 0.50 V, another IV–CT band (B1) was rapidly increased, and IV-CT band (B2) was decreased. This should correspond to the second oxidation process of the ***p*-MC** (Figure 25a). According to literature, the oxidation of the radical cation of TPDA leads to the rise of absorption at around 598 nm, which indicates the generation of open-shelled diradical dication.[5] Considering that ***p*-MC** shows a similar behavior, two electrons would be removed concomitantly from the diradical dication species to generate monoradical trication and closedshell tetracation species.

The spectroelectrochemical behavior of **Linear** is much similar to those observed with TPDA and its derivatives rather than that of ***p*-MC**. A couple of absorption bands assigned to the neutral species of **Linear** gradually decreased, and the rise of the IV-CT bands (B2) and (B1) was observed sequentially, showing isosbestic points (Figure 25c). This suggests that the oxidation process of **Linear** is in sequential order. In contrast, ***t*-Bu-MC** showed oxidation process like the mixture behaviors observed in ***p*-MC** and **Linear** (Figure 25b). Through the oxidation, new bands in the range of neutral form appeared, and then up to 0.40 V, IV-CT band (B2) arose. After passing the first oxidation potential, B1 was significantly increased, accompanying the decrease of B2 band. The simulation of the absorption spectra by calculation (Figure 21–23) shows that there is no new band forming between 250 nm and 450 nm, and therefore the rise of the neutral band probably was caused by the diffusion of neutral species and the increase of the concentration of the compound in the double layer between the solution and the electrode. As regards the difference between the ***p*-MC** and ***t*-Bu-MC** in the first oxidation, the absence of new band (600–700 nm) is clarified by theoretical calculation (Figures 21 and 22), where the cation absorption of ***p*-MC** is observed between 550–750 nm and that of ***t*-Bu-MC** is hypsochromically shifted and located between 450–600 nm (Figure 23).

The calculated spectra with TD-DFT (Figure 21–23) corroborate this analysis, as mentioned above paragraph. The B2 band corresponds to the presence of monocationic species. While the calculated band for ***p*-MC** and ***t*-Bu-MC** is red-shifted to 1100–1200 nm, that of **Linear** shows much greater agreement with the experiment. The B1 band coincided with the presence of trications and tetracations and is predicted to be between the B2 and neutral bands, in agreement with the experiment.

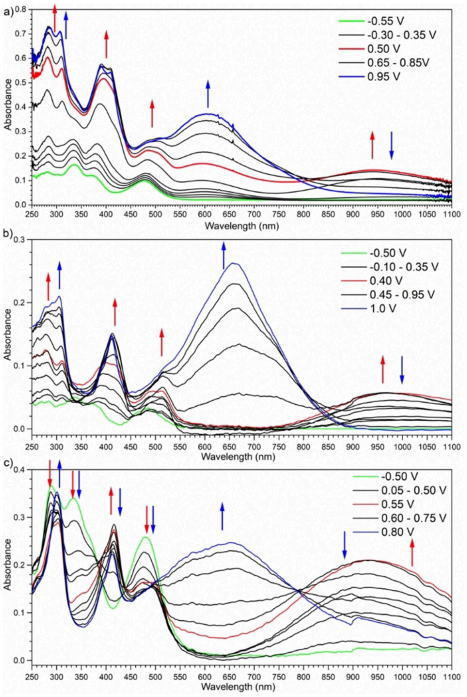

**Figure 25.** Potentiostatic UV-Vis-NIR spectroelectrochemistry of (a) ***p*-MC** ($5\times10^{-4}$ M), (b) ***t*-Bu-MC** ($2.5\times10^{-4}$ M), and (c) **Linear** ($5\times10^{-4}$ M) in $CH_2Cl_2$ containing 0.1 M *n*-$Bu_4NBF_4$. Reproduced from ref. 17. Copyright 2020 Wiley-VCH Verlag GmbH.

**Electron Paramagnetic Resonance analysis.**

Electron paramagnetic resonance (EPR) spectroelectrochemical studies, were performed using dichloromethane solutions of ***p*-MC**, **Linear**, and ***t*-Bu-MC** (concentration: $5.0\times10^{-4}$ M for ***p*-MC**, $5.0\times10^{-4}$ M for **Linear**, and $2.5\times10^{-4}$ M for ***t*-Bu-MC**) containing 0.1 M $n$-$Bu_4NBF_4$ as a supporting electrolyte. EPR measurements were carried out in a cylindrical cell equipped with a platinum wire as a working, platinum spiral as an auxiliary, and silver wire as a pseudo-reference electrode. The spectra of the radical anions were recorded during potentiostatic reduction of ***p*-MC** and **Linear**, and ***t*-Bu-MC**. The standard based on $Mn^{2+}$ was used for *g*-factor calibration. To calculate *g*-factor, the spectra of $Mn^{2+}$ (the third and fourth line) together with investigated sample were measured. The *g*-factor of the investigated sample was calculated based on known values of *g*-factors corresponding to 3rd and 4th lines of $Mn^{2+}$ spectrum (2.03277 for 3rd and 1.98104 for 4th spectral line). All of the investigations were conducted on the solutions purged with argon.

To obtain information on the species generated in the electrochemical reactions, EPR spectroelectrochemical measurements were conducted (Figure 26a–c). In the case of ***p*-MC**, the application of the potential of 0.3 V (vs. the $Fc/Fc^+$ redox couple) led to form the species having unpaired spins with the *g*-factor (2.00301) (Figure 26a). As mentioned in CV section, at the potential of 0.3 V, concomitant two-electron removal causes to generate diradical dication species ***p*-MC**$^{\bullet\bullet2+}$. If the diradical dication is closed-shell, the species is spinless, and therefore the formed species cannot have been detected by EPR spectroscopy. Hyperfine coupling constants (hfcc) cannot be analyzed due to the broad and structure-less EPR spectra, and thereby the structure of the radical species is difficult to identify experimentally. However, the theoretical calculations gave a reasonable chemical interpretation on the EPR experiments (Figure 26d–f). The spin of radical cation and diradical dication of ***p*-MC** delocalized over the whole molecule, mostly on the donor units (Figure 26d), which corresponds to the observed broad and structure-less EPR spectra. Moreover, calculations showed that the triplet configuration of the open-shell diradical dication is slightly more stable than that of open-shell singlet biradical dication (for details, see the former section). After the potential applied to 0.8 V (vs. $Fc/Fc^+$), where the 2nd oxidation process occurs in CV, an EPR signal was still active, and the intensity continuously increased (Figure 26a). Along with results acquired by CV and spectroelectrochemistry, it can be concluded that EPR-active (open-shelled) trication and tetracation species are formed in the second oxidation step. For ***t*-Bu-MC** and **Linear**, similar behavior was observed (Figure 26b and c). When compared to ***p*-MC**, ***t*-Bu-MC** shows much broader signal than ***p*-MC** (Figure 26a and b), probably due to the additional hyperfine couplings influenced by twelve hydrogen nuclei of four *t*-Bu groups. In the case of **Linear**, the EPR signal was more distinctly split than that for macrocycles, which should prove that the spins are more localized (Figure 26c). This was supported by the calculation, which indicates that the spins are localized on donor units: the spin of the radical cation localized on the end donor unit, while that of the diradical dication on the terminal and the internal donor (Figure 26f).

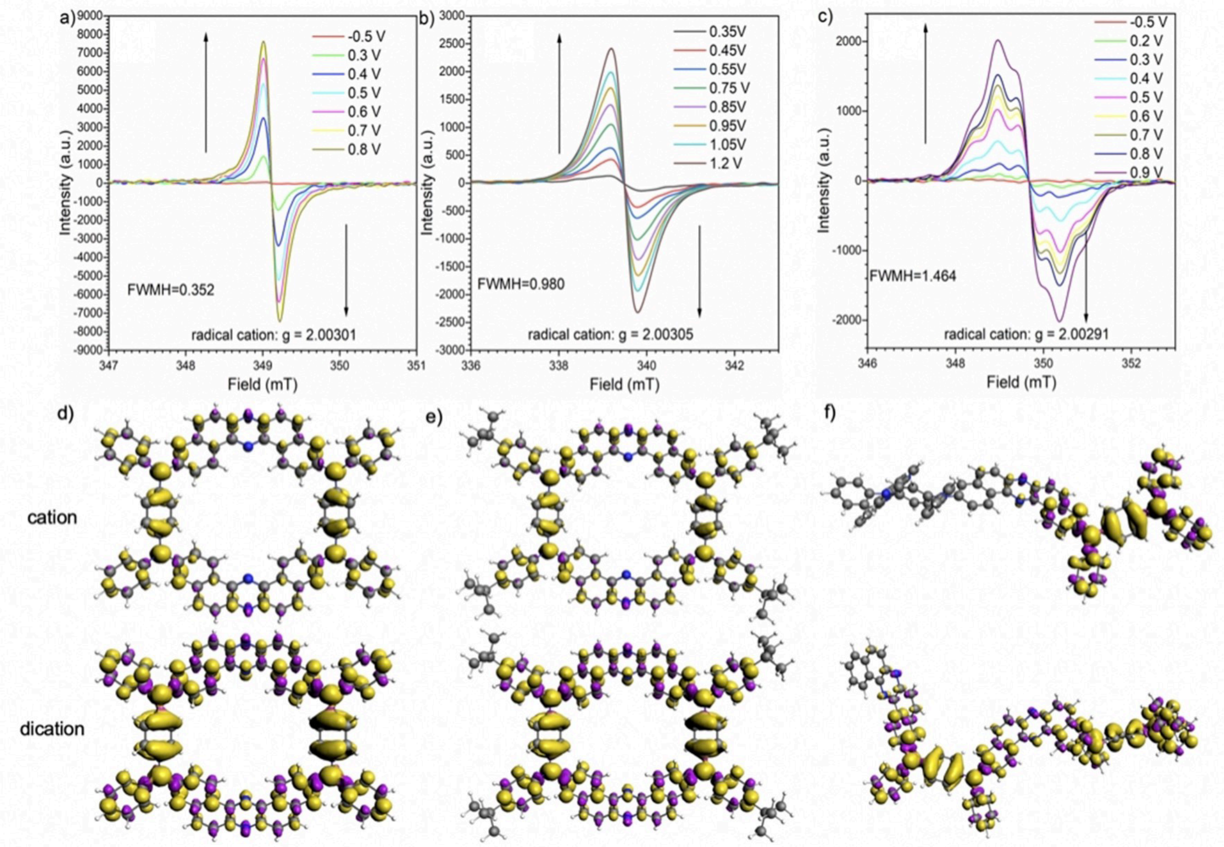

**Figure 26.** Potentiostatic EPR spectroelectrochemistry of (a) ***p*-MC** ($5\times10^{-4}$ M), (b) ***t*-Bu-MC** ($2.5\times10^{-4}$ M), and (c) **Linear** ($5\times10^{-4}$ M) in $CH_2Cl_2$ containing 0.1 M *n*-$Bu_4NBF_4$. Spin density map of cation and dication of (d) ***p*-MC**, (e) ***t*-Bu-MC**, and (f) **Linear** (DFT calculations at the PBE0/TZP level). Reproduced from ref. 17. Copyright 2020 Wiley-VCH Verlag GmbH.

**Potentiodynamic UV-Vis-NIR spectroelectrochemistry.**

UV-Vis-NIR spectroelectrochemical studies, were performed using dichloromethane solutions of ***p*-MC**, **Linear**, and ***t*-Bu-MC** (concentration: $5.0\times10^{-4}$ M for ***p*-MC**, $5.0\times10^{-4}$ M for **Linear**, and $2.5\times10^{-4}$ M for ***t*-Bu-MC**) containing 0.1 M *n*-$Bu_4NBF_4$ as a supporting electrolyte. UV-Vis measurements were carried out in a thin layer spectroelectrochemical cell which was a modification of cells described in the previous literature.[21] An ITO electrode was used as a working electrode, platinum spiral as an auxiliary electrode and silver wire as a pseudo-reference electrode.

To obtain information about the dynamic aspects of the molecular change when varying the voltage, the dynamic spectroelectrochemical analysis during the cyclic voltammperometry process was conducted.[21] Notably, the potentiodynamic analysis reveals why ***t*-Bu-MC** less effectively works on the devices than ***p*-MC** and the factor of the less stability of the ***t*-Bu-MC**-based devices. To understand the difference in CV between ***p*-MC**, **Linear**, and ***t*-Bu-MC**, the potentiodynamic UV-vis spectroelectrochemistry of the compounds was conducted with similar conditions for the CV experiment (Figure 27). In comparison of the potentiostatic process of all compounds, the absorption bands assigned to the neutral form does not increase through oxidation [i.e, $\lambda_{abs}$ (***p*-MC**) = 385, 480 nm; $\lambda_{abs}$ (***t*-Bu-MC**) = 334, 482 nm; and $\lambda_{abs}$ (**Linear**) = 332, 481 nm] (Figure 27a, c, and e). However, the new band with maxima (ca. 420 nm) is formed, which would explain that the increase in the absorption was observed through the potentiostatic process (Figure 25). In the dedoping process, a recursive decrease of spectra was observed in a similar manner but opposite way to the doping process (Figure 27b, d, and f). The behavior and the dynamic aspects of the process was looked closely to make the voltabsorptiometric curves with the particular wavelength (Figure 27g, h, and i).[21] After the oxidation of the ***p*-MC**, the intensity of neutral bands ($\lambda_{abs}$ = 335 and 480 nm) was decreased, accompanied with the sharp increase of the IV–CT bands of radial cationic/diradical dicationic species ($\lambda_{abs}$ = 945 nm) and monoradical tricationic/closed-shell tetracationic species ($\lambda_{abs}$ = 623 nm) (Figure 27g). Notably, in the process of dedoping, a synchronized change of the absorption bands at 335 and 623 nm/480 and 945 nm, where one increases while the other decreases, was observed (black vertical lines in Figure 27g). This would suggest that they are respectively related with the same oxidation stages.

As described above, **Linear** exhibits electrochemical responses, which are typical to conjugated aromatic amines. As the oxidation of **Linear** proceeded, the absorption bands of neutral state ($\lambda_{abs}$ = 332 and 481 nm) was decreased, and IV-CT bands ($\lambda_{abs}$ = 910 nm and 624 nm) were increased (Figure 27i). When the potential dropped after the oxidation of **Linear**, the decrease of IV-CT bands and the reversion of the neutral bands were observed (Figure 27i). For ***t*-Bu-MC**, a significant difference was observed. As the potential increased, the absorption bands of neutral state ($\lambda_{abs}$ = 334 and 482 nm) were decreased, and IV-CT band ($\lambda_{abs}$ = 965 nm) was increased. However, the increase of IV-CT band ($\lambda_{abs}$ = 965 nm) was observed before the intensity of the neutral bands rapidly dropped (Figure 27h). These inconsistent behaviors would suggest that there are problems in the doping process of the diradical dication of ***t*-Bu-MC**. Nevertheless, the process is more chaotic on de-doping (Figure 27d). This seems to be related with the second oxidation process, and the reduction of monoradical trication/closed-shell tetracation species to diradical dication/radical cation species could be disturbed. Structural changes would mostly cause such a difference between ***p*-MC** and ***t*-Bu-MC**. In common with conjugated molecules, during the oxidation, quinoidal structures to allow the electron transfer should be formed, which often accompanied with the planarization of the molecule.[24] In the case of ***p*-MC**, certain symmetry, which allows for the generation of monoradical trication/closed-shell tetracation directly after the diradical dicationic state, was observed. This was proven by the appearance of the band around 600–750 nm, before the distinction of monoradical cationic/diradical dicationic species become possible (Figure 27a). Opposite behavior was observed for ***t*-Bu-MC**. After the first oxidation, the structure is probably locked due to the additional steric hindrance group, which is making some trouble with doping and flattening of the structure.[25] This would suggest that the structure of ***t*-Bu-MC**$^{2+}$ is not symmetrical, which is preventing uniform distribution of the charges. In addition, the behaviors of ***t*-Bu-MC** observed in electrochemical and spectroelectrochemical measurement prove an evident problem with the de-doping process, which was caused by the second quasi-reversible oxidation process in the CV. After the charge-injection, a partial degradation of ***t*-Bu-MC**$^{2+}$ would be caused by such asymmetric structural changes in the emissive layer, resulting in lowering the efficiency and roll-off of the device.

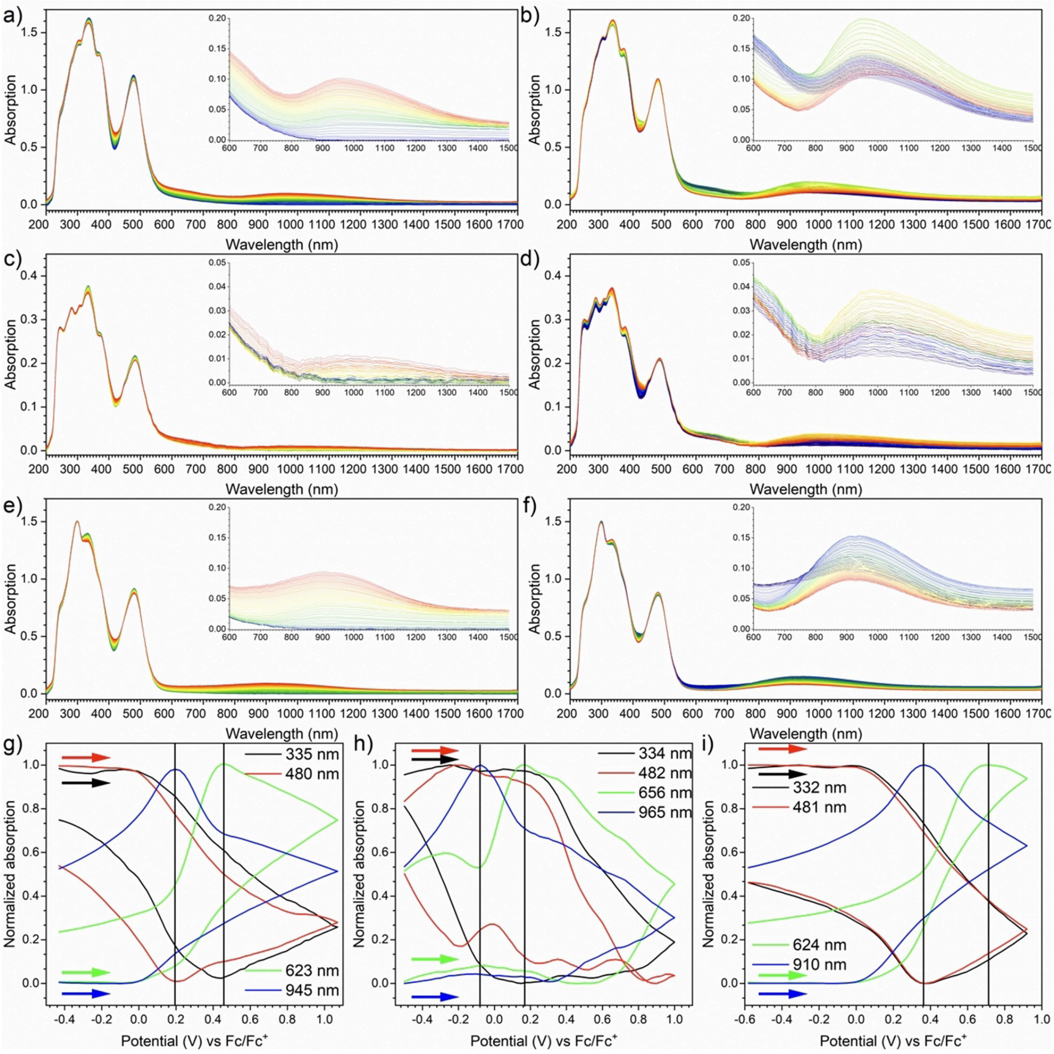

**Figure 27.** Potentiodynamic UV-Vis-NIR spectroelectrochemistry of doping process of (a) ***p*-MC** ($5\times10^{-4}$ M), (c) ***t*-Bu-MC** ($2.5\times10^{-4}$ M), and (e) **Linear** ($5\times10^{-4}$ M); dedoping process of (b) ***p*-MC** ($5\times10^{-4}$ M), (d) ***t*-Bu-MC** ($2.5\times10^{-4}$ M), and (f) **Linear** ($5\times10^{-4}$ M) in $CH_2Cl_2$ containing 0.1 M *n*-$Bu_4NBF_4$, scan rate 50 mV/s. Cyclic voltabsorptiometric measurement of (g) ***p*-MC** ($5\times10^{-4}$ M), (h) ***t*-Bu-MC** ($2.5\times10^{-4}$ M), and (i) **Linear** ($5\times10^{-4}$ M) in $CH_2Cl_2$ containing 0.1 M *n*-$Bu_4NBF_4$, scan rate 50 mV/s. Reproduced from ref. 17. Copyright 2020 Wiley-VCH Verlag GmbH.

## 2-6. References

1) Wang, C.; Li, Z. *Mater. Chem. Front.* **2017**, *1*, 2174−2194.
2) Izumi, S.; Higginbotham, H. F.; Nyga, A.; Stachelek, P.; Tohnai, N.; de Silva, P. Data, P.; Takeda, Y.; Minakata, S. *J. Am. Chem. Soc.* **2020**, *142*, 1482–1491.
3) Izumi, S.; Nyga, A.; de Silva, P.; Tohnai, N.; Minakata, S.; Data, P.; Takeda, Y.; *Chem. Asian J.* **2020**, *15*, 4098–4103.
4) Takeda, Y.; Okazaki, M.; Minakata, S. *Chem. Commun.* **2014**, *50*, 10291−10294.
5) Yang, T.-F.; Chiu, K. Y.; Cheng, H. C.; Lee, Y. W.; Kuo, M. Y.; Su, Y. O. *J. Org. Chem.* **2012**,

*77*, 8627−8633.

6) de Silva, P.; Kim, C. A.; Zhu, T.; Voorhis, T. V. *Chem. Mater.* **2019**, *31*, 6995−7006.
7) (a) Data, P.; Pander, P.; Okazaki, M.; Takeda, Y.; Minakata, S.; Monkman, A. P. *Angew. Chem., Int. Ed.* **2016**, *55*, 5739−5744. (b) Okazaki, M.; Takeda, Y.; Data, P.; Pander, P.; Higginbotham, H.; Monkman, A. P.; Minakata, S. *Chem. Sci.* **2017**, *8*, 2677−2686. (c) Data, P.; Okazaki, M.; Minakata, S.; Takeda, Y. *J. Mater. Chem. C* **2019**, *7*, 6616−6621. (d) Takeda, Y.; Kaihara, T.; Okazaki, M.; Higginbotham, H.; Data, P.; Tohnai, N.; Minakata, S. *Chem. Commun.* **2018**, *54*, 6847−6850.
8) Kuang, Z.; He, G.; Song, H.; Wang, X.; Hu, Z.; Sun, H.; Wan, Y.; Guo, Q.; Xia, A. *J. Phys. Chem. C* **2018**, *122*, 3727−3737.
9) Wu, C.; Djurovich, P. I.; Thompson, M. E. *Adv. Funct. Mater.* **2009**, *19*, 3157−3164.
10) Yeh, S. J.; Tsai, C. Y.; Huang, C.-Y.; Liou, G.-S.; Cheng, S.-H. *Electrochem. Commun.* **2003**, *5*, 373–377.
11) Ito, A.; Ino, H.; Tanaka, K.; Kanemoto, K.; Kato, T. *J. Org. Chem.* **2002**, *67*, 491–498.
12) (a) Software CrysAlisPro 1.171.39.20a: Rigaku Oxford Diffraction (2015), Software CrysAlisPro 1.171.39.20a Rigaku Corporation, Tokyo, Japan (b) Software CrysAlisPro 1.171.41.79a: Rigaku Oxford Diffraction (2020), Software CrysAlisPro 1.171.41.79a Rigaku Corporation, Tokyo, Japan.
13) (a) SHELXT Version 2014/5: Sheldrick, G. M. *Acta Cryst.* **2014**, *A70*, C1437. (b) SHELXT Version 2015: Sheldrick, G. M. *Acta Cryst.* **2015**, *A71*, 3–8.
14) (a) CrystalStructure 4.2.4: Crystal Structure Analysis Package, Rigaku Corporation (2016). Tokyo 196-8666, Japan. (b) CrystalStructure 4.2.5: Crystal Structure Analysis Package, Rigaku Corporation (2017). Tokyo 196-8666, Japan. (c) Olex$^2$ 1.3: Dolomanov, O. V.; Bourhis, L. J.; Gildea, R. J.; Howard, J. A. K.; Puschmann, H. *J. Appl. Cryst.* **2009**, *42*, 339–341.
15) (a) SHELXL Version 2014/7: Sheldrick, G. M. *Acta Cryst.* **2008**, *A64*, 112–122. (b) SHELXL Version 2018/1: Sheldrick, G. M. *Acta Cryst.* **2008**, *A64*, 112–122. (c) SHELXL Version 2018/3: Sheldrick, G. M. *Acta Cryst.* **2015**, *C71*, 3–8.
16) (a) Cardona, C. M.; Li, W.; Kaifer, A. E.; Stockdale, D.; Bazan, G. C. *Adv. Mater.* **2011**, *23*, 2367–2371 (b) Bredas, J.-L. *Mater. Horiz.* **2014**, *1*, 17–19.
17) Nyga, A.; Izumi, S.; Higginbotham, H. F.; Stachelek, P.; Pluczyk, S.; de Silva, P.; Minakata, S.; Takeda, Y.; Data, P. *Asian J. Org. Chem.* **2020**, *9*, 2153–2161.
18) Shao, Y. et al. *Mol. Phys.* **2015**, *113*, 184–215.

19) Baerends, E. J. et al. ADF 2019.3, SCM, Theoretical Chemistry, Vrije Universiteit, Amsterdam, The Netherlands, http://www.scm.com.

20) te Velde, G.; Bickelhaupt, F. M.; Baerends, E. J.; Fonseca Guerra, C.; van Gisbergen, S. J. A.; Snijders, J. G.; Ziegler, T. *J. Comp. Chem.* **2001**, *22*, 931–967.

21) (a) Data, P.; Motyka, R.; Lapkowski, M. Suwinski, J.; Monkman, A. P. *J. Phys. Chem. C* **2015**, *119*, 20188–20200. (b) Pluczyk, S.; Vasylieva, M.; Data, P.; *J. Vis. Exp.* **2018**, *140*, e56656.

22) (a) Lambert, C.; Nöll, G. *J. Am. Chem. Soc.* **1999**, *121*, 8434–8442. (b) Coropceanu, V.; Malagoli, M.; André, J. M.; Brédas, J. L. *J. Am. Chem. Soc.* **2002**, *124*, 10519–10530. (c) Szeghalmi, A. V.; Erdmann, M.; Engel, V.; Schmitt, M.; Amthor, S.; Kriegisch, V.; Nöll, G.; Stahl, R.; Lambert, C.; Leusser, D.; Stalke, D.; Zabel, M.; Popp, J. *J. Am. Chem. Soc.* **2004**, *126*, 7834–7845.

23) Ito, A. *J. Mater. Chem. C* **2016**, *4*, 4614–4625.

24) (a) Zeng, Z.; Shi, X.; Chi, C.; Navarrete, J. T. L.; Casado, J.; Wu, J. *Chem. Soc. Rev.* **2015**, *44*, 6578–6596.; (b) Pittelli, S. L.; De Keersmaecker, M.; Ponder Jr, J. F.; Österholm, A. M.; Ochieng, M. A.; Reynolds, J. R. *J. Mater. Chem. C* **2020**, *8*, 683–693.

25) (a) Colella, L.; Brambilla, L.; Nardone, V.; Parisini, E.; Castiglioni, C.; Bertarelli, C.; *Phys. Chem. Chem. Phys.* **2015**, *17*, 10426–10437.; (b) Casado, J.; Ortiz, R. P.; Navarrete, J. T. L. *Chem. Soc. Rev*. **2012**, *41*, 5672–5686.

# Chapter 3

# Investigation of Thermally Activated Delayed Fluorescence Properties of D–A–D–A π-Conjugated Macrocycles and their Applications to OLEDs

## 3-1. Organic Light-emitting Diode

Organic light-emitting diodes (OLEDs) are a type of light emitting diode in which the emissive layer is composed of organic compounds (Figure 1). Since the first prototype of OLED device based on small molecular luminescent materials was reported in 1987 by Tang and VanSlyke,[1] diverse types of OLEDs using a fluorescence and a heavy-metal-containing phosphorescence emitter have been extensively developed. Nowadays, OLEDs are already commercially used for displays of smartphones and televisions due to their thin and lightweight features, and also higher contrast and lower power consumption characters compared to traditional liquid crystal displays.

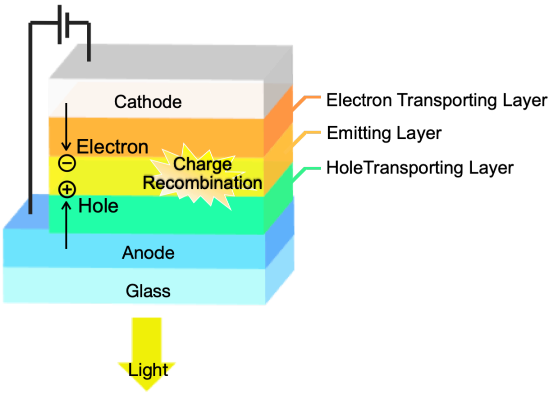

**Figure 1.** Structure of a general OLED device.

In an OLED, electrons and holes injected into the device recombine in the emitting layer, and the singlet and triplet excitons are consequently generated in the singlet-to-triplet ratio of 25:75, according to the spin statistics rule. In the case of fluorescent OLED materials, since only singlet excitons can be utilized for emitting light, the 75% of the electrical energy injected into the device is wasted, and thereby the maximum internal quantum efficiency (IQE) of the OLED is 25% (Figure 2a). Given that the light extraction efficiency is around 20%, the maximum EQE of OLEDs fabricated with a conventional fluorescent emitter is theoretically less than 5%. In contrast, phosphorescent materials allow for converting all the singlet excitons to the triple excitons through intersystem crossing (ISC), thus both singlet and triplet excitons can be harvested and converted into light as phosphorescence (Figure 2b). As the result, 100% IQE of the device is achievable. However, the majority of phosphorescent materials contain rare heavy metals such as Ir and Pt, for the purpose of enhancing large spin-orbit coupling (SOC). This causes high cost of production of OLEDs and lack of environmental sustainability. TADF organic materials offer an alternative to fluorescent and phosphorescent compounds as light emitters for OLEDs, as they fulfill the requirements of all of quantum efficiency, cost, and resource sustainability. OLEDs with a purely organic TADF emitter achieve the maximum 100% IQE by harvesting electrically generated triplet excitons through the efficient reverse intersystem crossing (rISC) process without the use of heavy metals (Figure 2c). Therefore, the maximum of OLEDs with the TADF emitters reach 20%.

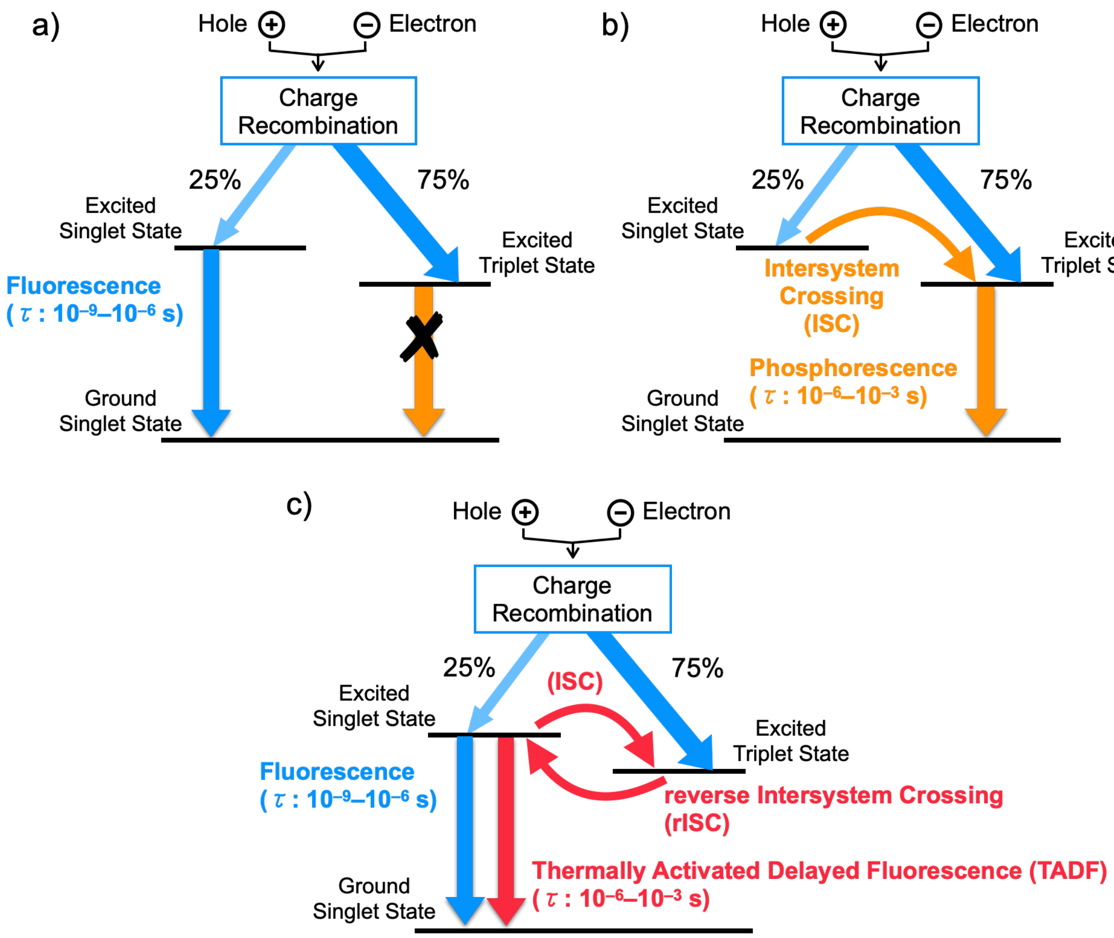

**Figure 2**. Exciton energy diagram and the possible decay pathways of singlet and triplet excitons, from (a) a conventional fluorescent emitter, (b) a phosphorescent emitter, and (c) a TADF emitter.

## Results and Discussion

### 3-2. Investigation of TADF Properties in Toluene Solutions

TADF emission is sensitive toward the presence of molecular oxygen, which can quickly quench the long-lived triplet-excited states through energy transfer or electron transfer mechanisms. To investigate how much TADF contributes to the photoluminescence (PL) of the macrocycles and the linear compound in solutions, their photoluminescent spectra in aerated and degassed toluene solutions were measured and compared (Figure 3). The significant decrease

(66%) in PL intensity of the emission was observed for ***p*-MC** in aerated toluene when compared to the degassed solution (Figure 3a). Upon the injection of oxygen gas, the intensity of the PL of **Linear** was also decreased, but the decline rate (24%) was smaller than that for ***p*-MC** (Figure 3a *vs* Figure 3b). Assuming that the emission observed under aerated and degassed conditions can be related to the prompt fluorescence (PF) and the sum of the PF and the delayed fluorescence (DF) via the triplet state, respectively, the number expressed by the equation {(DF/PF) − 1} × 100 (%) would indicate the % of the harvested triplet in a form of DF. From the comparison of the DF/PF ratio of ***p*-MC** and **Linear**, ***p*-MC** is considered as a much more promising TADF material than **Linear**. In contrast, the PL intensity of ***m*-MC** was little affected by the presence of oxygen, which would indicate little TADF contribution in PL from ***m*-MC** solution (Figure 3c).

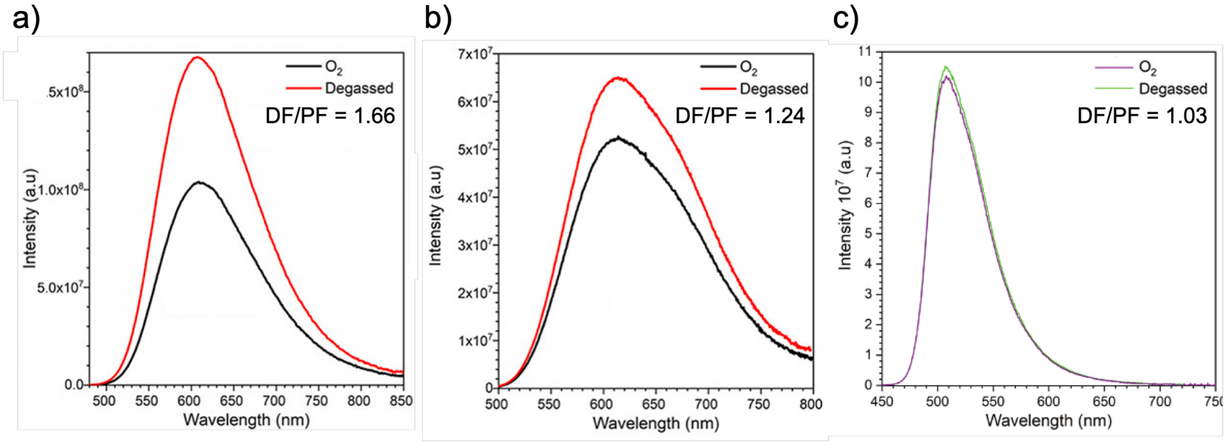

***c*** = 5×10⁻⁶ M.
($\lambda_{ex}$ = 470 nm)

***c*** = 5×10⁻⁶ M.
($\lambda_{ex}$ = 470 nm)

***c*** = 1×10⁻⁵ M.
($\lambda_{ex}$ = 365 nm)

**Figure 3.** PL spectra of aerated and degassed toluene solutions of (a) ***p*-MC**, (b) **Linear**, and (c) ***m*-MC**. (a) and (b) Adapted from ref. 2. Copyright 2020 American Chemical Society. (c) Adapted from ref. 3. Copyright 2020 Wiley-VCH Verlag GmbH.

## 3-3. Investigation of TADF Properties in Films

In most cases, the light-emitting layer of OLED is composed of a light-emitting material uniformly dispersed into a host material. To investigate the photophysics of the D–A–D–A compounds in host matrices, time-resolved luminescence spectroscopic analyses of thin films composing of an emitter in a nonpolar cycloolefin polymer (COP) matrix and a small molecular host matrix 4,4’-bis(*N*-carbazolyl)-1,1’-biphenyl (CBP) were performed (Figures 4 and 5). In both host matrices, ***p*-MC** and **Linear** displayed emissions in two distinct time regions (Figure 5). The first component, decaying with a lifetime in the nanosecond time range in all of the materials, is identified as PF from the singlet excited state ($S_1$), due to the temperature-independent emission profiles (Figures 4 and 5). In both cases (***p*-MC** and **Linear)**, the spectra at the time delay (TD) of 15 ns in both COP and CBP showed single Gaussian-type spectra attributed to emission from singlet charge-transfer state ($^1$CT) that decays over longer times (black lines, Figure 4). At a longer delay time in the micro- and millisecond time regions, delayed emissions were observed (Figure 5). Depending on the experimental temperature, both delayed emission from the singlet state and emission from the triplet state were found on similar millisecond time scales. Accordingly, the spectral examination at different temperature easily elucidates the emission from each state. At room temperature, the delayed emission was observed with the same spectral shape and onset energy as the prompt emission spectra from $^1$CT (red lines, Figure 4), which was attributed to TADF. The linear power dependence (slope ≒ 1.00) of the integrated emission intensity in the millisecond region of ***p*-MC** and **Linear** on laser pulse fluence also supported this assignment (Figures 12 and 13 in the Experimental Section). The emissions from the triplet state were observed at low temperatures (blue lines, Figure 4), with the triplet energy ($E_{T1}$) for ***p*-MC** being 2.19 eV in both COP and CBP hosts (Figure 4a and c). Due to the slightly higher dielectric constant of the CBP host[4] than that of COP host,[5] the $^1$CT energy of ***p*-MC** in CBP is stabilized to the lower energy (2.37 eV) than that in COP (2.43 eV). As the result, the $\Delta E_{ST}$ of ***p*-MC** dropped from 0.24 eV in COP to 0.18 eV in CBP, indicating a moderate exchange energy. The $\Delta E_{ST}$ values calculated at ω*PBE/cc-pVDZ level using the optimized ground-state structures for **helical** and **saddle** conformers (Tables 8 and 9 in Chapter

2) were found to be 0.55 and 0.50 eV, respectively. These values are relatively large when compared to the experimental gaps obtained with time-resolved emission spectroscopy. This suggests that the excited-state relaxation plays an important role in the emission process.

On one hand, the behavior of **Linear** was slightly different from that of ***p*-MC**. The $E_{T1}$ of **Linear** in COP (2.23 eV) is much higher than that in CBP host (2.11 eV) (Figure 4b and d). This would suggest that the triplet excited states of **Linear** are more influenced by the fluctuation of structural conformation when compared to ***p*-MC**, thereby the conformer with low $E_{T1}$ is formed. As with ***p*-MC**, the polarity of the host matrix influenced and lowered the $^1$CT energy of **Linear**, and thereby the $\Delta E_{ST}$ of **Linear** was narrowed from 0.25 eV in COP to 0.20 eV in CBP.

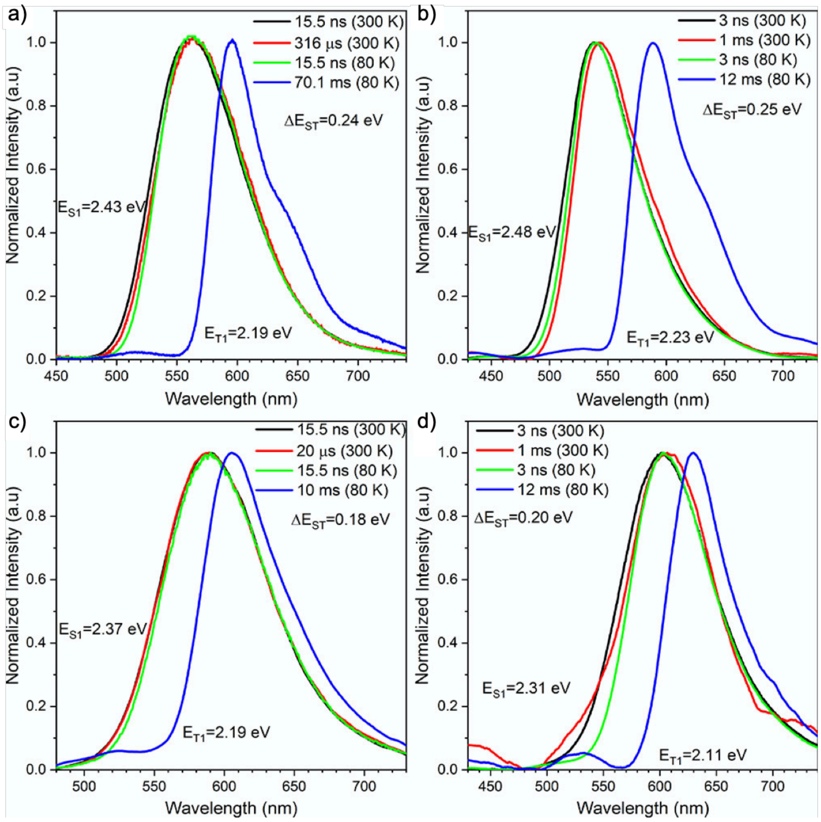

**Figure 4.** Normalized emission spectra of ***p*-MC** and **Linear** in host matrices at varying delay times at 300 and 80 K: (a) ***p*-MC** and (b) **Linear** in COP (1 wt % in host matrix); and (c) ***p*-MC** and (d) **Linear** in CBP (10 wt % in host matrix). Reproduced from ref. 2. Copyright 2020 American Chemical Society.

The intensity decays of the emission at different time delays for ***p*-MC** and **Linear** in COP and CBP were measured (Figure 5). In all cases, the PF and phosphorescence (PH) decay curves of both compounds are distinctive of CT-based organic TADF emitters.[6] The DF process increased in all films as the temperature elevated, however, on close inspection, the temperature dependence of the decay profiles of ***p*-MC** and **Linear** were different from each other. The DF process started at a much lower temperature for ***p*-MC** (ca. 120 K) than for **Linear** (ca. 200 K), which would indicate that a higher activation energy is required for the rISC process in the case of that of **Linear**. In addition, the rise of DF component of **Linear** in both films is much weaker than ***p*-MC** in the same matrices, suggesting that TADF has less contributed to the PL of **Linear** in host matrices than ***p*-MC**. These results are in good agreement with the results obtained with solutions (Figure 3a and b). Therefore, **Linear** exhibits a lower device efficiency than ***p*-MC** (Figure 7, *vide infra*).

From above the macrocyclization of the D–A–D–A structure dose not significantly influence $\Delta E_{\mathrm{ST}}$ and $\Delta E_{Ea}$, which are key factors for TADF (Figure 4 and Figure 12 and 13 in the Experimental Section). Given that these values of ***p*-MC** and **Linear** are almost the same, the difference in TADF efficiency of ***p*-MC** and **Linear** could be derived from the degree of conformational freedom of the compounds. Since **Linear** can change its conformation more easily than ***p*-MC** by the rotation around the D–A connections and/or N-C (Ph) bonds. Consequently, the triplet excitons of **Linear** would be easily quenched by molecular motion when compared to ***p*-MC**, which results in the low TADF efficiency of **Linear**.

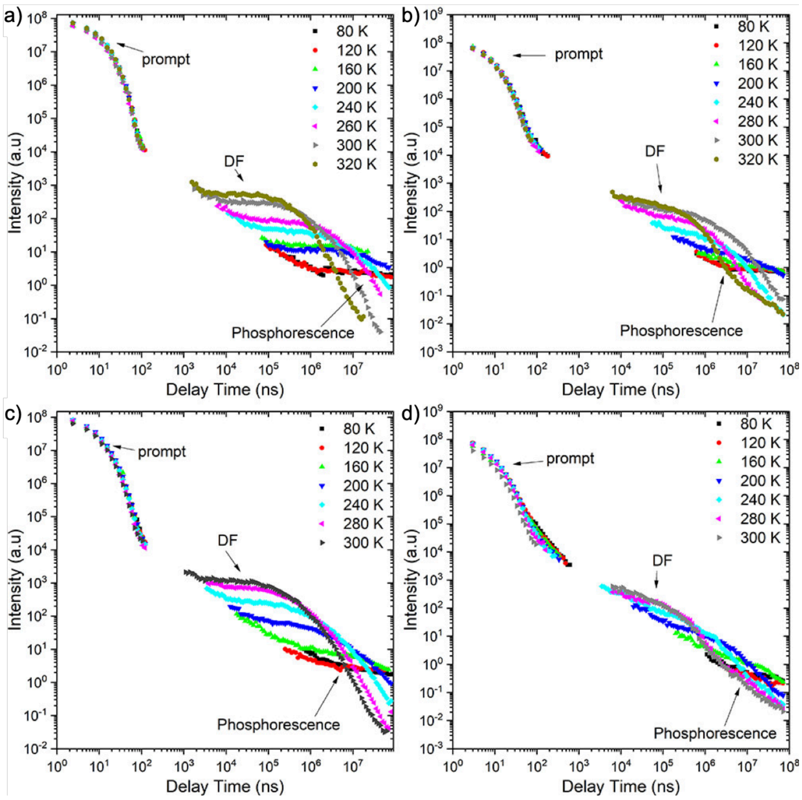

**Figure 5.** Emission intensities of ***p*-MC** and **Linear** in host matrices against delay time measured at different temperatures: (a) ***p*-MC** and (b) **Linear** in COP (1 wt % in host matrix); and (c) ***p*-MC** and (d) **Linear** in CBP (10 wt % in host matrix). Reproduced from ref. 2. Copyright 2020 American Chemical Society.

The photophysics of ***m*-MC** in host matrices were also investigated by time-resolved spectroscopic analyses of blending films (1 wt% ***m*-MC** in COP, and 10 wt% ***m*-MC** in CBP) (Figure 6). Prompt emission at the time delay of 5 ns in both films displayed Gaussian-type spectra centered at around 520 nm (black and blue lines, Figure 6a; red line, Figure 6b). In COP, delayed emission in the microsecond-time region at ambient temperature (300 K) nicely matched with the prompt emission (red line, Figure 6a), which proves that the delayed emission radiated from the singlet excited state ($S_1$). The slope of the delayed emission integral against the laser pulse energy was found to be 1.00 (Figure 14 in the Experimental Section), and this result proves the delayed emission as TADF. As with ***p*-MC** and **Linear**, the phosphorescence spectra in COP (green, Figure 6a) showed similar one to that of DBPHZ ($^3LE_A$).[7] The triplet energy ($E_{T1}$) calculated from the phosphorescence spectra (2.39 eV) is slightly higher than that of ***p*-MC** ($E_{T1}$

= 2.19 eV in COP) but almost the same as those of DBPHZ-cored twisted D–A–D TADF emitters.[8] This would suggest that the increase in the $T_1$ energy of ***m*-MC** when compared to ***p*-MC** is attributed to breaking electronic delocalization by the meta substitution topology. The $^1$CT energy of ***m*-MC** is also destabilized to give higher singlet energy ($E_{S1}$ = 2.70 eV) than that of ***p*-MC** ($E_{S1}$ = 2.43 eV). The energy is also about 0.3 eV higher than those of previously reported D–A–D TADF compounds.[8] As a result, $\Delta E_{ST}$ of ***m*-MC** in COP is 0.31 eV, which is little wider than that of ***p*-MC** (0.24 eV). This was qualitatively reproduced by the theoretical calculations at the ωPBE/cc-pVDZ level: calculated $\Delta E_{ST}$ for ***m*-MC** is 0.37 eV (Table 10 in Chapter 2) and that for ***p*-MC** is 0.50 eV. Importantly, *meta*-type macrocycle ***m*-MC** in CBP displays no or very faint TADF emission, which is in contrast with ***p*-MC**. From the time-resolved analysis of ***m*-MC** in the CBP matrix, a delay component was not observed, and the phosphorescence was not found even at low temperature (Figure 6b and d). These results exclude ***m*-MC** as an efficient OLED emitter. Taking the electrochemical instability of ***m*-MC** into account, the analysis of ***m*-MC** in an OLED device was not performed.

While ***p*-MC** shows efficient TADF in both solution and host matrices, ***m*-MC** exhibits little TADF in toluene solution and no TADF in CBP. The replacement of *para*-type donors to *meta*-type donors reduces the CT nature in the excited states. Electrons of the amino group in *para* position could be transferred to DBPHZ through overlapping orbitals, however those in *meta* position could not do so due to the breaking electronic delocalization. Therefore, $^1$CT energy of ***m*-MC** would be destabilized, when compared to ***p*-MC**. However, the $^3$LE energy was not drastically affected by the difference of donor, due to the twisted structures. As a consequence, $\Delta E_{ST}$ ($^1$CT–$^3$LE) became wider in ***m*-MC** than ***p*-MC**, and the rISC cannot occur to show TADF.

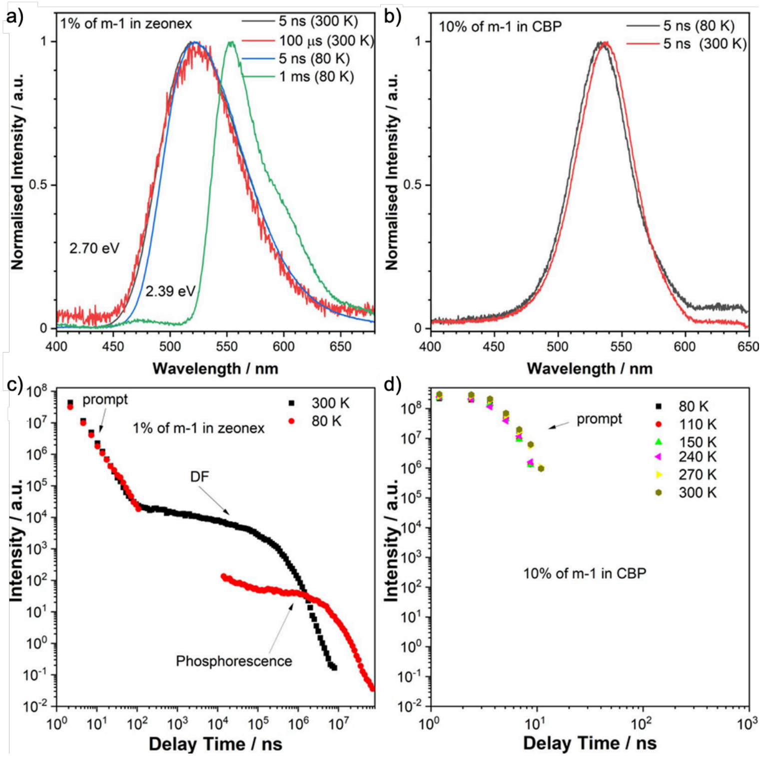

**Figure 6.** Prompt fluorescence, delayed fluorescence, and phosphorescence spectra of ***m*-MC** in (a) COP (1 wt % in host matrix) and (b) CBP (10 wt % in host matrix). Photoluminescence decay of ***m*-MC** in (c) COP (1 wt % in host matrix) and (d) CBP (10 wt % in host matrix). Reproduced from ref. 3. Copyright 2020 Wiley-VCH Verlag GmbH.

The photophysics of ***t*-Bu-MC** embedded in host matrices (1 wt% ***t*-Bu-MC** in COP, and 10 wt% ***t*-Bu-MC** in CBP) was also investigated (for the details, see Experimental Section). As is the case for ***p*-MC** and **Linear**, the host affected the $^1$CT energy: the $^1$CT energy of ***t*-Bu-MC** in CBP (2.29 eV) was 0.42 eV lower than that in COP (2.71 eV) (Figure 15a and b in the Experimental Section). In contrast to ***p*-MC** and **Linear**, the change of the host from COP to CBP stabilized the triplet state energy of ***t*-Bu-MC** by 0.20 eV, and both $^1$CT and $^3$CT energies were lowered in CBP than in COP. As consequence, the smallest $\Delta E_{ST}$ gap (0.15 eV) among all the investigated compounds (***p*-MC** 0.18 eV; Linear 0.20 eV) was achieved with ***t*-Bu-MC** in CBP. As small $\Delta E_{ST}$ gap (0.15 eV), the OLED devices fabricated with ***t*-Bu-MC** showed high EQE (10.4%), which is a slightly lower value than that with ***p*-MC** (*vide infra*). However, ***t*-Bu-MC** have a problem with electrochemical stability (for details, see Chapter 2), the roll-off in high current region was observed in the device fabricated with ***t*-Bu-MC** (*vide infra*).

### 3-4. Fabrication and Characteristics of OLED Devices

To examine the possibility of applying ***p*-MC** and **Linear** as an emitter to OLED devices, thermal stability of ***p*-MC** and **Linear** was investigated under air and $N_2$ atmosphere by thermogravimetric analysis (TGA) (Figures 8 and 9 in the Experimental Section). High thermal decomposition temperatures [$T_d$ (5 wt% loss) 548−585 °C for ***p*-MC** and 535−578 °C for **Linear**] showed that both molecules would be applicable to vacuum thermal deposition for purification and fabrication of OLEDs. To evaluate the electroluminescence performances of ***p*-MC** and **Linear** as a TADF emitter, OLED devices were fabricated with ***p*-MC** and **Linear** through the coevaporation technique. The fabricated device structure was as follows: ITO/NPB (40 nm)/10 wt % ***p*-MC** or **Linear** in CBP (30 nm)/TPBi (50 nm)/LiF (1 nm)/Al (100 nm). The both OLEDs fabricated with ***p*-MC** and **Linear** exhibited low turn-on voltage of 2.0 and 2.5 V, respectively (Figure 7a). Notably, the device fabricated with ***p*-MC** as the emitter showed a bright orange emission ($\lambda_{\max}$ 589 nm), and the maximum EQE was achieved up to 11.6%, which far exceeded the theoretical maximum EQE of that with a conventional fluorescent material (5%). It should be noted that this represents the first example of a purely organic π-conjugated macrocyclic TADF emitter for OLEDs. More importantly, the EQE of the OLEDs fabricated with ***p*-MC** was also far superior to that with **Linear** (up to 6.9%, Figure 7b). The luminance of device fabricated with ***p*-MC** was quite higher (>23,000 cd $m^{-2}$) than that of **Linear** (ca. 12,500 cd $m^{-2}$), which suggested better charge recombination in the device based on ***p*-MC** (Figure 7c). Both devices showed low-to-moderate efficiency roll-off (the roll-offs of current efficiencies at 1000 cd $m^{-2}$ were 3.9% for ***p*-MC** and 16.0% for **Linear**) (Figure 7d).

As for the device fabricated with ***t*-Bu-MC** as an emitter, the electroluminescence of the OLED device was evaluated (for the details, see Experimental Section). After long device optimization, the best structure was found to be ITO/HAT-CN (10 nm)/NPB (30 nm)/TAPC (10 nm)/7 wt% ***t*-Bu-MC** in CBP (25 nm)/TPBi (50 nm)/LiF (1 nm)/Al (100 nm). The EQE of the device fabricated with ***t*-Bu-MC** was ca. 10.4%, which was slightly lower value than that with ***p*-MC** (11.6%) (Figure 16b). However, in contrast to ***p*-MC** and **Linear**, the device fabricated with ***t*-Bu-MC** showed roll-off in the high current density region (Figure 16). This was probably caused by less stability in electrochemical process of the emitter of ***t*-Bu-MC** (for the details, Experimental Section in Chapter 2). These results indicated that ***t*-Bu-MC** was inferior to ***p*-MC** as TADF emitter for OLED.

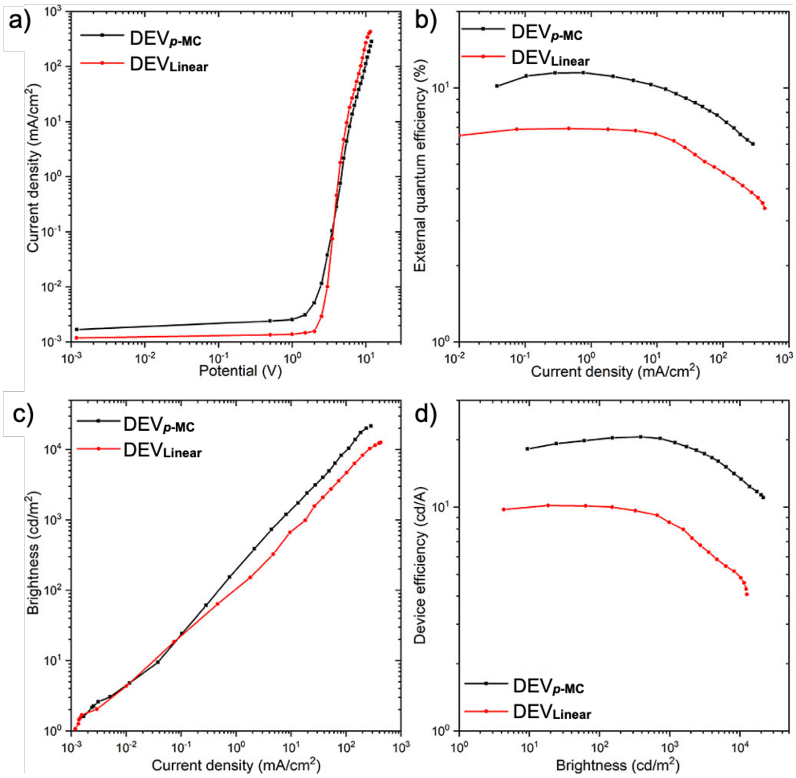

**Figure 7.** Characteristics of devices fabricated with ***p*-MC** and **Linear**. Adapted from ref. 2. Copyright 2020 American Chemical Society.

## 3-5. Summary

It was found that TADF phenomena in solutions and matrices was observed from ***p*-MC** and **Linear**, while ***m*-MC** showed faint or no TADF emission in solutions and matrices due to its topology of the donor. Finally, the author revealed that D–A–D–A π-conjugated macrocycle comprising of DBPHZs as acceptors and *p*-phenylenediamine derivatives (i.e. ***p*-MC**) shows efficient TADF, and the EQE of OLED device fabricated with ***p*-MC** achieved as high value as 11.6%, which far exceeded those with **Linear** and a conventional fluorescent material. The macrocyclization of D–A–D–A framework would prevent quenching the triplet excitons by molecular motions caused by single bond rotations.

## 3-6. Experimental Section

### General remarks.

Thermogravimetric analysis was performed with TG/DTA-7200 system (SII Nano Technology Inc.). Photoluminescence spectra of thin films were recorded at room temperature with Edinburgh Instruments FLS980 fluorescence spectrometer with Xe-lamp as an excitation source and R-928 photomultiplier detector. Phosphorescence, prompt fluorescence, and delayed fluorescence spectra and decays were recorded using nanosecond gated luminescence and lifetime measurements (from 400 ps to 1 s) using either third harmonics of a high energy pulsed Nd:YAG laser emitting at 355 nm (EKSPLA) or a $N_2$ laser emitting at 337 nm. Emission was focused onto a spectrograph and detected on a sensitive gated iCCD camera (Stanford Computer Optics) having a sub-nanosecond resolution. PF/DF time-resolved measurements were performed by exponentially increasing gate and integration times. Temperature-dependent experiments were conducted using a continuous flow liquid nitrogen cryostat (Janis Research) under a nitrogen atmosphere.

**Materials.**

CBP: 4,4'-bis(*N*-carbazolyl)-1,1'-biphenyl (Sigma Aldrich), NPB: *N*,*N*'-di(1-naphthyl)-*N*,*N'*-diphenyl-(1,1'-biphenyl)-4,4'-diamine (TCI-Europe), HAT-CN: 2,3,6,7,10,11-hexacyano-1,4,5,8,9,12-hexa-azatriphenylene (Sigma Aldrich), TAPC: 1,1-bis[(di-4-tolylamino)phenyl]cyclohexane (Sigma Aldrich), TPBi: 2,2',2"-(1,3,5-Benzinetriyl)-tris(1-phenyl-1*H*-benzimidazole) (LUMTEC), LiF (99.995%, Sigma Aldrich), and Aluminum wire (99.9995%, Alfa Aesar) for use in TADF emitter were purchased from the companies indicated in each parentheses. All purchased materials were purified by temperature-gradient sublimation in a vacuum.

**Thermogravimetric analysis (TGA).**

The TGA profiles of ***p*-MC**, **Linear**, ***m*-MC** and ***t*-Bu-MC** were obtained using a Pt pan under the air or the $N_2$ gas flow (200 mL/min), starting from 40 °C to 1000 °C at the ramp rate of 10 °C/min (Figure 8–11).

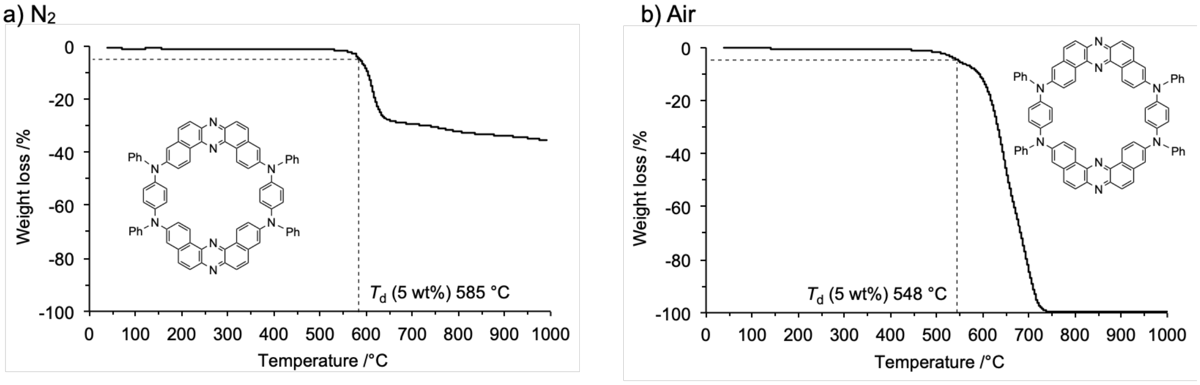

**Figure 8.** TGA profiles of ***p*-MC** under (a) a $N_2$ gas flow and (b) the air. Adapted from ref. 2. Copyright 2020 American Chemical Society.

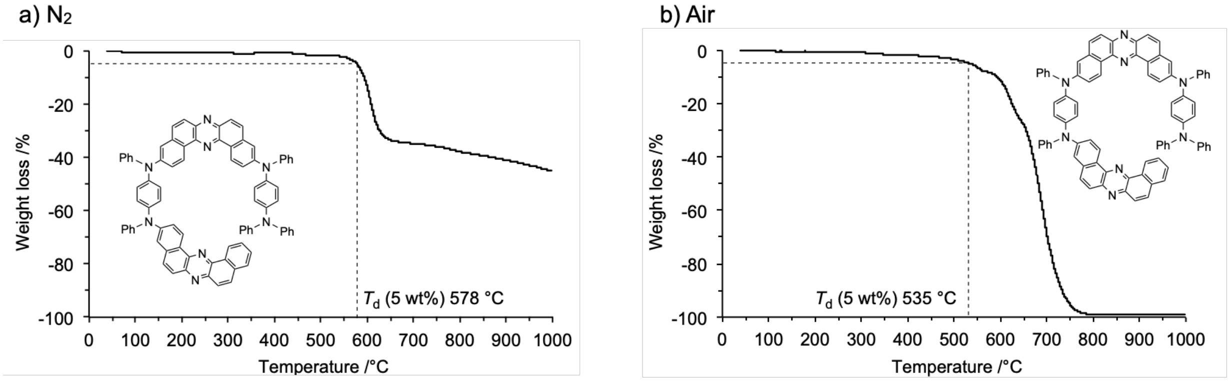

**Figure 9.** TGA profiles of **Linear** under (a) a $N_2$ gas flow and (b) the air. Adapted from ref. 2. Copyright 2020 American Chemical Society.

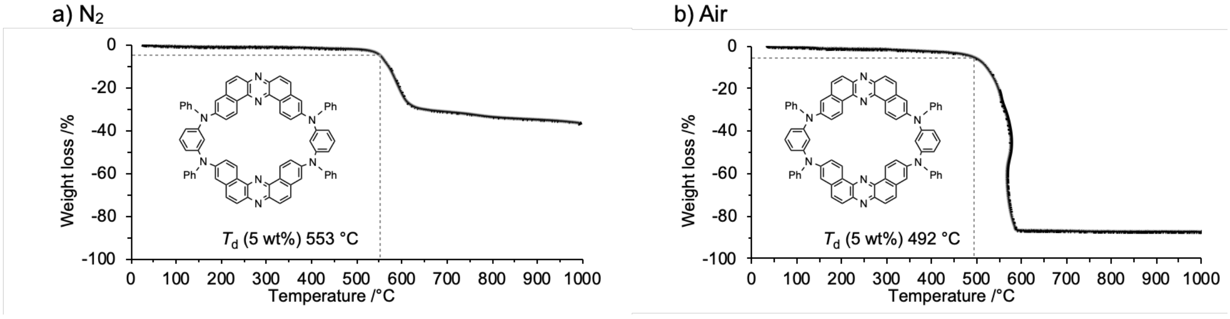

**Figure 10.** TGA profiles of ***m*-MC** under (a) a N$_2$ gas flow and (b) the air. Adapted from ref. 3. Copyright 2020 Wiley-VCH Verlag GmbH.

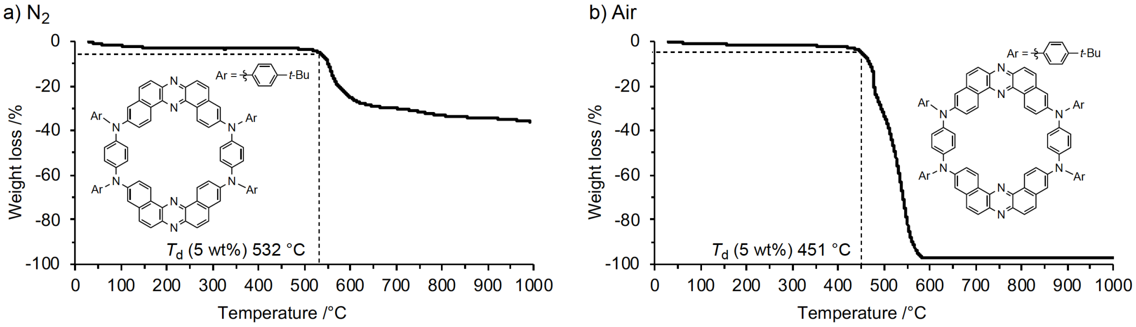

**Figure 11.** TGA profiles of ***t*-Bu-MC** under (a) a N$_2$ gas flow and (b) the air. Reproduced from ref. 9. Copyright 2020 Wiley-VCH Verlag GmbH.

**Emission dependence of laser pulse energy and temperature.**

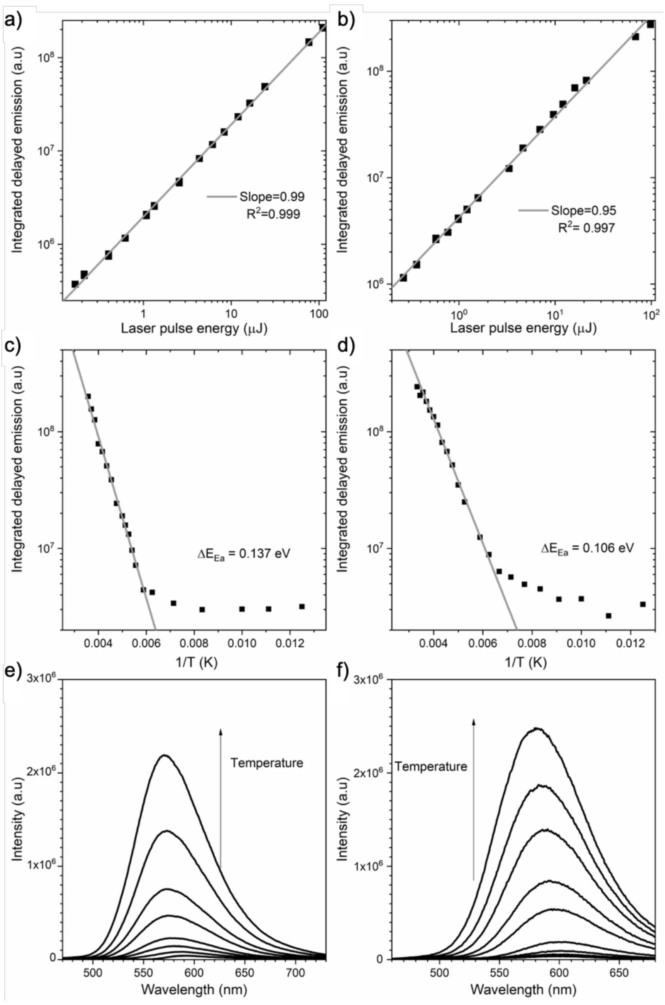

**Figure 12.** (a) Laser pulse energy versus delay emission intensity of 1% w/w ***p*-MC** in COP. Delay time = 500 μs, integration time 200 μs. (b) Laser pulse energy versus delay emission intensity of 10% w/w ***p*-MC** in CBP. Delay time = 50 μs, integration time 250 μs. (c) Integrated delayed emission versus the inverse of temperature (K) of (d) 1% w/w ***p*-MC** in COP and (e) 10% w/w ***p*-MC** in CBP. Delay time = 100 μs, integration time 100 μs. Temperature-dependent emission spectra of ***p*-MC** in (e) COP and (f) CBP. Reproduced from ref. 2. Copyright 2020 American Chemical Society.

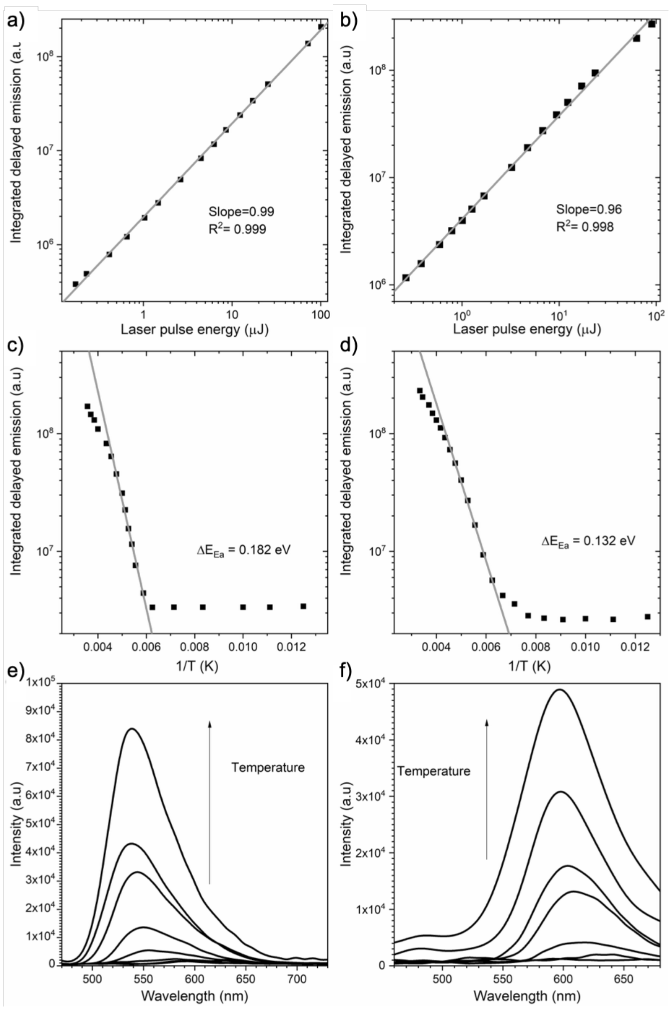

**Figure 13.** (a) Laser pulse energy versus delay emission intensity of 1% w/w of **Linear** in COP. Delay time = 500 μs, integration time 200 μs. (b) Laser pulse energy versus delay emission intensity of 10% w/w **Linear** in CBP. Delay time = 50 μs, integration time 250 μs. (c) Integrated delayed emission versus the inverse of temperature (K) of 1% w/w **Linear** in COP and (d) 10% w/w **Linear** in CBP. Delay time = 100 μs, integration time 100 μs. Temperature-dependent emission spectra of **Linear** in (e) COP and (f) CBP. Reproduced from ref. 2. Copyright 2020 American Chemical Society.

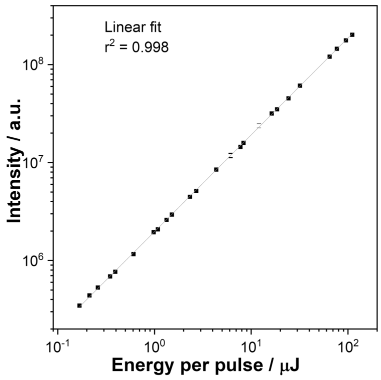

**Figure 14.** Power dependence of delayed fluorescence of ***m*-MC** in COP at 300 K. Reproduced from ref. 3. Copyright 2020 Wiley-VCH Verlag GmbH.

**Time-resolved luminescence spectroscopy of *t*-Bu-MC in films.**

In COP and CBP host, ***t*-Bu-MC** showed emission within two distinct time regions (Figure 15c and d). As is the case for ***p*-MC** and **Linear**, the first component of ***t*-Bu-MC**, which decayed with a lifetime within the nanosecond time regime, was attributed to prompt emission from the singlet excited state due to its temperature independence (Figure 15a and b). The emission spectra of ***t*-Bu-MC** observed at nanosecond time delays in both of COP and CBP exhibited Gaussian shapes ascribed to the irradiation from $^{1}$CT. In the millisecond regime, delayed emissions with similar millisecond timescales from the singlet and triplet states were observed (Figure 15c and d). The delayed emissions of ***t*-Bu-MC** observed in the millisecond region at room temperature (300 K) was ascribed to TADF, because it well overlapped with the prompt CT emission spectra (Figure 15a and b). In contrast, the delayed emission observed at a low temperature (50 K) was the emission from the triplet state with the onset triplet energy being at 2.34 eV in COP and 2.14 eV in CBP host (Figure 15a and b).

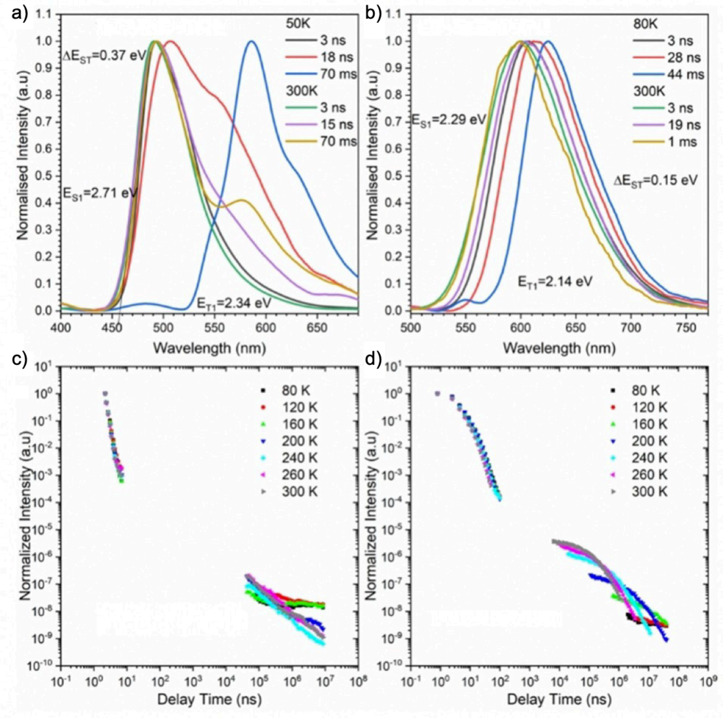

**Figure 15.** Normalized emission spectra of ***t*-BuMC** in host matrices at varying delay times at 300 K and 50 K or 80 K: (a) COP (1 wt % in host matrix) and (b) CBP (10 wt% in host matrix). Emission intensities of ***t*-BuMC** in host matrices against delay time measured at a different temperature: (c) COP (1 wt % in host matrix) and (d) CBP (10 wt% in host matrix). Reproduced from ref. 9. Copyright 2020 Wiley-VCH Verlag GmbH.

**Devices fabrication and characterization.**

OLEDs have been fabricated on pre-cleaned, patterned indium-tin-oxide (ITO) coated glass substrates with a sheet resistance of 20 Ω/sq and ITO thickness of 100 nm. All small molecules and cathode layers were thermally evaporated in Kurt J. Lesker SuperSpectros 200 evaporation system under pressure of $10^{-6}$–$10^{-7}$ mbar without breaking the vacuum. The sizes of pixels were 4 $mm^2$, 8 $mm^2$ and 16 $mm^2$. All organic evaporated compounds were purified by CreaPhys organic sublimation system. All materials were purified by temperature-gradient sublimation in a vacuum. The characteristics of the devices were recorded using 10-inch integrating sphere (Labsphere) connected to a Source Meter Unit and Ocean Optics USB4000 spectrometer.

The luminance of device based on ***t*-BuMC** was quite high (more than 11,000 cd $m^{-2}$) but still lower than those for devices fabricated with **Linear** (ca. 12,500 cd $m^{-2}$) and ***p*-MC** (>23,000 cd $m^{-2}$) emitters (Figure 16c). In the lower voltage, the ***t*-BuMC**-based device exhibited a higher brightness than others, however, after 5 V (ca. 8 mA $cm^{-2}$), the process connected to the roll-off was observed, and the emission increased with a lower rate. Device optimization, which usually helps to decrease the roll-off, did not help in the case of ***t*-BuMC** emitter. This suggests that the roll-off is caused not by the problems related to charge injection and/or device structure but by the one lying in emitter itself.

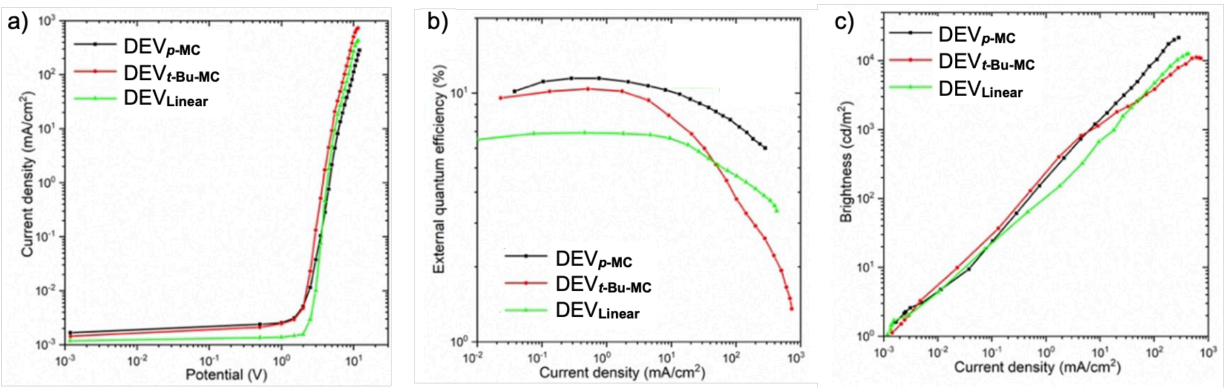

**Figure 16.** Comparison of device characteristics between ***p*-MC**, **Linear**, and ***t*-BuMC**. Adapted from ref. 9. Copyright 2020 Wiley-VCH Verlag GmbH.

## 3-7. References

1. Tang, C. W.; VanSlyke, S. A. *Appl. Phys. Lett.* **1987**, *51*, 913–915.
2. Izumi, S.; Higginbotham, H. F.; Nyga, A.; Stachelek, P.; Tohnai, N.; de Silva, P. Data, P.; Takeda, Y.; Minakata, S. *J. Am. Chem. Soc.* **2020**, *142*, 1482–1491.
3. Izumi, S.; Nyga, A.; de Silva, P.; Tohnai, N.; Minakata, S.; Data, P.; Takeda, Y.; *Chem. Asian J.* **2020**, *15*, 4098–4103.
4. Babazadeh, M.; Burn, P. L.; Huang, D. M. *Phys. Chem. Chem. Phys.* **2019**, *21*, 9740–9746.
5. [Catalog] ZEONEX®. http://www.zeon.co.jp/content/200323391.pdf (accessed Jan 4, 2021)
6. Data, P.; Pander, P.; Okazaki, M.; Takeda, Y.; Minakata, S.; Monkman, A. P. *Angew. Chem., Int. Ed.* **2016**, *55*, 5739−5744.
7. Takeda, Y.; Okazaki, M.; Minakata, S. *Chem. Commun.* **2014**, *50*, 10291– 10294.
8. Takeda, Y.; Data, P.; Minakata, S. *Chem. Commun.* **2020**, *56*, 8884–8894.
9. Nyga, A.; Izumi, S.; Higginbotham, H. F.; Stachelek, P.; Pluczyk, S.; de Silva, P.; Minakata, S.; Takeda, Y.; Data, P. *Asian J. Org. Chem.* **2020**, *9*, 2153–2161.

# Conclusion

The present Thesis aimed at the development of thermally activated delayed fluorescent donor-accepter-donor-accepter π-conjugated macrocycles and their applications to OLEDs. The results obtained through the studies are summarized as follows:

Chapter 1 describes the design and synthesis of D–A–D–A π-conjugated macrocycles (***p*-MC**, ***m*-MC** and ***t*-Bu-MC**) and a linear compound (**Linear**) comprising phenylenediamine derivatives as donors and dibenzo[*a*,*j*]phenazines as acceptors. The combination of U-shaped electron-deficient DBPHZ as the accepters and electron-rich propeller-structured *p*-phenylenediamine derivatives as the donors is the key to both of synthetic feasibility and TADF function. The D–A–D–A π-conjugated macrocycle ***p*-MC** is designed. The synthetic routes to the macrocycles and the linear compound have been successfully achieved.

Chapter 2 describes the structural analyses of the D–A–D–A π-conjugated macrocycles (***p*-MC**, ***m*-MC**) and the investigation of steady-state photophysical and electrochemical properties of all the compounds. Depending on recrystallization conditions, ***p*-MC** shows two polymorphs with different emitting color under UV irradiation. ***p*-MC** and **Linear** show suitable properties for TADF materials such as ICT characteristics in UV-vis absorption and photoluminescence and electrochemically reversible redox behaviors. In contrast, ***m*-MC** exhibits weak ICT nature when compared to ***p*-MC** and **Linear**, and electrochemical instability, which is suggested that ***m*-MC** does not show efficient TADF.

Chapter 3 describes the TADF properties of the D–A–D–A compounds and applications to OLED devices as an emitter. As implied in Chapter 2, ***p*-MC** and **Linear** show TADF in both solutions and films, while ***m*-MC** exhibits faint or no TADF. The OLED device fabricated with ***p*-MC** achieves EQE up to 11.6%, which significantly exceeds theoretical maximum (~5%) with that with a conventional fluorescent emitter and the maximum EQE of the OLED with **Linear** (6.9%).

Through this Thesis, it is revealed that the macrocyclization of D–A–D–A π-conjugated unit is an effective strategy for enhancing the efficiency of TADF. In addition, the topology in phenylenediamine donor of the D–A–D–A macrocycle significantly affects TADF properties. Efficient TADF of D–A–D–A macrocycle is achieved by employing *p*-phenylenediamine.

The findings obtained through this study as mentioned above would significantly contribute to the progress in TADF molecules and D–A π-conjugated macrocycles.

# List of Publications

The content of this thesis has been published in the following papers.

1) Thermally Activated Delayed Fluorescent Donor–Acceptor–Donor–Acceptor π-Conjugated Macrocycle for Organic Light-Emitting Diodes

   Saika Izumi, Heather F. Higginbotham, Aleksandra Nyga, Patrycja Stachelek, Norimitsu Tohnai, Piotr de Silva, Przemyslaw Data, Youhei Takeda, and Satoshi Minakata

   *J. Am. Chem. Soc.* **2020**, *142*, 1482–1491.

2) Electrochemical and Spectroelectrochemical Comparative Study of Macrocyclic Thermally Activated Delayed Fluorescent Compounds: Molecular Charge Stability vs OLED EQE Roll-Off

   Aleksandra Nyga,[†] Saika Izumi,[†] Heather F. Higginbotham, Patrycja Stachelek, Sandra Pluczyk, Piotr de Silva, Satoshi Minakata, Youhei Takeda, and Przemyslaw Data
   [†]These authors contributed equally.

   *Asian J. Org. Chem.* **2020**, *9*, 2153–2161.

3) Revealing Topological Influence of Phenylenediamine Unit on Physicochemical Properties of Donor–Acceptor–Donor–Acceptor Thermally Activated Delayed Fluorescent Macrocycles

   Saika Izumi, Aleksandra Nyga, Piotr de Silva, Norimitsu Tohnai, Satoshi Minakata, Przemyslaw Data, and Youhei Takeda

   *Chem Asian J.* **2020**, *15*, 4098–4103.

# Copyright

The author has obtained the permissions to reuse contents. The author wishes to express her thanks to Copyright Clearance Center, Creative Commons, American Chemical Society, and Wiley-VCH Verlag GmbH, Weinheim.

Credits

Reprinted with permission from Izumi, S.; Higginbotham, H. F.; Nyga, A.; Stachelek, P.; Tohnai, N.; de Silva, P.; Data, P.; Takeda, Y.; Minakata, S. *J. Am. Chem. Soc.* **2020**, *142*, 1482–1491. Copyright 2020 American Chemical Society.

Reprinted with permission from Nyga, A.; Izumi, S.; Higginbotham, H. F.; Stachelek, P.; Pluczyk, S.; de Silva, P.; Minakata, S.; Takeda, Y.; Data, P. *Asian J. Org. Chem.* **2020**, *9*, 2153–2161. Copyright 2020 Wiley-VCH Verlag GmbH, Weinheim.

Reprinted with permission from Izumi, S.; Nyga, A.; de Silva, P.; Tohnai, N.; Minakata, S.; Data, P.; Takeda, Y. *Chem Asian J.* **2020**, *15*, 4098–4103. Copyright 2020 Wiley-VCH Verlag GmbH, Weinheim.

# Acknowledgement

The author would like to express her sincere gratitude to Professor Dr. Satoshi Minakata, Department of Applied Chemistry, Graduate School of Engineering, Osaka University for his thoughtful supervision and valuable helps throughout this work. She wishes to express her deeply thanks to Professor Dr. Ken-ichi Nakayama for his reviewing this Thesis with helpful comments and suggestions. The author also greatly appreciates to Professor Dr. Norimitsu Tohnai for his reviewing this Thesis with kind comments and suggestion and, moreover, for the performance of single crystal X-ray structure analysis.

The author owes a great debt of gratitude to Associate Professor Dr. Youhei Takeda for his continuous guidance and invaluable advices during the course of this study. She is sincerely grateful to Assistant Professor Dr. Kensuke Kiyokawa for his helpful discussions and encouragement.

She is indebted to Assistant Professor Dr. Takashi Tsujimoto for his assistance in DSC measurements and to Assistant Professor Dr. Taro Uematsu for his assistance in CV and DPV measurements. She expresses her appreciation to Professor Dr. Yutaka Ie and Assistant Professor Dr. Seihou Jinnai for their assistance in the purification of sample by sublimation.

The author would like to express her gratitude to Ms. Aleksandra Nyga, Dr. Patryja Stachelek, Dr. Sandra Pluczyk, Dr. Heather F. Higginbotham, and Associate Professor Dr. Przemyslaw Data, for their valuable discussion and excellent collaboration about electrochemical and spectrochemical studies, fabrication of OLED devices, and investigations of their performances. She also appreciates helpful discussion and great collaboration with Assistant Professor Dr. Piotr de Silva about theoretical calculations.

Thanks are also due to the Instrumental Analysis Center, Graduate School of Engineering, Osaka University, for the measurement of spectral and analysis data. The author would like to especially thank Dr. Kyoko Inoue for her kind support and insightful comments for NMR measurements.

The author deeply thanks Ms. Junko Ohmagari for her kind help and heart-warning encouragement.

The author is deeply indebted to Dr. Masato Okazaki for his valuable discussion and kind words. Thanks are also due to all students of Minakata group for their hearty encouragement, constant support and kind friendship.

Furthermore, the author is deeply grateful to her family, Mr. Hiroe Izumi, Ms. Toyoko Izumi, Ms. Hiromi Izumi and Ms. Yuka Izumi, for their full understanding and perpetual support, which enabled her to complete her doctorate.

Finally, her appreciation cannot be expressed in words for all people who helped her during doctoral course.

Saika Izumi